工學博士學位論文

Fabrication of Organic Electrodes Using Conducting Polymers and Graphene and Their Organic Electronic Device Applications

전도성 고분자와 그래핀을 이용한 유기전극의 제조 및 유기전자소자에의 응용

2014年 2月

서울大學校 大學院

化學生物工學部

申 慶 煥

Fabrication of Organic Electrodes Using Conducting Polymers and Graphene and Their Organic Electronic Device Applications

by

Kyoung-Hwan Shin

Submitted to the Graduate School of Seoul National University

in Partial Fulfillment of the Requirements

for the Degree of Doctor of Philosophy

February, 2014

Thesis Adviser: Jyongsik Jang

Fabrication of Organic Electrodes Using Conducting Polymers and Graphene and Their Organic Electronic Device Applications

전도성 고분자와 그래핀을 이용한 유기전극의 제조 및 유기전자소자에의 응용

指導敎授: 張 正 植

이 論文을 工學博士 學位論文으로 提出함

2013年 10月

서울大學校 大學院

化學生物工學部

申 慶 煥

申 慶 煥의 工學博士 學位論文을 認准함

2013年 11月

委 員 長 趙 在 英 (인)

副委員長 張 正 植 (인)

委 員 金 榮 奎 (인)

委 員 李 鍾 贊 (인)

委 員 林 淳 皓 (인)

Abstract

Fabrication of Organic Electrodes Using Conducting Polymers and Graphene and Their Organic Electronic Device Applications

Kyoung-Hwan Shin
School of Chemical and Biological Engineering
The Graduate School
Seoul National University

Organic electronic devices will significantly improve and revolutionize several aspects of our daily life. The most envisaged applications are the displays, lighting modules, and organic photovoltaic cells. Organic electronic devices have considerable advantages in contrast to current devices, such as lightweight, thin, robust, conformable, and flexibility. The performance, efficiency and lifetime of organic electronic devices are greatly affected by the optical, electrical, and structural properties of the organic electrodes. These should meet specific and advanced requirements, such as high optical transparency, ultra low atmospheric gas permeability, electrical conductivity, structural stability, film–substrate adhesion, etc. Electrodes consisted of transparent conductive oxides have attracted a considerable amount of interest

and have been extensively investigated. Traditionally, the most common material is indium tin oxide, which has retained its dominance due to superior combination of high optical transparency and low resistance.

However, indium tin oxide is also prone to several major problems. The supply of indium is constrained by both mining and geo-political issues; therefore, indium is relatively expensive. Adding to the cost of indium tin oxide is the expense of setting up and maintaining a sputter deposition line, as well as the low deposition yields. In addition to cost, indium tin oxide suffers from being quite brittle, showing cracks at relatively low strains. This is already a problem in many of today's devices, and promises to be an even bigger issue in future flexible electronics.

To make light, unbreakable, flexible, rollable, and fully transparent devices, eventually, it is indispensable that the metal-based components should be replaced with organic materials. This dissertation presents a potential solution of the materials for the electrode of organic electronic devices focusing on conducting polymers and graphene. Solution-processable polyaniline is fabricated by secondary doping with camphorsulfonic acid. The polyaniline solution can be spin-coated onto various substrates including glass, indium tin oxide and flexible polymeric film, which process yields highly conductive polyaniline electrodes successfully. Inkjet printing-mediated vapor deposition

polymerization is emerging as a useful method for printing an electrode pattern of nondispersive conducting polymers. An exquisitely patterned polypyrrole electrodes is formed by the technique in top-contact thin film transistor instead of metal electrodes. A novel and reliable approach for the preparation of reduced graphene oxide transparent electrodes is conducted through the combination of chemical and subsequent pressure-assisted thermal reduction at 180℃ on a flexible plastic substrate. This reduction process produces reduced graphene oxide electrodes without the transferring or imprinting processes used in conventional synthetic approaches for graphene thin film production. These results strongly suggest that these organic electrodes should be potentially very useful in many new types of applications related to organic electronic devices.

Keywords: Organic electrodes; Conducting polymer; Graphene; Chemical sensor; Dye-sensitized solar cell; Organic thin film transistor

Student Number: 2010–30806

List of Abbreviations

AFM : atomic force microcsope

APS : ammonium persulfate

BIPV : building integrated photovoltaic

C60 : fullerene

CNT : carbon nanotube

CRGO : chemically reduced graphene oxide

CSA : 10-camphorsulfonic acid

CV : cyclic voltammetry

CVD : chemical vapor deposition

DSSC : dye-sensitized solar cell

EB : emeraldine base

EIS : electrical impedance spectra

EOI : imidazolium iodide

ES : emeraldine salt

FE-SEM : field-emission scanning electron microscopy

FET : field-effect transistor

FIB : focused ion beam

FT-IR : Fourier transform infrared

FTIR-ATR : Fourier transform infrared-attenuated total reflection

FTO : fluorine-doped tin oxde

GI : gate insulator

GO : graphene oxide

HSC : hybrid solar cell

IJP-VDP : inkjet printing-mediated vapor deposition polymerization

IPCE : incident photon-to-current efficiency

ITO : indium tin oxide

j_{sc} : short circuit current

LB : Langmuir-Blodgett

LE : leucoemeraldine

LED : light emitting diode

$\bar{M}_v$: viscosity average molecular weight

MFC : mass flow controller

MPII : 1-methyl-3-propylimidazolium iodide

MPN : methoxypropionitrile

NHE : normal hydrogen electrode

NIR : near infrared

NMP : N-methyl-2-pyrrolidone

OED : organic electronic device

OPV : organic photovoltaic cell

OTFT : organic thin film transistor

PACB : polyaniline-loaded carbon black

PANI : polyaniline

PCE : power conversion efficiency

PEN : polyethylene naphthalate

PES : polyethersulfone

PET : polyethylene terephthalate

PETA : pentaerythritol triacrylate

PG : pernigraniline

PGMEA : propylene glycol monomethyl ether acetate

PPy : polypyrrole

PRGO : pressure-assisted thermally reduced graphene oxide

PSC : polymer solar cell

PSS : polystyrenesulfonate

PT : polythiophene

PVP : polyvinylphenol

R_{ct} : charge transfer resistance

rGO : reduced graphene oxide

RMS : root mean square

R_s : electrolyte resistance

SEM : scanning electron microscope

SWCNT : single-walled carbon nanotube

TBP : tert-butyl pyridine

TCO : transparent conductive oxide

TEM :Transmission electron microscope

THF : tetrahydrofuran

TIPS-pentacene : 6,13-bis(triisopropylsilylethynyl)-pentacene

TLM : transfer-line method

TRGO : thermally reduced graphene oxide

TsO : *p*-toluenesulfonate

V_{oc} : open-circuit voltage

W_s : Warburg impedance

XPS : X-ray photoelectron spectroscope

XRD : X-ray diffraction

μ : mobility

[η] : intrinsic viscosity

List of Tables

List of Figures

Table of Contents

1. Introduction

1.1. Background

1.1.1. Organic electronic devices

Organic electronic devices (OEDs) are expected to improve our daily life and to significantly advance the visualization of information, communications, information technology, energy generation through renewable resources, building lighting, high resolution imaging systems and others [1–4]. Among the envisaged applications, the most promising are the displays and lighting modules, organic photovoltaic cells (OPVs), data systems and media, etc [1–5]. OEDs will be characterized by considerable advantages in contrast to current devices, such as lightweight, thin, robust, conformable, and ability to be rolled when are not in use [5–9].

The conventional semiconductor industry is based upon the inorganic materials such as SiO_2 for insulators, GaAs and doped Si for semiconductors and Cu, Au and Al for electrodes. Nowadays, the replacement of rigid substrates and electrodes by soft materials such as polymers represents one of the key challenges for the production of novel display, lighting and energy generation systems [1–6,10].

The development of OEDs is closely related to contemporary innovations in both materials and processes, at lab and production scale. These innovations include novel nanostructured materials, such as conducting polymers, graphene, printable metals, and organic semiconductors, which are soluble or

can be deposited by printing processes [1–10]. Also, flexible polymeric substrates (polyethersulfone (PES), polyethylene terephthalate (PET), polyethylene naphthalate (PEN), etc.) are promising to replace the rigid ones (Si and glass) and new plastic-based substrates coupled with modern sophisticated techniques for the growth and printing of organic light-emitting polymers and active matrix thin-film transistor arrays, open up the possibility of cost-effective, roll-to-roll processing in high volumes for the intergraded production of OEDs in large scale [11–13].

However, the performance, efficiency and lifetime of OEDs are greatly affected by the optical, electrical, and structural properties of the organic electrodes. These should meet specific and advanced requirements, such as high optical transparency, ultra low atmospheric gas permeability, electrical conductivity, structural stability, film–substrate adhesion, etc [11]. These properties are determined and controlled by the bonding structure of the materials, and on the surface and interface nanostructure and chemistry [10–14]. The detailed knowledge of the bonding structure, mechanical response and surface nano-topography of the organic electrodes are of significant importance and affect all the production steps.

Electrodes consisted of transparent conductive oxides (TCO) have attracted a considerable amount of interest and they have been extensively investigated since they constitute a major stage of the production of electronic devices both on rigid and flexible substrates. Traditionally, the material of choice is a sputtered metal oxide, the most common of which is indium tin

oxide (ITO). ITO was first synthesized and studied in the 1940s, and has been well developed over the last 50 years. ITO has retained its dominance due to its superior combination of high optical transparency and low resistance, the two most important features of a transparent conductor; emerging nanomaterials have struggled to compete with ITO in this respect.

However, ITO is also prone to several major problems. The supply of indium is constrained by both mining and geo-political issues; therefore, indium is relatively expensive, having its price peaking at over $800/kg in 2006, and this cost is reflected in ITO pricing. Adding to the cost of ITO is the expense of setting up and maintaining a sputter deposition line, as well as the low deposition yields. In addition to cost, ITO suffers from being quite brittle, showing cracks at relatively low strains, which lead to a sharp increase in resistance. This is already a problem in many of today's devices, and promises to be an even bigger issue in future flexible electronics. Fortunately, recent advances in nanomaterials synthesis, purification, and solubilization have led to the emergence of viable alternatives to ITO [15]. The materials most often considered to replace sputtered ITO include nanostructured ITO [16–18], conducting polymers [19–21], nanostructured silver [22–25], carbon nanotubes (CNTs) [26–28], and graphene [29,30].

In this introduction part, a short overview of the materials for the electrode of OEDs will be provided focusing on conducting polymers and graphene. Also, some of the latest advances on the applications of organic electrodes will be reported including chem/bio sensors, solar cells, and transistors.

1.1.2. Organic materials for electrode

1.1.2.1. Conducting polymer

Conducting polymers are rendered conductive through a conjugated bond system along the polymer backbone. They are typically formed either through chemical oxidation of the monomer (for example with iron chloride) [31] or electrochemical oxidation of the monomer. Two oxidation reactions occur simultaneously – the oxidation of the monomer and the oxidation of the polymer [32] with the coincident insertion of a dopant/counter ion (e.g. Cl^-). The dopant or doping level (in this p-type conducting polymer) is typically below 1 dopant per polymer unit: approximately 0.3–0.5, i.e., 2–3 monomer units per dopant. This is limited by how closely the positive charges (so-called polarons) can be spaced along the polymer chain.

Synthesis of conducting polymers for electrodes may be accomplished through electrochemical or chemical means. In general, oxidation is used to provide the driving force for polymer synthesis, whether it is through the addition of a chemical oxidant (e.g., ammonium persulfate) or through the application of an oxidizing electrochemical potential to the surface of a submerged electrode [33]. As this type of synthesis is performed in an oxidizing environment, the resulting polymers are formed in an already doped state. Polyaniline (PANI), for example, is synthesized in the emeraldine salt state under oxidative conditions. Reductive polymerization is not unheard of, but is rarely employed primarily due to limited applicability [34–37]. This is possibly one reason p-type polymers are more commonly studied than n-type

polymers. Conducting polymers are most often synthesized in a solution of monomer and electrolyte, but there are examples of solid-state or vapor deposition polymerizations as well [38,39]. Metal-catalyzed cross-couplings are another method for producing conjugated polymers [40–44]. Unlike oxidative synthesis, polymers synthesized in this way are formed in a charge-neutral state. Unfortunately, these systems can sometimes require the presence of specific functional groups and sensitive reaction conditions not conducive to producing large quantities of material suitable for electrodes. However, promising advances in direct arylation polymerizations are working toward eliminating the need for generating monomers with specific functional group requirements [45]. Metal-catalyzed polycondensations are also a potential method for synthesizing new n-type or specially functionalized materials [46].

Several recent synthetic approaches have focused upon increasing the solubility or dispersibility of conducting polymers to enhance their processability. Side chains are essential for solubilizing conducting polymers used in semiconducting applications, and similar concepts are applicable for electrochemical energy storage [47–50]. Side chain functionalization has been used to facilitate intimate mixing in composites [51–53]. Conducting polymer:polyelectrolyte complexes have also come a long way to improve polymer processing [54–56].

The polymers that are most commonly studied for use in organic electrodes are polypyrrole (PPy) and PANI.

PPy was firstly synthesized in 1912 [57]. PPy synthesized by conventional

chemical methods is insoluble in common solvents because of strong inter-chain interactions [58]. Two major ways are applied for PPy synthesis which are based on induction of polymerization by different factors: (i) chemical initiation by oxidative agents [59]; (ii) photo induced synthesis [60]; (iii) electrochemical activation by anodic current [61]. All polymerization initiation methods mentioned have particular application, e.g. chemical initiation by oxidative agents might be successfully applied if a great amount of PPy is needed for application in the design of chromatography columns [62] or for some other purposes. By using chemical [59] or even biochemical [63] methods it is easy to prepare PPy particles of different and/or controlled size ranging from several nanometers up to several micrometers and/or containing various inclusions. Moreover, by chemical methods it is possible to uniformly perform overoxidation of this polymer, what is on special interest of affinity chromatography since molecularly imprinted PPy might be produced, which might exhibit selectivity to molecules ranging from the small organics [64–66] to high molecular weight biomolecules [67]. Photo-induced PPy synthesis is attractive in photolithographic application of this polymer, since it allows alterations in synthesized PPy morphology by change of excitation light wave length [68] and theoretically it might be applied for the design of electronic chips. However, because of slow light induced polymerization rate this polymerization type is still not very often applied if compared with chemical or electrochemical polymerization.

By using chemically induced polymerization the PPy is mainly produced

in the bulk solution and just some amount of synthesized PPy is covering the surface of introduced materials. It means that chemically induced polymerization is not very efficient with respect to deposition of PPy over some surfaces. Moreover, PPy is almost insoluble in usual solvents, except some cases where it is doped with proper agents increasing solubility of this polymer [69] and it means that deposition (e.g. by solvent evaporation) of this polymer from the solution containing dissolved polymer is possible at the stage where the polymer is still in the form of colloid particles, before its precipitation [63]. However, the major obstacle for use of this deposition method for designing of PPy based sensors is a poor adherence of this deposit to the surface, contrary to the film obtained by electrochemical polymerization. But all these disadvantages might be avoided if electrochemical polymerization is applied (**Figure 1**). It allows deposition of PPy over electrodes deposited in the electrochemical cell. That is the reason why electrochemical polymerization has found an application as a general deposition method if thin PPy layers are requested. By using this method thickness and morphology of deposited layer might be controlled by application of well-defined potential and known current passing through the electrochemical cell [70]. Electrochemical deposition of PPy might be performed from various solvents (e.g. acetonitrile, water, etc.).

PANI has attracted much attention due to its unique and controllable chemical and electrical properties [71], its environmental [72], thermal [73] and electrochemical stability [74], and its interesting electrochemical, electronic,

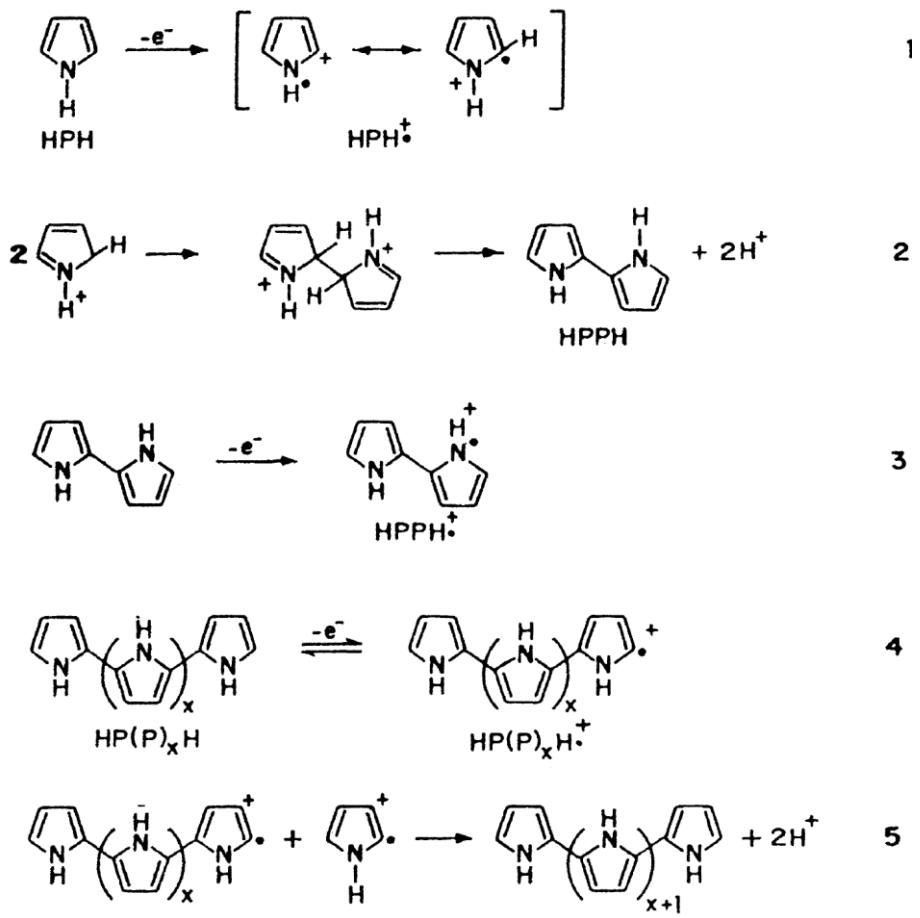

Figure 1. Mechanism for the electrochemical polymerization of the PPy. Reprinted with permission. Copyright 2003 Elsevier.

optical and electro-optical properties [75]. Moreover, PANI is known to have a broad range of tunable properties emanating from its structural flexibility leading to many applications in different fields such as anti-corrosive coatings, energy storage systems, gas sensing, as well as electrochromic and electrocatalytic devices. Chandrakanthl and Careem have claimed that PANI has the highest environmental stability [76] and is recognized as the only conducting polymer that is stable in air [77]. From economic point of view, aniline monomer is less expensive than other monomers used for the synthesis of other conducting polymers.

The structure of PANI has been illustrated in **Figure 2**. Leucoemeraldine (LE) is fully reduced state. Pernigraniline (PG) is fully oxidized state with imine links instead of amine links. The emeraldine form of PANI, often referred to as emeraldine base (EB), is either neutral or doped, with imine nitrogens protonated by an acid. EB is regarded as the most useful form of PANI due to its high stability at room temperature and moreover its doped form (emeraldine salt; ES) is electrically conducting. LE and PG are poor conductors, even when doped with an acid. These forms may be inter-converted by chemical and/or electrochemical oxidation or reduction.

PANI is a p-type semiconductor and thus majority charge carriers in PANI are holes [78]. The delocalized π-bonds available in this system are responsible for its semi-conducting properties. PANI has semi-crystalline, heterogeneous system with a crystalline (ordered) region dispersed in an amorphous (disordered) region [79]. It is similar to a quasi-metallic island surrounded by

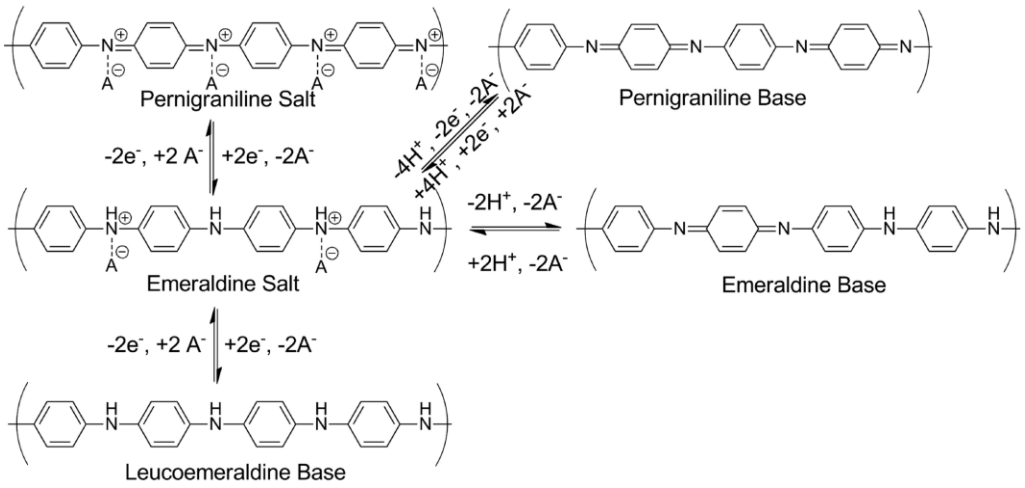

Figure 2. Illustration of the redox states of PANI and the chemical reactions associated with their interconversion. Reprinted with permission. Copyright 2013 John Wiley and Sons.

non-metallic amorphous zone. When PANI is doped with an acid, a polaron is formed through successive formation of bipositive species, bipolaron structure, and more stable polaron structure. This polaron structure is responsible for electrical conduction through hopping mechanism in its crystalline region and this hopping may be intra-chain or inter-chain [80]. In polaron structure, a cation radical of one nitrogen acts as a hole and this hole acts as charge carriers. The electron from the adjacent nitrogen (neutral) jumps to this hole and it becomes electrically neutral. Consequently, the holes start to move. However, in bipolaron structure, this type of movement is not possible since two holes are adjacently located. In LE or PN structures, the electronic environments of all nitrogen atoms along the polymer chain are similar. Protons from a dopant can be attracted by any nitrogen atom and there may be a few (more than two) protonated nitrogen or free nitrogen atoms situated side by side across the chain. Hence, there is a less chance for chain regularity, creating less chance for the formation of a polaron. As a result, protonated LE or PN are insulating in nature.

1.1.2.2. Graphene

Up till now, many reports have suggested that graphene-based electrodes are promising candidates in a wide range of applications, such as field-effect transistors (FETs) [81], solar cells [82], light emitting diodes (LEDs) [83], touch screens [84], electrochemical sensors [85,86], batteries [87] and supercapacitors [88,89]. For electronic and optoelectronic devices, like solar

cells and LEDs, doped metal oxides, particularly ITO, have been widely used as electrode materials due to their low sheet resistance (e.g., 10–30 Ω sq^{-1}) and high optical transmittance (> 90% at 550 nm) [90]. Unfortunately, concerns have been raised over the limited indium source, stringent deposition conditions, and consequently high costs [91]. In addition, ITO also suffers from several technical disadvantages. For example, its brittle nature leads to cracks and fracture at a low strain of 2–3% [91,92]. It is not stable in basic or acidic environments, which causes a shortened life time [91,93]. Furthermore, the ITO film has a relatively high index of refraction ($n \approx 2.0$), which can result in unwanted reflections when they are coated on substrates with relatively lower refraction indices [91]. Other potential issues associated with the ITO thin film are the ion diffusion from the ITO to the polymer layer in solar cells, and the poor transparency in the near infrared (NIR) region, which compromises their performance in solar harvesting and certain NIR-based optoelectronic devices [94]. In contrast, the chemical vapor deposition (CVD)-graphene-based thin film, with comparable conductivity and transparency to ITO [95], has shown many attractive and competitive advantages, such as the excellent flexibility and good thermal and chemical stability, which suggest that the graphene-based electrode is the ideal replacement for ITO in future electronic devices. In electrochemical applications, carbon-based materials such as activated carbon, fullerenes (C_{60}), carbon nanofibers and CNTs have been widely used as electrodes [96–98], because they have many advantageous properties like good conductivity, wide potential window, and

good electrocatalytic activity for various redox reactions [99]. Furthermore, crystalline carbon structures, such as C_{60}, CNTs, and diamond, possess sp^2/sp^3 hybridized domains, which allow for chemical modification and are very important for surface reactions [99]. In fact, graphene, the building block of these crystalline carbon materials [100], exhibits similar attractive properties. Moreover, since both sides of a graphene sheet are exposed, graphene provides larger theoretical specific surface areas for electrochemical reactions compared to the other types of crystalline carbon structures. Importantly, the capability of being mass-produced from bulk graphite makes graphene-based materials even more attractive for development of the cost-effective, high-performance electrochemical devices like supercapacitors and batteries.

To date, graphene-based electrodes can be categorized in four groups based on the different graphene materials used, i.e., the pristine graphene electrode, the CVD-grown graphene electrode, the chemically modified graphene electrode, and the graphene composite electrode. Among them, the fabrication of chemically modified graphene electrodes usually involves solution-phase processes, requires no special equipment, making them relatively low-cost. Spin coating [101], drop casting [102], Langmuir–Blodgett (LB) method [103], self-assembly [104], and vacuum filtering [105] are the most commonly used methods to prepare thin films of GO (graphene oxide) or rGO (reduced graphene oxide) from their dispersions. The obtained GO film can be subsequently reduced by hydrazine vapor [101], thermal annealing [106], electrochemical reduction [104] and laser irradiation [105] (**Figure 3**).

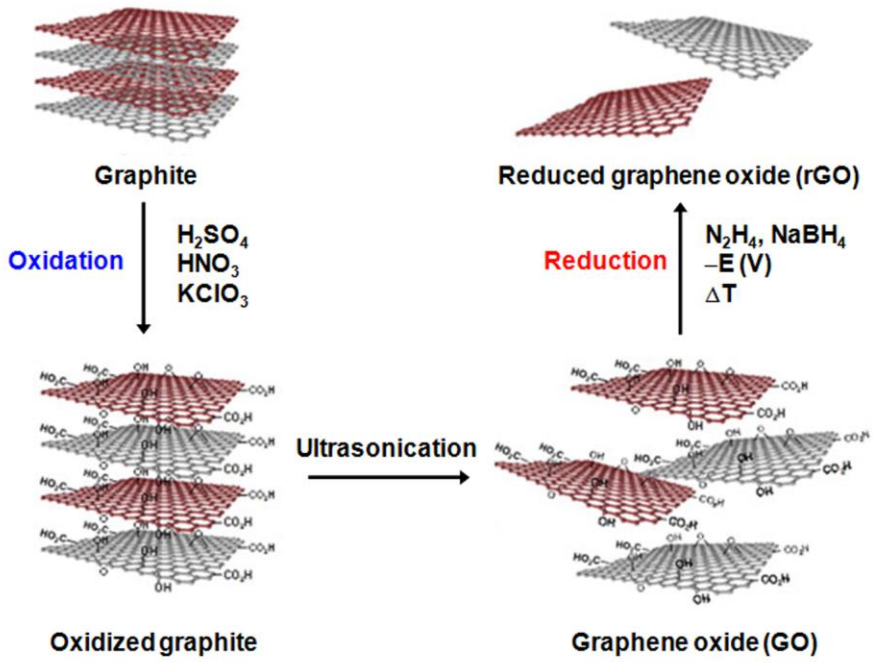

Figure 3. The procedure followed for the production of chemically modified graphene electrode using graphite as the starting material. This is followed by: (1) An oxidative treatment is initially performed to generate oxidized graphite; (2) exfoliation by ultrasonication to generate GO; (3) reduction of GO by using various reduction methods to produce rGO.

1.1.3. Applications of organic electrodes

1.1.3.1. Chem/Bio sensor

Conducting polymers, such as PPy, PANI, polythiophene (PT) and their derivatives, have been used as the active layers of gas sensors since early 1980s [107]. In comparison with most of the commercially available sensors, based usually on metal oxides and operated at high temperatures, the sensors made of conducting polymers have many improved characteristics. They have high sensitivities and short response time; especially, these features are ensured at room temperature. Conducting polymers are easy to be synthesized through chemical or electrochemical processes, and their molecular chain structure can be modified conveniently by copolymerization or structural derivations. Furthermore, conducting polymers have good mechanical properties, which allow a facile fabrication of sensors. As a result, more and more attentions have been paid to the sensors fabricated from conducting polymers, and a lot of related articles were published. There are several reviews emphasize different aspects of gas sensors [108–110], and some others discussed sensing performance of certain conducting polymers [111–113].

Conducting polymers have been extensively used as transducers in electrochemical biosensors to measure and amplify signals [114]. Both intrinsically conducting polymers and conducting polymer-nanocomposite materials have been used as bio-transducers. Some of the most commonly used conducting polymers for development of different types of electrochemical biosensors are: PANI, PPy and PT. Low cost, scalability, easy

processing capability and material properties such as large surface area, adjustable transport properties, and chemical specificities makes conducting polymers attractive candidates for applications in electrochemical sensing [115]. Conjugated conducting polymers contain alternating single and double bonds in their polymer chain resulting in the formation of de-localized electrons which act as charge carriers. In order to improve sensitivity and selectivity of the biosensors, redox mediators are dispersed, added as dopants or chemically conjugated into the polymer matrix [116–118]. Conjugated conducting polymers, thus, mediates electron transfer between the biorecognition layer and the final electrode [119]. Moreover, the conjugated backbone of conducting polymers allows modulation of its properties by enabling attachments (or immobilization) to a variety of chemical moieties.

Graphene and its derivatives have shown great potential to replace or supplement other carbon-based materials like CNTs, C_{60} and graphite in electrochemical sensing [120–122]. Various kinds of electrodes based on functionalized graphene or graphene composites have been fabricated to detect a wide range of chemical and biochemical species, such as H_2O_2 [123], ascorbic acid [124], glucose [125], dopamine [126], DNA [127], and antigen [128].

1.1.3.2. Solar cell

Solar cells, which can convert sun light energy to electrical energy, are considered as the most promising devices to utilize the renewable and clean

solar energy resource in a sustainable way. Although silicon solar cells (i.e., crystalline silicon and polysilicon systems) dominate the market now, the cost of these cells limits their popularization. In contrast, organic or hybrid photovoltaic devices including polymer solar cells (PSCs), hybrid solar cells (HSCs), and dye-sensitized solar cells (DSSCs) have attracted considerable attention over the past decade due to their advantages such as light weight, flexibility and low cost [129]. The focus on solar cell devices is to improve the energy conversion efficiency and the device stability while decreasing the processing cost. It has been known that the performance of solar cells depends not only on the employed materials (active materials, electrode materials, and buffer materials), but also on their morphologies and the interfacial contact properties. So, the scientific issues in materials design and device engineering are of critical importance in order to bring various solar cells to full commercialization. From the view of pursuing solar cell devices with low cost, thin, light, and flexible architectures, conducting polymers are more competitive candidates for photovoltaic cells than conventional inorganic counterparts [130]. Currently, the progress on the synthesis of new conducting polymers has paved a new way for next generation high performance solar cells at low cost.

Conducting polymers are suitable materials for counter electrode of DSSCs. Thus Saito et al. used PEDOT doped with p-toluenesulfonate (TsO) or polystyrenesulfonate (PSS) as catalysts for counter electrodes of DSSCs [131,132]. Hole-conducting materials such as polypyrrole and polyaniline can

be used along with carbon black as a composite catalyst for the counter electrode. Kitamura et al. compared platinum-sputtered fluorine-doped tin oxide (FTO)-glass and carbon black deposited FTO-glass as counter electrodes for solid-state DSSCs, which use a polypyrrole as the hole-transport material [133]. A carbon counter electrode can improve the fill factor and the efficiency will then increase. A modest 0.62% efficiency was reported for 10 mW cm^{-2} irradiance (J_{sc} = 0.104 mA cm^{-2}, V_{oc} = 716 mV, and FF = 78%). The porous structure of the carbon increases the interface between the PPy and counter electrode to improve the charge exchange. On the other hand, Ikeda et al. used a polyaniline-loaded carbon black (PACB) as a counter electrode [134]. A viscous mixture of PACB with the ionic liquid 1,3-diethyleneoxide-derivatized imidazolium iodide (EOI) was formed and this paste was applied between the photoelectrode and bare FTO-glass as the counter electrode. The best concentration of the PACB is 10% in the PACB-EOI mixture, yielding 3.48% conversion efficiency (j_{sc} = 12.8 mA cm^{-2}, V_{oc} = 580 mV, FF = 47%).

The first solid-state DSSC based on the graphene electrode was demonstrated by Müllen and coworkers [135]. In this work, a typical rGO thin film was prepared by dip coating of an aqueous GO dispersion on a pretreated quartz substrate, followed by thermal reduction at 1100 °C. The as-prepared thin film exhibited a conductivity of 550 S cm^{-1} and transmittance of 70% over the 1000–3000 nm range but dropped to 50% at 400 nm. The fabricated rGO/TiO_2/dye/spiro-OMeTAD/Au device showed a PCE of 0.26%, lower than that (0.84%) of the corresponding FTO-based device. Therefore, the

improvement on the sheet resistance and optical transmittance of rGO thin film is the key challenge in maximizing the efficiency of a DSSC based on rGO-electrode.

As for the liquid-electrolyte DSSC, in order to replace the most widely used Pt-FTO counter electrode, graphene-based materials have been used to modify the commercial electrode of ITO, FTO, or graphite. For example, after the hydrazine-reduced GO sheets were dispersed in a terpineol solution containing 5 wt% of ethylcellulose, Zhang et al. screen-printed this dispersion onto an FTO slide followed by annealing it at 400 ℃ to give the 3D network of rGO films [136]. An improved charge transfer at the electrode-electrolyte interface was thus achieved with the enlarged effective reaction area in the 3D network, indicated by the small charge transfer resistance at the counter electrode (R_{ct} = 1.2 Ω cm^2) and a high power conversion efficiency (PCE) of 6.81%, which is comparable to that obtained by the Pt-FTO-based counter electrode.

1.1.3.3. Transistor

Mechanical flexibility is one of the most important advantages in organic thin film FETs from viewpoints of next-generation ubiquitous electronics. For a realization of flexible FET devices, C_{60} and pentacene thin film FETs with many kinds of plastic substrates and polymer dielectrics have been investigated during a past decade [137]. Furthermore, in addition to plastic substrates and polymer gate dielectrics, source/drain/gate contact electrodes are indispensable

to be replaced from conventional metal to conducting polymers for a complete mechanical flexibility. Metals such as gold and platinum have been commonly used as source/drain (S/D) electrodes Au electrodes have the favorable working function that matches well with the energy levels of p-channel organic semiconductors, so that the holes are injected and transported through the organic material [138]. However, a large contact resistance usually exists between the organic semiconductor and the metal S/D electrodes, especially in transistors with bottom-contact geometry.

Several studies on transport characteristics for organic thin film FETs with conducting polymers have been performed so far [139–142]. Cosseddu et al. recently reported ambipolar transport in C_{60}/pentacene FET with representative conducting polymer, PEDOT:PSS electrodes on PET substrate fabricated by use of soft lithography (micro contact printing) technique [141]. Actually, the ambipolar FET characteristics with the n-channel μ value of 3.5×10^{-4} cm^2 V^{-1} s^{-1} and p-channel μ value of 0.01 cm^2 V^{-1} s^{-1} are observed in this device. The n-channel μ value originating from C_{60} thin films was lower by three orders of magnitude than those for standard C_{60}-FETs with Au electrodes on SiO_2/Si and parylene/PET substrates [137,143]. Furthermore, the best μ value among p-channel organic thin film FETs with conducting polymer electrodes fabricated in bottom contact structure was at most 0.01 cm^2 V^{-1} s^{-1}, which was realized in pentacene thin film FET with PEDOT:PSS electrodes [142], although the very high μ value of 0.05–0.3 cm^2 V^{-1} s^{-1} is exceptionally reported by Halik et al. [140]; recently the high μ value of 0.2 cm^2 V^{-1} s^{-1} is

realized in pentacene thin film FET with PEDOT:PSS-coated Au electrodes in bottom contact structure [144].

Zhu and coworkers deposited graphene on patterned thin film of Cu or Ag to serve as hybrid electrodes for pentacene-FETs [145]. The decreased work function of the electrodes and the reduced contact resistance between the electrodes and semiconductor have led to a high carrier mobility of 0.53 cm^2 V^{-1} s^{-1}, which is about ten times higher than that with the pure Cu or Ag contact electrodes. In another report, all-carbon based transistor arrays were fabricated by Hong et al. [146], consisting of the semiconducting channel made from the aligned single-walled carbon nanotubes (SWCNTs) and S/D electrodes made from graphene films. Both the SWCNTs and graphene layers were produced by CVD, and integrated into FETs by a series of lithography-based patterning and transfer printing processes. The resulting devices showed the ultrathin lay-outs (SWCNTs combined with 0.6–2.0 nm graphene film) with good optical transparency throughout the visible range (75% transmittance at 550 nm). In addition, the graphene-graphene S/D electrode pair was compared with the Pd-Pd pair, giving rise to ≈ 10% higher current levels, suggesting that graphene is a better contact material for SWCNT-based FETs.

1.2. Objectives and Outline of the Study

1.2.1. Objectives

To make light, unbreakable, flexible, rollable, and fully transparent devices, eventually, it is indispensable that the metal-based components should be replaced with organic materials. The aim of this dissertation is profoundly related to the demands of the era of organic electronic devices. As part of an effort to lead the current of the times, a field of electrode has been chosen for this dissertation among the various device components. Conducting polymers and graphene provide highly flexible and conductive organic electrodes successfully. Furthermore, their applications are also explored for organic electronic devices including chemical sensor, dye-sensitized solar cell, and organic thin film transistor.

1.2.2. Outline

This dissertation focuses on the fabrication of organic electrodes with conducting polymers and graphene and their applications for organic electronic devices. In the viewpoint of above-mentioned topics, this dissertation involves the following subtopics:

I. PANI/CSA chemical sensor for NH_3 gas detection
II. TCO-free PANI/CSA counter electrode for a bifacial dye-sensitized solar cell

III. PANI/CSA counter electrode for a novel organic dye-sensitized solar cell

IV. PPy source/drain electrode using inkjet printing-mediated vapor deposition polymerization for organic thin film transistor

V. Graphene gate electrode using pressure-assisted thermal reduction method for organic thin film transistor

VI. PANI/CSA gate and Ag souce/drain electrode using inkjet printing method for organic thin film transistor

A detailed outline of the study is as follows:

1. Highly conductive PANI/CSA films have been fabricated successfully. It was investigated that the conductivity enhancement of PANI/CSA films in the viewpoint of $CHCl_3$ amount in *m*-cresol solvent. Furthermore it was applied directly to NH_3 gas sensor without any patterned microelectrodes. The fabricated sensor had high sensitivity of NH_3 gas as low as 2 ppm and the electrical responses represented reversible and reproducible behavior.
2. PANI/CSA solution was spin-coated on normal glass substrate in order to fabricate a counter electrode of DSSC. The PANI/CSA counter electrode shows high conductivity and excellent catalytic ability. This counter electrode also can be operated by introducing light from both photoanode and counter electrode sides due to transparency of the PANI/CSA film. Bifacial DSSCs can exploit solar light source more efficiently, and will be more preferable for their versatile applications as power-generating

windows, especially in the area of building integrated photovoltaics (BIPV). The assembled bifacial DSSC using the transparent PANI/CSA counter electrode presented excellent conversion efficiency of 5.50 % from front illumination and 2.67 % from back illumination. These results illustrate the promising potential for effective bifacial DSSC with Pt and TCO-free counter electrode. Furthermore, electrochemical properties of the PANI/CSA counter electrode and optical transmittance changes with electrochromism properties were analyzed.

3. The potential application of the PANI/CSA counter electrode have been examined as a model system for the preparation of high-efficiency DSSCs based on a novel metal-free organic dye. Conventional DSSCs are based on N719 (di-tetrabutylammonium-*cis*-*bis*(isothiocyanato)*bis*(2,2′-bipyridyl-4,4′-dicarboxylato) ruthenium(II)), the difference between the redox potential of the dye and the I/I_3^- redox couple is in excess of 600 mV. A novel metal-free organic dye (Carbz-PAHTDTT, S9) was used for this study. S9 affords excellent light-harvesting properties when used in conjunction with thin TiO_2 electrodes comprising a 2.2 μm mesoporous TiO_2 layer (particle size, 18 nm) and a 4.4 μm TiO_2 scattering layer (particle size, 400 nm). The combination of thin TiO_2 electrodes and organic dyes with high extinction coefficients has previously been proven to be beneficial for solid-state DSSCs based on organic charge transport materials, where accelerated charge recombination is of equal concern. The DSSC using S9 dye gives great energy conversion efficiency as high

as 7.16 % when assembled with PANI/CSA counter electrode, which is a more improved performance than conventional metal-based N719 DSSCs. Furthermore, it is clearly confirmed that the PANI/CSA counter electrode is a universal electrode which can be operated under the solar cell configuration using a novel organic dye.

4. A versatile route to overcome the limitations of printing nondispersive conducting polymer PPy was introduce by combining inkjet printing with vapor deposition polymerization (IJP-VDP) for the fabrication of top-contact S/D electrodes in flexible organic thin film transistors (OTFTs). PPy was chosen because it could be substituted for expensive Au electrodes and opened a way to pattern of nondispersive conducting polymer in common solvents. An initiator solution was deposited on the organic semiconductor layer by IJP, and subsequent exposure to vaporized monomers induced selective polymerization, producing a conducting polymer on the printed initiator. IJP-VDP is emerging as a useful method for printing an electrode pattern of nondispersive conducting polymers in top-contact OTFTs instead of metal electrodes. To the best of our knowledge, this is the first report of high-performance flexible pentacene transistors with top-contact S/D electrodes of a patterned conducting polymer using IJP-VDP, where illustrate the simplicity and versatility of the patterning process with a nondispersive conducting polymer.
5. A novel and reliable approach for the preparation of rGO transparent electrodes was studied through the combination of chemical and

subsequent pressure-assisted thermal reduction at relatively low temperature (180℃) on a flexible plastic substrate. This reduction process produces rGO electrodes without the transferring or imprinting processes used in conventional synthetic approaches for graphene thin film production. Furthermore, the electrical performance of the conductive film obtained by this process was enhanced due to the dense packing of each graphene sheet. The densified rGO film formed a uniform surface with low surface resistance, allowing in practical application to gate electrode of flexible OTFTs. In a proof-of-concept demonstration, the rGO thin film-gated OTFT exhibited superior device performance in terms of mobility and on/off ratio.

6. All-solution processed flexible OTFT was explored using PANI/CSA gate electrode as a key component. A highly conductive, flexible, and half-transparent gate electrode was prepared by spin-coating the PANI/CSA solution onto PES substrate. It showed splendid compatibility with its substrate, which lead to high flexibility. Ag source/drain electrodes were constructed by inkjet printing method on PETA insulating layer and 6,13-bis(triisopropylsilylethynyl)-pentacene (TIPS-pentacene) served as an active material. Optimizing TIPS-pentacene preparation condition such as various solvents and dissolution time make it possible to maximize the device performance.

2. Experimental details

2.1. Organic Electrodes for Chemical Sensor

2.1.1. PANI/CSA chemical sensor for NH_3 gas detection

2.1.1.1 Synthesis of PANI via interfacial polymerization

Water and $CHCl_3$ were mixed with volumetric ratio of 1 to 2, and then HCl (96 mmol) was added to the mixture. Aniline monomer (22 mmol) was dropped into the solution followed by vigorous stirring. APS solution was prepared by adding APS powder (11 mmol) to 5.76 M HCl solution (15 mL). At the desired reaction temperature, APS solution was introduced into the monomer solution. The obtained PANI was washed and dried to give green emeraldine salt form of PANI powder.

2.1.1.2. Fabrication of PANI/CSA film

As-prepared PANI was deprotonated with NH_4OH 1M aqueous solution. The dedoped PANI was rewashed followed by drying step. For the secondary doping, PANI and 10-camphorsulfonic acid (CSA) were mixed with molar ratio of 2 to 1 at the mortar. These mixture powders were dissolved in *m*-cresol and/or *m*-cresol/$CHCl_3$ co-solvent with 3 wt.-%. PANI/CSA solution was drop-casted onto a cover glass. After drying at 50 $^{\circ}$C, PANI/CSA films were obtained with average thickness 12 μm measured by field-emission scanning electron microscope (FE-SEM) images at the cross-sectional area of the films.

2.1.1.3. Fabrication of the sensor device

The free-standing PANI/CSA film was used for a transducing material. Small area (4.0 mm × 0.5 mm) of the PANI/CSA film was separated from the original film with scissors and immobilized to the surface of cover glass. Two copper wires were linked to both sides of the film by silver paste. After the assembled sensor device was dried *in vacuo* at ambient temperature, copper wires connected to sourcemeter and the signals were recorded on computer.

2.1.1.4. Sensitivity measurement of PANI/CSA film sensor

In order to evaluate the sensitivity of PANI/CSA film upon exposure to ammonia (NH_3) gas, the normalized resistance change was examined in real-time at a constant applied current of 10 μA. The normalized resistance change defined as $\Delta R/R_0 = (R-R_0)/R_0$, where R and R_0 symbolized the time-dependent resistance and the initial resistance. Reversibility and reproducibility of the fabricated sensor were measured by alternating exposures of NH_3 gas mixed with nitrogen (N_2) stream for 1 min and N_2 stream only for 4 min. The concentration of NH_3 was regulated by adjusting the flow of N_2 stream via mass flow controller.

2.1.2. Instrumental

Synthesis of emeraldine salt form and emeraldine base form of PANI was confirmed by Fourier transform infrared (FT-IR) spectroscopy with a Bomem MB 100 (Bomem Inc., Canada). Intrinsic viscosity of emeraldine base in THF

was measured by tuning-fork vibration method with SV-10 viscometer (A&D Ltd, Japan). Atomic force microscope (AFM) with a Digital Instruments D3100 (Veeco, USA) in tapping mode used for the surface morphology observation of the PANI/CSA films. The scan range of the film was 500 nm × 500 nm. FE-SEM images were obtained using a JSM-6701F (JEOL Ltd, Japan) instrument at an acceleration voltage of 10 kV. M18XHF-SRA (MAC Science Co., Ltd, Japan) X-ray diffractometer offered X-ray diffraction (XRD) patterns of the PANI/CSA films. The conductivities of the PANI/CSA films were measured by four-point probe technique with a Keithley 2400 (Keithley Instruments Inc., USA) sourcemeter and probe station. The probe used was made from tungsten carbide with a tip spacing of 1 mm and probe tip diameter of 12 μm. NH_3 gas flow concentration was manipulated by mass flow controller (MFC) SEC-4400 (STEC Inc., Japan). The resistance change of the sensor was monitored with a Keithley 2400 sourcemeter connected to a computer.

2.2. Organic Electrodes for Dye-Sensitized Solar Cell

2.2.1. TCO-free PANI/CSA counter electrode for a bifacial dye-sensitized solar cell

2.2.1.1. Preparation of PANI/CSA film

The aniline monomer purchased from Aldrich was used as received. APS (98.0 %) and CSA (98.0 %) were also obtained from Aldrich. Kokusan Chemical Co., Ltd (Tokyo, Japan) provided with *m*-cresol (98.0 %). Chloroform ($CHCl_3$) (99.0 %), hydrochloric acid (HCl) (35.0~37.0 %) and ammonia solution (NH_4OH) (28.0~30.0 %) were used as received from Samchun Chemical Co. (Seoul, Korea). Water and $CHCl_3$ were mixed at a 1:2 volumetric ratio followed by the addition of HCl (96 mmol). The aniline monomer (22 mmol) was dropped into the solution followed by vigorous stirring. The APS solution was prepared by adding the APS powder (11 mmol) to the 5.76 M HCl solution (15 mL). At the desired reaction temperature, the APS solution was introduced into the monomer solution. The obtained PANI was washed and dried to give the green emeraldine salt form of the PANI powder. The as-prepared PANI was deprotonated with a NH_4OH 1 M aqueous solution. The dedoped PANI was rewashed followed by a drying step. For secondary doping, PANI and CSA were mixed at 2:1 molar ratio with a mortar and pestle. These mixture powders were dissolved in *m*-cresol with 3 wt%. The solution was spin-coated on a glass substrate with holes and dried at 50 ℃. After drying, the PANI/CSA coated glass was heated on a hot plate at various temperatures for 30 min to determine the thermal treatment effect.

2.2.1.2. Electrode assembly for DSSCs

The μm-scaled TiO_2 films with an active area of 0.2 cm^2 were prepared by the deposition of a viscous TiO_2 paste (Ti-nanoxide D/SP, Solaronix Co.) on FTO glass (8 Ω cm^{-2}, Pilkington TEC glass™, USA). N719 dye (Ru[LL0-$(NCS)_2$], L=2,20-bipyridyl-4,40-dicarboxylic acid, L'=2,2'-bipyridyl-4,40-ditetrabutylammonium carboxylate, 0.5 mM, Solaronix Co.) was then adsorbed in the fabricated TiO_2 electrode as a sensitizer. The dye-adsorbed TiO_2 electrode was assembled with a counter electrode into a sandwich-type cell using thermal adhesive films (Surlyn: 30 μm, Dupont). A drop of the redox electrolyte was injected into the cell. The iodide redox electrolyte was a solution of methoxypropionitrile (MPN) dissolved 0.6 M 1-methyl-3-propylimidazolium iodide (MPII), 0.1 M LiI, 0.05 M I_2, 0.5 M *tert*-butyl pyridine (TBP).

2.2.2. PANI/CSA counter electrode for a novel organic dye-sensitized solar cell

2.2.2.1. Working electrode preparation

The glass substrate used was 4 mm thick 10 Ω/sq conductive FTO glass with high transparency in the visible range purchased from Nippon sheet glass. Mesoporous 4×4 mm TiO_2 films were printed using a commercial semi automatic screen printer and commercial 18 nm TiO_2 screen printing paste (PST-18NR, JGC Catalysts and Chemicals). The scattering paste was prepared from 400 nm particles mixed 5 to 1 by weight with 18 nm particles and an

additional 3.5 parts ethyl cellulose and 30.5 parts terpineol. After a first sinter process (500℃) a $TiCl_4$ treatment was applied by immersing the films in a 20 mM aqueous $TiCl_4$ solution and applying 70℃ heat for 30 min in a water saturated atmosphere. After another sintering process (500℃) the approximately 80℃ warm films were immersed in a solution of 0.2 mM Carbz-PAHTDTT and 20.0mM chenodeoxycholic acid in a 3 : 2 mixture of chloroform and ethanol over 12 hours. N719 dye was purchased from dyesol and used as 0.5 mM solution in 50% acetonitrile, 50% *tert*-butanol with a dying time of 12 hrs. The dyed films were washed in acetonitrile for 5 min to remove non-attached dye from the pores.

2.2.2.2. Electrolyte fabrication

All electrolytes used were prepared using anhydrous solvents, deoxygenated by freeze-drying and stored in a nitrogen glove box. Iodide, propyl-methyl imidazolium iodide (PMII), chenodeoxycholic acid (cheno) and guanidinium thiocyanate (GuSCN) were purchased from commercial suppliers in high purity and used as received. The *tert*-butylpyridine (*t*-BP) was distilled under nitrogen atmosphere and then stored in the glove box. After the addition of *t*-BP the cheno precipitated, but redissolved after 1 min of stirring.

2.2.2.3. Cell assembly

The dried working electrode and the counter electrode were assembled using a 25 μm thick Surlyn gasket (Solaronix) of the dimensions 5×6 mm. A

pneumatic finger was used to apply pressure while heating through the counter electrode. The cells were then transferred into a nitrogen glove box and vacuum backfilled through a predrilled hole in the counter electrode. The backfilling hole was sealed at 150℃ using a square of aluminium backed Surlyn prepared by melting 25 μm Surlyn onto aluminium foil at 100°C.

2.2.3. Instrumental

Atomic force microscopy (AFM, XE-70, Park Systems, Korea) in tapping mode was used to examine the surface morphology of the PANI/CSA films. The thickness and morphology of the PANI film were confirmed by FE-SEM (SUPRA 55VP, Carl Zeiss, Germany) at an acceleration voltage of 2 kV. Coil conformation changes of PANI influenced by thermal treatment were observed by using a UV/Vis/NIR spectrometer (JASCO V-570). Transmittances of PANI/CSA and Pt counter electrodes were measured by using a UV/Vis spectrometer (Scinco, S-3100). Cyclic voltammetry (CV, Potentiostat/Galvanostat, AUTOLAB PGSTAT30, Netherlands) was measured using an acetonitrile solution dissolved in 10 mM LiI, 1 mM I_2 and 0.1 M $LiClO_4$ as an electrolyte. The *in-situ* optical transmittance change during CV measurement was observed by He-Ne laser (λ = 633 nm) to indentify electrochromic properties. The photocurrent–voltage (*j*–V) characteristics of the assembled DSSCs and current transient measurement were evaluated using a 500 W xenon lamp (XIL model 05A50KS source units) with a light intensity of 1 sun (100 mW cm^{-2}), which was adjusted using an NREL fabricated Si

reference solar cell. The *j*–V characteristic test was carried out under front illumination and rear illumination. The incident photon-to-current efficiency (IPCE, PV measurements, Inc.) was measured from 300 nm to 800 nm under short circuit conditions. The electrical impedance spectra were measured using an impedance analyzer (IM6, Zahner elecktrik) at an open-circuit potential under 1 sun light illumination and a frequency ranging from 10^5 to 0.05 Hz. The Nyquist plot of electrical impedance spectra (EIS) was plotted by using the equivalent circuit model which presented in the literature [184]. The R_s denotes the resistance of the electrolyte and the TCO substrate. R_{ct} and R were the charge transfer resistance of the interfaces of the counter electrode/electrolyte and porous electrode/electrolyte, respectively. The finite Warburg impedance (W_s) related elements were influenced by the diffusion in the nanoparticle electrode/electrolyte interface.

A sun simulator (Oriel) fitted with a filtered 1,000W xenon lamp was used to provide simulated solar irradiation (AM1.5, 1,000W m^{-2}). Current–voltage curves were recorded using a Keithley 2400 source meter. The output of the light source was adjusted using a calibrated silicon photodiode (Peccell Technologies). The photodiode was fitted with a color filter provided by the supplier, to minimize the optical mismatch between the calibration diode and the dye-sensitized solar cells. The light intensity was adjusted by using a filter wheel equipped with a series of mesh filters.

2.3. Organic Electrodes for Organic Thin Film Transistor

2.3.1. Polypyrrole source/drain electrode by using inkjet printing-mediated vapor deposition polymerization for organic thin film transistor

2.3.1.1. Fabrication of source/drain electrode of OTFTs

The device was built on a flexible PES film. The Au gate electrode (50 nm) was thermally deposited on the PES substrate at a deposition rate of 1.0 Å·s^{-1}. Polyvinylphenol (PVP), a polymeric dielectric material, and poly(melamine-co-formaldehyde), a cross-linking agent, were dissolved in propylene glycol monomethyl ether acetate (PGMEA) (10 mL) at a molar ratio of 2:1. The PVP solution was spin-casted at 4000 rpm for 30 s and subsequently cross-linked at 130 ℃ for 15 min and 200 ℃ for 5 min in N_2 atmosphere, forming a ~300-nm PVP gate dielectric. On top of the cross-linked PVP dielectric layer, pentacene film was thermally evaporated in a vacuum chamber by a shadow mask under a pressure of 5×10^{-6} Torr at room temperature at a deposition rate of 0.4 Å·s^{-1}. The pentacene semiconductor was ~60 nm thick. Prior to IJP-VDP, the pentacene layer was treated with O_2 plasma (80 W for 1 s) at ambient pressure. The initiator solution, composed of APS (20 wt%) and PSS as an additive in distilled water (10 mL), was dropped on top of the pentacene active layer from the desktop printer cartridge (Cannon PIXMA IP 1300), in which the PSS concentration was varied from 0 to 12 wt%. Devices with printed initiator patterns were exposed to pyrrole monomer vapor in a vacuum chamber at 10^{-1} Torr for 10 min for VDP. For comparison,

devices based on Au S/D electrodes were also fabricated with an identical corresponding structure.

2.3.2. Graphene gate electrode by using pressure-assisted thermal reduction method for organic thin film transistor

2.3.2.1. Preparation of GO solution

Water-soluble GO powder was prepared by modified Hummer's method [147]. A mixture of graphite (1 g), $K_2S_2O_8$ (0.5 g) and P_2O_5 (0.5 g) was placed in H_2SO_4 (1.5 mL) solution at 80 ℃ for 6 h (all chemicals were purchased from Sigma Aldrich, Korea). Then, the mixed solution was diluted, filtered and washed sequentially on the filter with deionized water. The washed mixture was dried in a vacuum oven for overnight. Next, the peroxidated graphite (1 g) and $NaNO_3$ (0.5 g) were added to H_2SO_4 (23 mL) solution and placed in an icebath at 0℃ for 30 min. Then, $KMnO_4$ (3 g) was injected into the mixed solution and carefully stirred overnight. Deionized water was added to the mixed solution over 2 h and the temperature was increased to 98 ℃ slowly. Subsequently, 30 wt% aqueous H_2O_2 solution was added to the mixture and stirred for 3 h, producing a brown-colored slurry. The slurry was washed with 10 wt% HCl. Additional washing was performed with deionized water to neutralize the solution. Finally, GO powder was obtained after drying and a GO suspension was prepared by dispersing the GO powder in deionized water. The fabricated GO suspension was stable for several months without an external stimulus.

2.3.2.2. Preparation of the GO films on PES substrates

A final concentration of GO solution (2 mg/mL) was obtained by mixing of the GO suspension with ethanol at a volume ratio of 50% ethanol to water. Before the spin-coating process, the PES substrates were plasma-treated (200 W, 8 SCCM O_2) to modify their surface wettability. The substrates were completely covered with a sufficient amount of the GO suspension.

2.3.2.3. GO reduction

Hydrazine vapor reduction was performed prior to thermal reduction. The spin-coated GO thin films were placed in a clean glass chamber containing 1 mL of hydrazine (30%, Sigma Aldrich). The chamber was sealed and placed in an oven at 100℃ for 1 h. The color of the GO thin films changed from brown to metallic gray by chemical reduction. Thermal reduction was carried out following hydrazine vapor reduction. The sample was heated to 180℃ at a heating rate of 5℃ min^{-1} in a tubular furnace under an argon atmosphere, and held at 180℃ for 30 min. Pressure-assisted thermal reduction was carried out inside a glovebox following hydrazine vapor reduction. The sample was placed in a a hot press between stainless-steel plates at 180 ℃ for 30 min.

2.3.2.4. Fabrication of the organic thin film transistor

The OTFTs were fabricated with a bottom-gate and top-contact configuration. The as-prepared PRGO thin film on the PES substrate was used as a gate electrode. Polyvinylphenol (PVP), a polymeric dielectric material,

and poly(melamine-co-formaldehyde), a cross-linking agent, were dissolved in PGMEA (10 mL) at a molar ratio of 2:1. The PVP solution was spin-casted at 4000 rpm for 30 s and subsequently cross-linked at 130℃ for 15 min and 200℃ for 5 min in N_2 atmosphere, forming an about 300 nm PVP gate dielectric. On top of the cross-linked PVP dielectric layer, pentacene film was thermally evaporated in a vacuum chamber by a shadow mask under a pressure of 5×10^{-6} Torr at room temperature at a deposition rate of 0.4 Å s^{-1}. The pentacene semiconductor was about 60 nm thick. The gold S/D electrode (50 nm) was thermally deposited on the PES substrate at a deposition rate of 1.0 Å s^{-1}.

2.3.3. PANI/CSA gate and Ag souce/drain electrode by using inkjet printing method for organic thin film transistor

2.3.3.1. Formation of PANI/CSA gate electrode

A flexible PES film was used as a device substrate. PANI/CSA solution was prepared by as-mentioned method and spin-coated onto the PES film for the gate electrode. PANI/CSA electrode was dried on the hot plate at 100 ℃ for 12 h.

2.3.3.2. Fabrication of OTFTs with Ag source/drain electrode

Gate insulating layer was formed by spin-coating of acrylate resin. 1 wt% of Diphenyl(2,4,6-trimethylbenzoyl)phosphine oxide (Sigma Aldrich, Korea) as photo-initiator was dissolved into pentaerythritol triacrylate (Sigma Aldrich,

Korea) and the solution was stirred for 48 h. PANI/CSA gate electrode was coated with the resin by spin-coating for gate insulation. Mercury lamp (300 W) irradiated UV light to the resin for photocuring. The Ag electrode of the device was constructed on the resin layer by inkjet printing of the silver dispersion (20 wt% Ag) containing 10 wt% propylene glycol and 0.05% of BYK 348 as wetting agents. The printing was performed by an Omnijet 200 printer (Unijet Co., LTD, Korea) with 30 pL (Samsung) printheads. Uniform droplet effluence was achieved by applying 5 s long 50 V pulse at a frequency of 500 Hz. The printed pattern was sintered under N_2 atmosphere in the glove box at 150 ℃ for 30 min. 6,13-bis(triisopropyl-silylethynyl) pentacene (Sigma Aldrich, Korea) was used as an active material. 2 wt% of TIPS-pentacene was dissolved into various solvents for from 3 to 48 h.

2.3.4. Instrumental

Optical micrographs were acquired using a Leica DM2500 P. Infrared spectra were recorded using a Bomen MB 100 FTIR spectrometer. The plasma reactor was a parallel-electrode type with a 13.56-MHz radio-frequency generator. The conductivity of the printed PPy electrode was confirmed using four-probe measurements (Keithley 2400 source meter) at 25℃. The sheet resistance was averaged for 10 different locations in a PPy electrode. Transistor performance was characterized using an Agilent HP4155C semiconductor parameter analyzer (Agilent, Santa Clara, CA, USA). Capacitance voltage characteristics of the metal–insulator–metal (MIM)

capacitors were measured using an HP 4284 precision LCR meter (Agilent, Santa Clara, CA, USA). Thicknesses of the thin films were measured using a profilometer (ET 3000, Kosaka Laboratory, Ltd.). X-ray photoelectron spectroscopy (XPS) was performed using an ASCALab220i-XL electron spectrometer form VG Scientific (Cedex, France) with 300 W Al Kα radiation at a base pressure of 3×10^{-9} mbar. High power XRD measurements were carried out using an M18XHF-SRA (Mac Science, Yokohama, Japan) diffractometer equipped with a Cu Kα radiation source (k = 1.5406 A) at 40 kV and 300 mA (12 kW). The XRD peaks were collected between 10° and 40° at a scan rate of 4 min^{-1}. Contact angles were determined with a DSA10 contact angle analyzer (Krüss, Matthews, NC, USA) interfaced to drop shape analysis software. Electrical resistance was measured using a 2400 sourcemeter (Keithley, Cleveland, OH, USA) at 25 ℃ by a four-probe method. FE-SEM images were acquired with JSM-6700F microscope (JEOL, Tokyo, Japan) at an acceleration voltage of 10 keV. Film transmittance was measured using a UV–visible spectrometer (Lamda-20; Perkin-Elmer, Waltham, MA, USA) at a resolution of 1 nm. AFM (XE-70; Park Systems, Suwon, Korea) in tapping mode was used to examine the surface roughness of RGO thin films. Transmission electron microscopy (TEM) images were acquired with a JEOL JEM-200CX microscpoe at an acceleration voltage of 200 kV. For the microtome process, SPURR's kit resin (Electron Microscopy Sciences, Fort Washington, PA, USA) was mixed with the powder MSNF, and cured for 24 h at 70℃. Electrical resistance of PANI/CSA gate electrodes was measured by

using a four-point probe method with a Keithley 2400 sourcemeter (Keithley, Cleveland, OH, USA) at 25 ℃. Optical micrographs were acquired by using an Eclipse LV100POL microscope (Nikon Instruments Inc., Japan). AFM (XE-70, Park Systems, Korea) was used to examine the surface morphology of the PANI/CSA gate electrodes and TIPS-pentacene crystals. FE-SEM and focused ion beam (FIB; Carl Zeiss, Auriga, Germany) were used to investigate the interface between PANI/CSA gate electrodes and a PES substrate. UV/Vis transmittance of the PANI/CSA gate electrodes was measured by using a PerkinElmer Lambda 35 spectrometer.

3. Results and Discussions

3.1. Organic Electrodes for Chemical Sensor

3.1.1. PANI/CSA chemical sensor for NH_3 gas detection

During the past few decades, conducting polymers including PPy [148], PANI [149], PT [150] and PEDOT [151] have been widely investigated due to their fascinating electrical properties. Extensive researches of conducting polymers have been performed for improving the conductivity and mainly focused on the conversion of insulating polymer into metal-like conducting material [152]. In particular, PANI has several advantages such as simple synthetic route, good environmental stability, high yield, and tunable conductivity. Because of these superiorities, precedent achievements have been reported in the view point of the various applications [153].

Representative characteristics of PANI embrace the insulators in the pristine form and the conductors after doping (or protonating). The conducting form of PANI is called emeraldine salt, which is made from protonation of the imine nitrogens in the insulating form of PANI (emeraldine base). In general, strong acids with small size such as hydrochloric acid [154], fluoroboric acid [155] and sulfuric acid [156] have been used for the dopant. In the case of small molecule dopants, however, the conductivities are reduced at room temperature due to dopant evaporation [157]. By contrast with the above doping process, the concept of secondary doping was suggested by MacDiarmid et al. [158] Dodecylbenzylsulfonic acid [159], *p*-toluenesulfonic

acid [160] and polymeric acids [161] have been employed as a secondary dopant but the highest conductivity was obtained using PANI doped with CSA in *m*-cresol solvent [162]. Ikkala et al. reported that the optimized conformation of PANI was formed with CSA in *m*-cresol [163]. As a result, several studies have been conducted for the PANI/CSA complex system and their applications [164,165]. However, there was limited information concerning $CHCl_3$ as a solvent of PANI/CSA system because the PANI/CSA in $CHCl_3$ exhibited low conductivity due to poor solubility [162].

In addition, conducting polymers have been used for signal transducer of chemical sensor to detect target species [166,167]. However, PANI/CSA system has been scarcely applied for chemical sensor. In this paper, the PANI/CSA films were directly utilized as a signal transducer for the detection of NH_3 gas. It is a colorless gas with a pungent and suffocating odor and recognized as one of the primary irritants to humans. The limit of human exposure is known as approximately 20 ppm of NH_3 gas [168]. Therefore, the detection of toxic gas is the pivotal issue in fields of industrial processing, clinical diagnosis, and environmental monitoring.

In this part, conductivity enhancement of PANI/CSA films was investigated in the viewpoint of $CHCl_3$ amount in *m*-cresol solvent. A novel *m*-cresol/$CHCl_3$ co-solvent system was introduced to dissolve PANI/CSA powder. Highly conductive PANI/CSA films were successfully fabricated and the average conductivity of resultant film was measured to be over 600 S cm^{-1}. Furthermore, the PANI/CSA films could be applied directly to NH_3 gas sensor

without any patterned microelectrodes. The fabricated sensor had high sensitivity of NH_3 gas as low as 2 ppm and the electrical responses represented reversible and reproducible behavior.

Emeraldine salt form of PANI should be dedoped by strong base in order to apply solution process because it is scarcely soluble in aqueous and/or organic solvents. The dedoped PANI, i.e. emeraldine base, is easily soluble in organic solvents including *m*-cresol, tetrahydrofuran (THF), and N-methyl-2-pyrrolidone (NMP). Therefore, dedoping process is necessary to make a PANI film. **Figure 4** shows SEM images of PANI powders before and after dedoping. PANI prepared by interfacial polymerization exhibits fibril network structure and its dimension is nanoscale. The diameter of PANI nanofiber is slightly reduced after dedoping but overall morphology and network structure are preserved. Viscosity measurement was conducted to characterize emeraldine base form of PANI in THF solution. The obtained intrinsic viscosity [η] was 0.545 g dL^{-1} at 23 ℃. Mark-Houwink equation ([η] = KM^{α}) was used for the calculation. The viscosity average molecular weight ($\bar{M}_v$) of PANI was found to be 56 200 by the approximation of taking the K and α values of emeraldine base/N-methyl-2-pyrrolidone/2-methylaziridine (EB/ NMP/2MA) system (K = 1.2×10^{-4} and α = 0.77) [169] because the K and α values for PANI in THF were not known. Furthermore, FT-IR spectra in **Figure 5** were suggested to charaterize emeraldine salt and base forms of PANI. The peaks at 1590 and 1165 cm^{-1} correspond to the quinoid unit (N=Q=N)

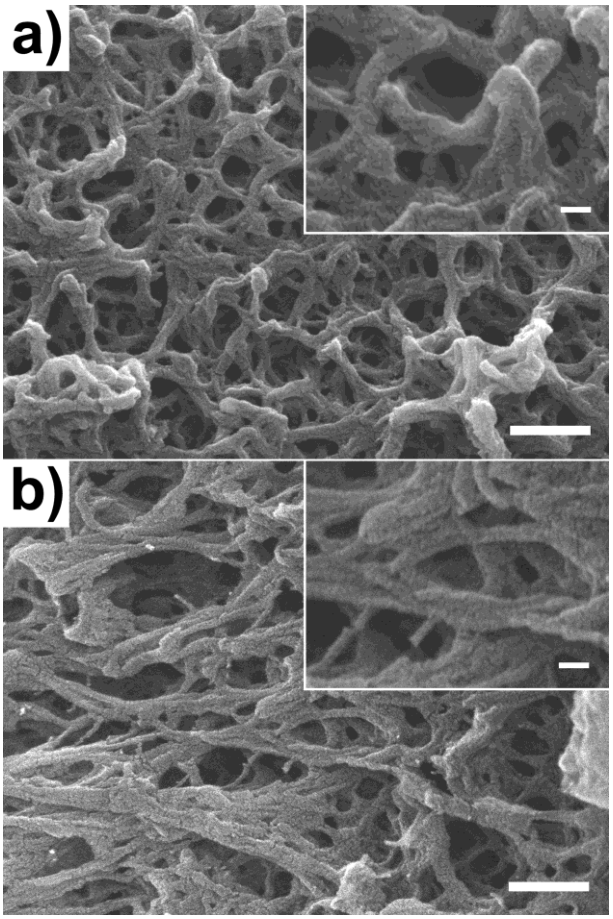

Figure 4. SEM images of (a) emeraldine salt form and (b) emeraldine base form of PANI powders and insets are magnified images. Scale bars represent 200 nm and insets are 20 nm.

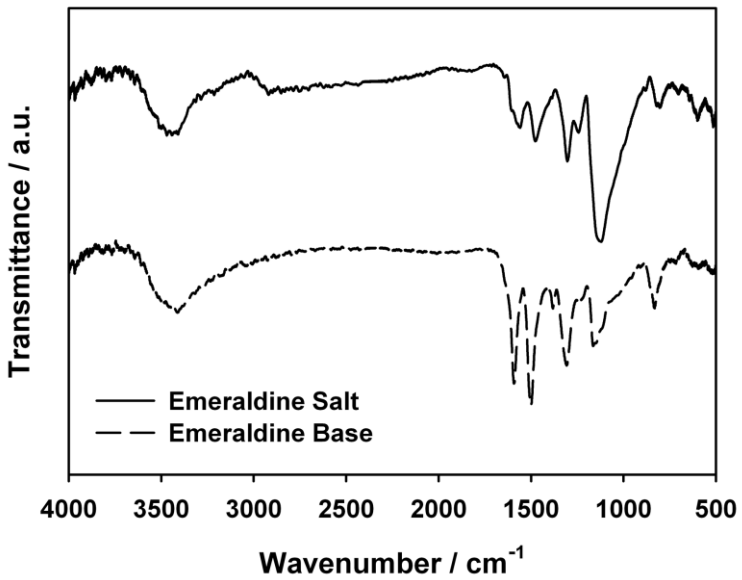

Figure 5. FT-IR spectra for emeraldine salt form and emeraldine base form of PANI.

and the band at 1500 cm^{-1} is resulted from the benzenoid unit (N−B−N). The peaks at 1310 and 830 cm^{-1} are ascribed to the stretching vibration of C−N and out-of-plane bending vibration of C−H on *para*-disubstituted rings, respectively. In addition, the band at 1160 cm^{-1} was assigned as the "electronic-like band" [170]. Jing et al. explained that this intense and broad band is due to a vibrational mode of $B-\overset{+\bullet}{N}H-B$, which was formed in doping process [171] and the band diminished after dedoping. Judging from these data, it could be confirmed that emeraldine salt form of PANI was successfully synthesized and converted to emeraldine base form by deprotonation.

A brief fabrication procedure of PANI/CSA film is illustrated in **Figure 6**. Emeraldine base form of PANI powder was mixed with CSA and contained in a vial with 3 wt% of solvent. Then *m*-cresol or *m*-cresol/$CHCl_3$ co-solvent was added in the vial to dissolve PANI/CSA powder. PANI/CSA solution was drop-casted onto a cover glass with 0.25 mL of solution. It was dried at 50 °C for 8 h to fabricate highly conductive PANI/CSA film. **Figure 7** indicates the conductivity of PANI/CSA films as a function of $CHCl_3$ concentration. Conductivity values were calculated from sheet resistance and film thickness. Typical 4-point probe technique was used for the measurement of sheet resistances. Film thickness was determined by cross-sectional SEM images of PANI/CSA films. The best average conductivity was 640 S cm^{-1} at 20 vol% of $CHCl_3$. Conductivity increased more than two times by simply adding 20 vol% of $CHCl_3$ into the solvent compared to the case without $CHCl_3$. The

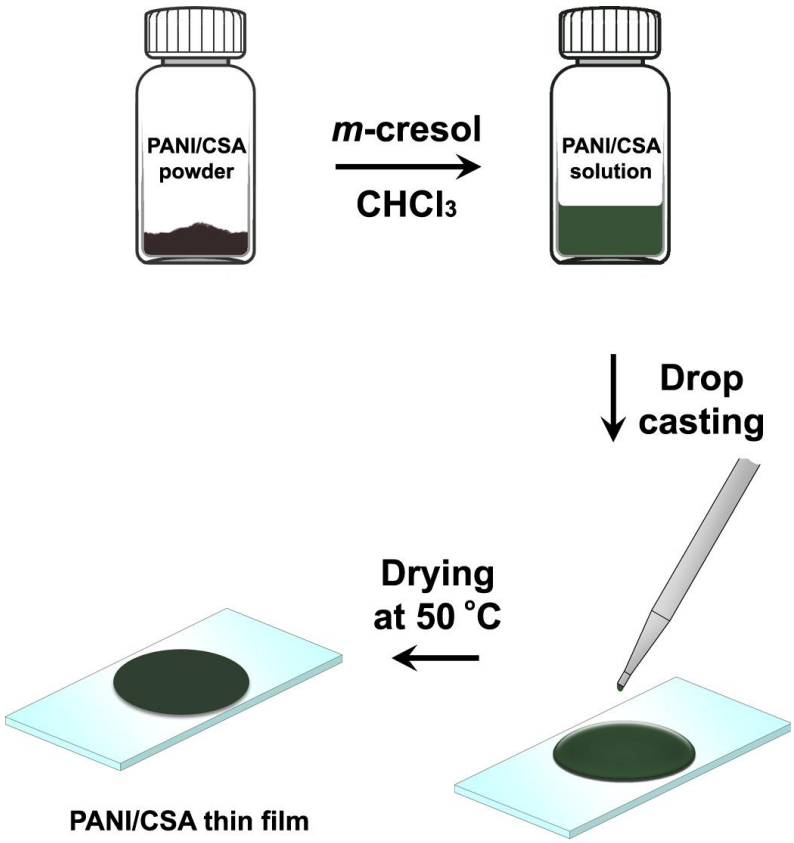

Figure 6. Schematic diagram for synthetic procedure of PANI/CSA film.

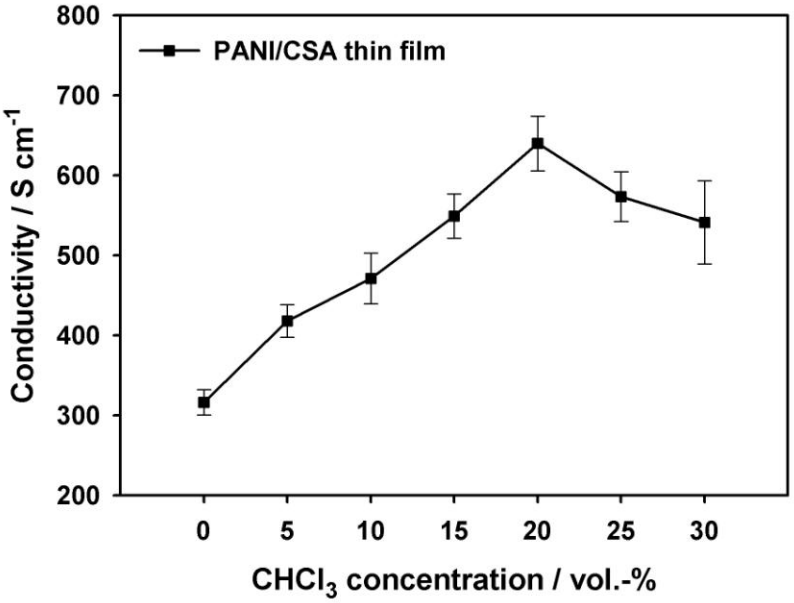

Figure 7. The conductivity variations of PANI/CSA films as a function of $CHCl_3$ concentration in *m*-cresol solvent.

conductivity of PANI/CSA films increased with increasing $CHCl_3$ concentration up to 20 vol% and decreased at 25 and 30 vol%. From this result, it can be concluded that the conductivity of PANI/CSA films was strongly affected by the $CHCl_3$ concentration in *m*-cresol solvent.

In general, there are some difficulties in dissolving PANI/CSA powder because *m*-cresol acts as a coagulant, resulting in PANI gels [172]. Some of these powders were dissolved into *m*-cresol and the remainder formed PANI gels. The quantity of dissolved PANI/CSA powder should be increased and the formation of PANI gels should be hindered to fabricate PANI film with high conductivity. Thus *m*-cresol/$CHCl_3$ co-solvent system was introduced to increase dissolving weight percent of PANI/CSA powder. There are two reasons choosing $CHCl_3$ as a co-solvent. One is that PANI/CSA shows low solubility in $CHCl_3$ [162] and the other is that $CHCl_3$ evaporates much faster than *m*-cresol due to the volatility difference. Under the same concentration, the amount of PANI gels formed by coagulation is almost same regardless of whether the solvent is *m*-cresol only or *m*-cresol/$CHCl_3$. In the case of using *m*-cresol/$CHCl_3$ co-solvent, PANI/CSA powder is dissolved in *m*-cresol selectively and $CHCl_3$ is elimiated rapidly during the drying step. As a result, the weight percent of PANI/CSA in the solvent increased with decreasing coagulation. The increase in dissolution of PANI/CSA powder facilitates the formation of PANI/CSA/*m*-cresol complexes. It has been reported that PANI chain, CSA, and *m*-cresol form the geometrically optimized structure [163]. The formation of complexes causes unraveling of compact PANI chains

subsequently, leading to the expanded-coil conformation [173]. Since the grains consist of PANI chains, expanded-coil conformation also results in grain growth [174]. Therefore it could be explained that the addition of $CHCl_3$ invokes the expansion of PANI/CSA grains eventually. However, it was impracticable to increase weight percent of PANI/CSA powder from the beginning of the process. In the case that the concentration of PANI/CSA exceeded 3 wt%, film forming was unfeasible since all the powders turned into PANI gels.

Surface morphologies of PANI/CSA films were inspected in order to elucidate the grain growth. **Figure 8** shows SEM images of PANI/CSA films as a function of $CHCl_3$ amounts. Cross-sectional images were also obtained to measure the film thicknesses for conductivity calculation. SEM images demonstrated that the grain size of PANI/CSA increased gradually with increasing $CHCl_3$ concentration. As mentioned previously, expanded-coil conformation led to grain growth of PANI/CSA. Grain growth, in turn, reduced contact resistances among the PANI/CSA grains [175]. Contact resistance means the electrical resistivity arose from when the charges pass through a contact surface between the grains. In the case of small grains, charges would meet more grain interfaces than the case of large grains if the charges travel same distance. These little contact resistances are accumulated over the whole film and finally led to conductivity decrement. Therefore the grain growth caused by $CHCl_3$ produces the reduction of contact resistance, resulting in the improvement of conductivity. However, it has been revealed

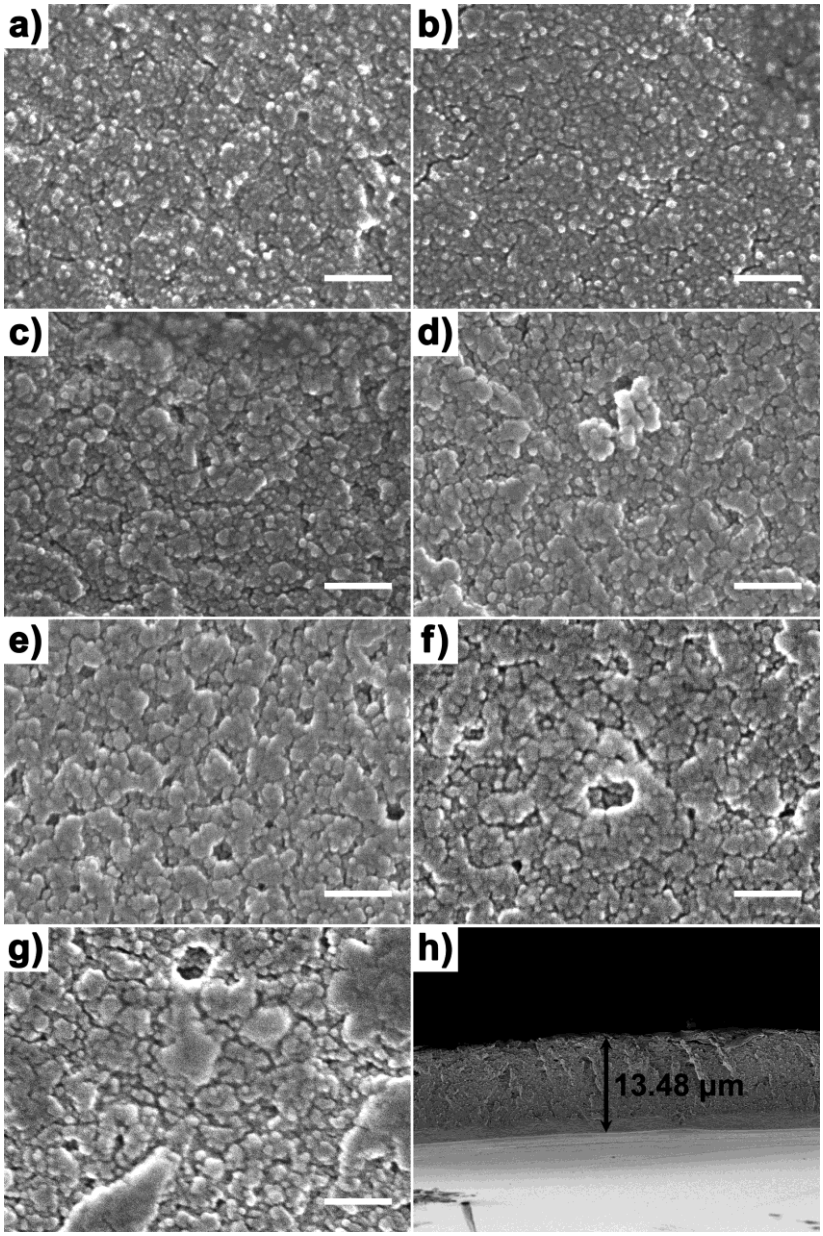

Figure 8. SEM images of the PANI/CSA films: $CHCl_3$ amounts are (a) 0, (b) 5, (c) 10, (d) 15, (e) 20, (f) 25, and (g) 30 vol%. The image (h) shows the cross section of film (g). All scale bars are 100 nm.

that the conductivity of PANI/CSA film started decreasing from 25 vol% of $CHCl_3$ in spite of grain size growth. Surface topographies were investigated by AFM to contemplate the relationship between the conductivity decrease and the roughness of the film. They have been expressed in **Figure 9** with their height profiles as a function of $CHCl_3$ concentration. The AFM images obviously confirmed that PANI/CSA grains expanded with increasing $CHCl_3$ amount as same as the SEM images. In particular, generation of gaps was discovered in the film with 25 and 30 vol% of $CHCl_3$ and these results coincided with SEM images of **Figure 8(f) and (g)**.

The surface topographies of PANI/CSA films with 25 and 30 vol% of $CHCl_3$ (**Figure 9(f) and (g)**) are apparently distinguishable from the others. The PANI/CSA films with 0, 5, 10, 15, and 20 vol% of $CHCl_3$ exhibited analogous morphologies, while the film with 25 and 30 vol% of $CHCl_3$ had gaps between the PANI/CSA grains on a whole surface. The intergrain gap was originated from the higher volatility of $CHCl_3$ (boiling point: 61.2 $^{\circ}C$) compared with *m*-cresol (boiling point: 202.8 $^{\circ}C$). As the amount of $CHCl_3$ increased up to 25 vol%, fast evaporation of $CHCl_3$ induced splits on the PANI/CSA film surface during the drying step. The presumption was supported by height profiles shown in **Figure 9** and definitely different profiles were exhibited in **Figure 9(f) and (g)**. The fissured surface morphology has a close relationship with the decrease of conductivity. In other words, the conductivity variation is affected by surface roughness because the sheet resistance is directly influenced by charge flow along a surface. The charge

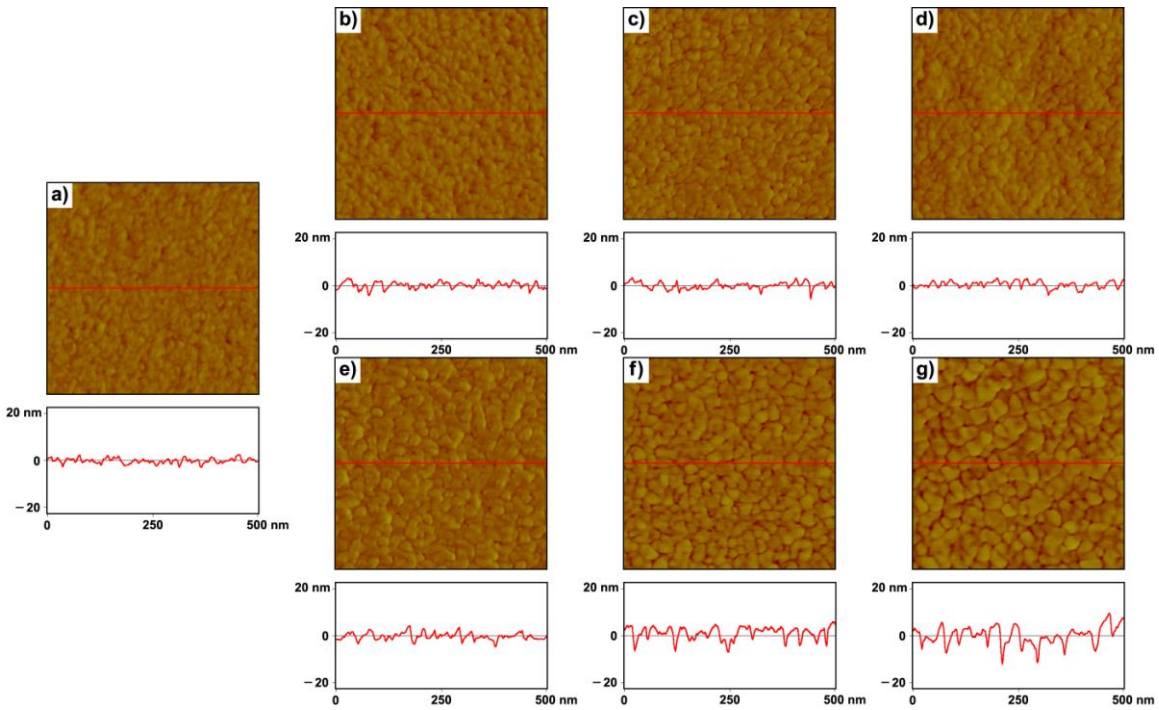

Figure 9. AFM images of PANI/CSA films and their height profiles: $CHCl_3$ amounts are (a) 0, (b) 5, (c) 10, (d) 15, (e) 20, (f) 25, and (g) 30 vol%.

flow is hindered by intergrain gaps acting as trap states for the charge carriers [176], and then the intergrain gaps and the recessed regions played a role in restricting the overall carrier mobility [177]. Moreover, when the charges move from one grain to next, they should go round fissured state, which causes the extension of electronic pathway. These tiny increments of resistivity were accumulated within the entire film and finally led to conductivity decrement. Subsequently, the conductivity of PANI/CSA film with 25 and 30 vol% of $CHCl_3$ decreased compared to the film with 20 vol% of $CHCl_3$ due to these effects.

To investigate the capability of PANI/CSA films as a transducer for detecting NH_3 gas, PANI/CSA solution was fixed at 30 vol% of $CHCl_3$ because the existence of spatial gaps on the film provided a larger surface area [178]. **Figure 10** illustrates the assembly procedure of chemical sensor using PANI/CSA film as a transducing material. At first, the fabricated PANI/CSA film was detached from a cover glass. Right size (4.0 mm × 0.5 mm) of PANI/CSA film was separated with scissors. Silver paste immobilized the severed film on a slide glass and connected with two copper wires simultaneously. After drying in the vacuum oven, revealed part of copper wire and silver paste in the connection point were sealed with common cellophane tape in order to increase signal-to-noise ratio. Area acting as a signal transducer was about 2.0 mm × 0.5 mm actually. A four-terminal I-V measurement was performed to record the resistance by measuring the voltage across the wire at a constant current of 10 μA. The normalized resistance change ($\Delta R/R_0$) of the

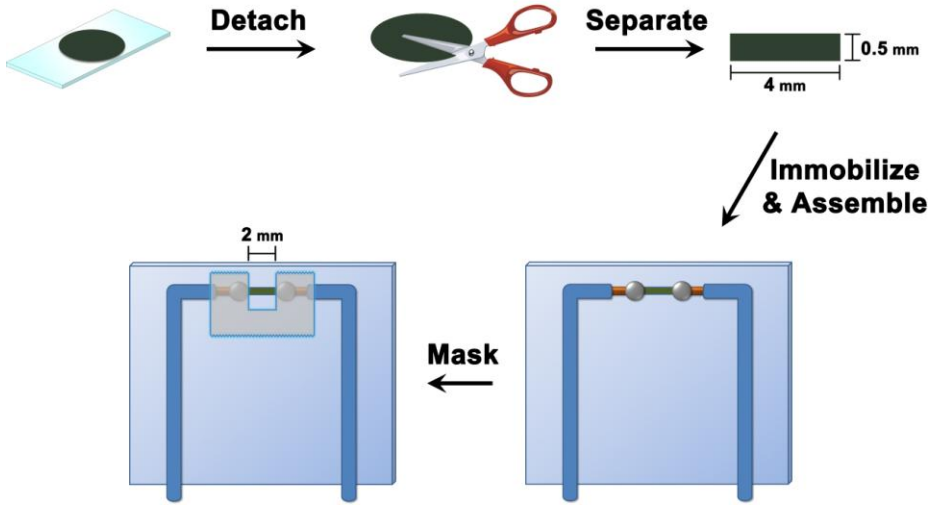

Figure 10. Schematic diagram for assembly procedure of chemical sensor using PANI/CSA film.

sensor was monitored in real time at 25 °C.

Figure 11 shows the electrical responses of PANI/CSA film upon cyclic exposures to various NH_3 gas concentrations and nitrogen (N_2) streams. In general, the dedoping process of PANI exhibits a low sensitivity and a slow response time compared with the acid doping [179]. Consequently, reversibility and reproducibility of the fabricated sensor were measured by periodical exposures to NH_3/N_2 mixed stream for 1 min followed by N_2 stream only for 4 min. The resistance of PANI/CSA film rapidly increased when the film was exposed to NH_3 gas. After NH_3 gas exposure was terminated, the resistance decreased immediately. The detachment of NH_3 molecules successfully achieved from the internal surface of the film. The cyclic tests denoted similar responses more than five times. These results suggest that the PANI/CSA film can be reversibly used in detecting NH_3 gas.

Figure 12 displays the sensitivity change of PANI/CSA film as a function of NH_3 gas concentration. The sensitivity was defined as the normalized resistance change measured when the sensor device exposed to NH_3 gas for 1 min. The sensitivity change demonstrated a nearly linear behavior over a whole range of NH_3 concentrations. This implied that sufficient imine-nitrogen sites existed on the surface of PANI/CSA film. Spatial gaps on the film surface provide an increment of overall surface area. It was known that the transducers consisting of nanomaterials such as nanoparticles, nanorods, and nanotubes showed better sensing performances because they have larger surface area than films [180]. In the case of fissured PANI/CSA films, extended surface area

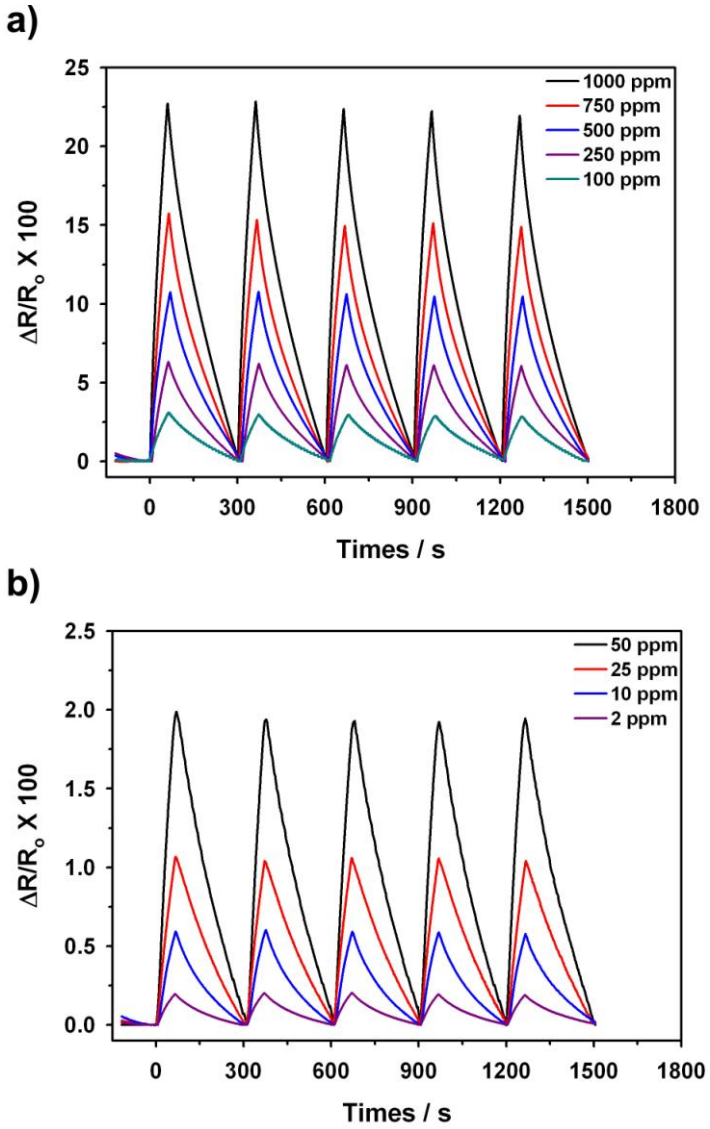

Figure 11. Responses of PANI/CSA film upon cyclic exposures to different NH_3 gas concentrations.

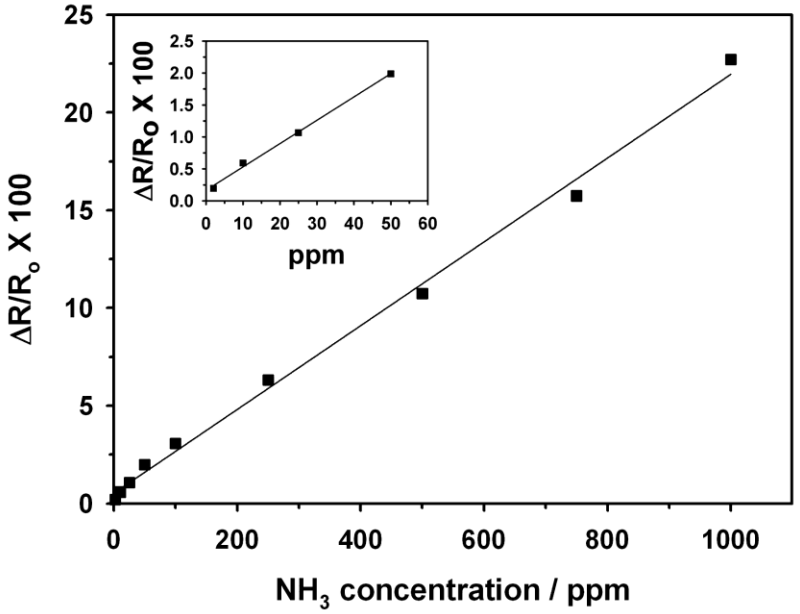

Figure 12. Sensitivity change of PANI/CSA films as a function of NH_3 gas concentration.

accommodates the PANI/CSA transducer to enhance the sensitivity and real-time response. This PANI/CSA film sensor can be convenient and efficient for detecting analytes and directly applicable for constructing chemical sensor assemblies without any patterned microelectrodes.

3.2. Organic Electrodes for Dye-Sensitized Solar Cell

3.2.1. TCO-free PANI/CSA counter electrode for a bifacial dye-sensitized solar cell

DSSCs have attracted considerable interest as a promising candidate for future energy generating devices [181]. They usually consist of a layer of titanium dioxide (TiO_2) nanocrystals with dye, a redox electrolyte containing I^-/I_3^- ion pairs, and a counter electrode coated with a platinum (Pt) catalyst on TCO glass [182]. In these elements of DSSCs, the counter electrode serves to transfer electrons from an external circuit to triiodide and reduce triiodide ions. The platinized TCO such as In-doped SnO_2 (ITO) or F-doped SnO_2 (FTO) was typically used as a counter electrode. However, Pt is a noble metal with high cost, and the preparing Pt counter electrode is complex and high energy-consuming [183]. Therefore, the preparation of an alternative counter electrode is needed to achieve efficient fabrication cost of DSSCs. Recently, many researches related to new counter electrode have concentrated on Pt-free electrodes. The various carbon-based materials have received much attention as a promising alternative to Pt. The Grätzel group has reported approximately 10 % maximum performance with activated carbon [184]. The other approach of applying new inorganic materials such as WC or CoS in counter electrode showed good photovoltaic efficiency [185]. The conducting polymers including PANI [186] or PEDOT could also be applied to DSSC as efficient counter electrodes [187]. Maximum cell efficiency over 7 % was obtained because of the good electrocatalytic activity of these materials. Among the

various conducting polymers, PANI is one of the most widely investigated conducting polymer material owing to its outstanding redox reversibility, environmental stability, low cost, and facile synthesis [188]. Accordingly, doped PANI has been studied for conducting polymer materials over the last decades [189]. Emeraldine salt (ES) state PANI presents electrocatalytic activity of iodide reduction, which has attracted a lot of interest in counter electrodes of DSSC. Wu group [190] applied microporous PANI with 100 nm nanoparticles coated on FTO film to a counter electrode of DSSC and this device achieved high cell efficiency. Deng [191] and Shin group [192] utilized anion-doped PANI deposited on FTO film as a counter electrode of DSSC. However, TCO which used in general DSSC electrode also has a drawback of cost originating from an expensive fabrication process, the efforts of reducing TCO electrodes in DSSC device are greatly interested in the viewpoint of production cost and some research groups have reported good results [193].

This study was focused on the replacing expensive Pt and TCO into a conducting polymer. The conventional platinized TCO glass counter electrodes (**Figure 13(a)**) are used as a catalyst layer and a charge transport layer, respectively. On the other hand, Pt and TCO-free counter electrode used in this paper functions two things in a single layer simultaneously (**Figure 13(b)**), which is prepared using materials with high catalytic activity for I_3^- reduction and rapid charge transport ability. In this part, camphorsulfonic acid-doped PANI (PANI/CSA) films were synthesized with high conductivity and excellent catalytic ability through simple spin-coating process. The PANI/CSA

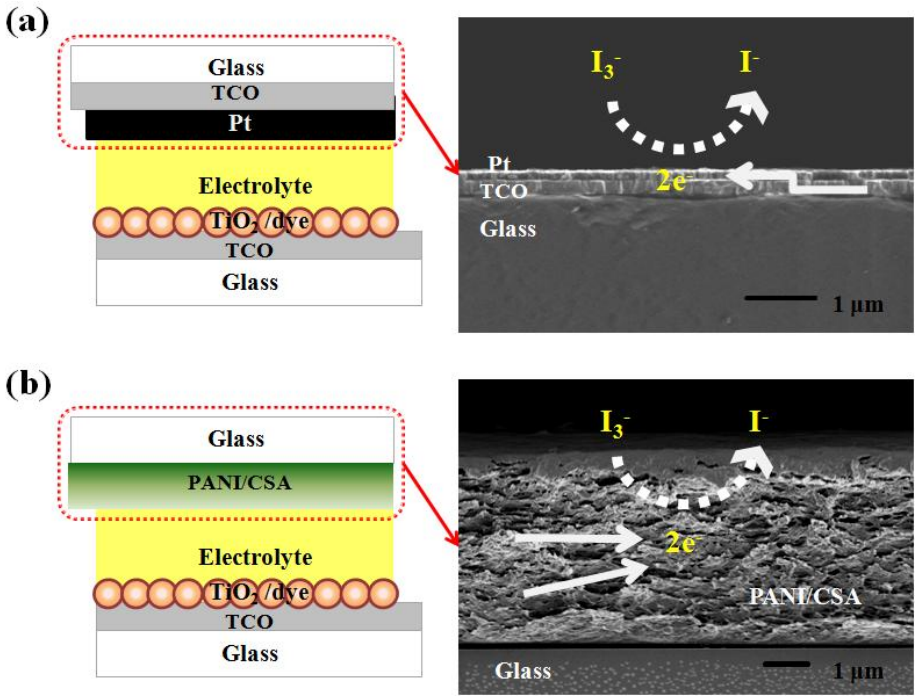

Figure 13. Schematic diagrams of the DSSCs; (a) DSSCs with the conventional counter electrode (Pt and TCO) and (b) DSSCs with Pt and TCO-free counter electrode.

spin-coated on normal glass substrate was successfully assembled as a counter electrode of DSSC. This film also can be operated by introducing light from both photoanode and counter electrode sides due to transparency of the PANI/CSA film. Bifacial DSSCs can exploit solar light source more efficiently, and will be more preferable for their versatile applications as power-generating windows, especially in the area of BIPV [186]. The assembled bifacial DSSC using the transparent PANI/CSA counter electrode presented excellent conversion efficiency of 5.50% from front illumination and 2.67% from back illumination. These results illustrate the promising potential for effective bifacial DSSC with Pt and TCO-free counter electrode by PANI/CSA film. Furthermore, electrochemical properties of the PANI/CSA film coated on TCO-free glass substrate as a counter electrode and optical transmittance changes with electrochromism properties were analyzed.

A counter electrode should have electrocatalytic activity for triiodide reduction. **Figure 14** demonstrates the comparison of the CV curves for I^-/I_3^- redox about PANI/CSA film on glass and platinized ITO. According to the CV curves in **Figure 14**, the PANI/CSA film on glass showed a much higher anodic peak current of 3.7 mA cm^{-2} and cathodic peak current of −1.8 mA cm^{-2} while the platinized ITO exhibited a anodic peak current of 1.8 mA cm^{-2} and a cathodic peak current of −1.6 mA cm^{-2}. As can be seen in **Figure 15**, the cathodic current density slightly changed after 100 CV cycles from −0.5 V to +1.0 V (vs. Ag/AgCl (sat. KCl)) at 100 mV s^{-1}. This result suggests that the PANI/CSA film on glass has good reversibility and stability in the I^-/I_3^- redox

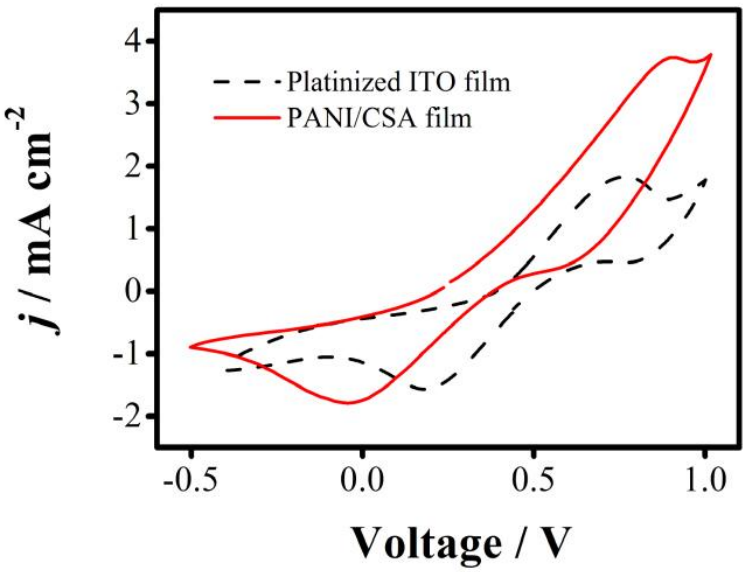

Figure 14. Comparison of redox performances of PANI/CSA counter electrode and the platinized TCO counter electrode under iodide redox electrolyte; CV curves of the PANI/CSA film and Pt on ITO glass at 50 mV s^{-1}.

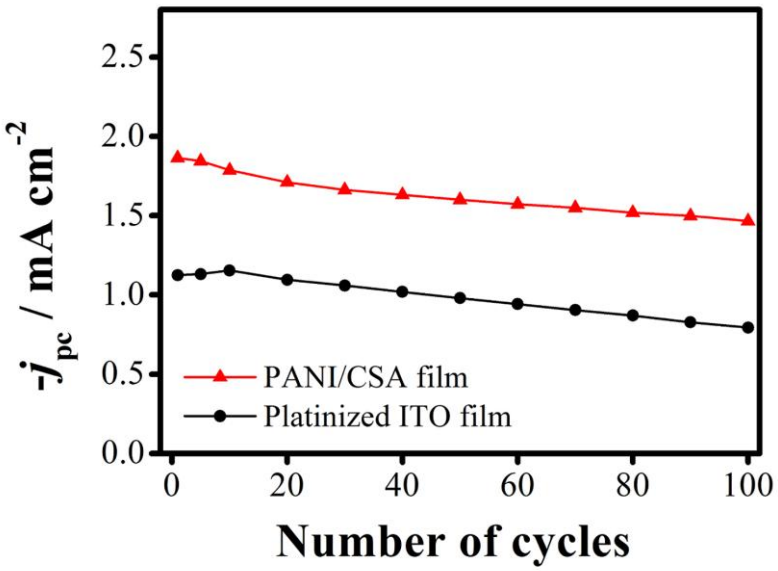

Figure 15. Comparison of redox performances of PANI/CSA counter electrode and the platinized TCO counter electrode under iodide redox electrolyte; the changes in the cathodic peak current density (j_{pc}) during 100 CV cycles.

couple compared to platinized ITO film [189]. **Figure 16** indicates a linear relationship between the scan rate and cathodic peak current. The adsorption of iodide species was slightly affected by the redox reaction on the PANI electrode surface, but the major rate-determine step of the reaction was diffusion process [190]. In addition, the twice larger slope of the PANI/CSA film was also attributed to the faster redox reaction, even though this polymer electrode was constructed on a TCO-free substrate. Therefore, it can be ascertained that PANI/CSA coated on TCO-free glass shows superior electrocatalytic activity for triiodide reduction.

It was considered that the major factors to improve performance of the PANI/CSA counter electrode were thickness of the film and thermal treatment temperature. Above all, the thickness of the PANI/CSA film strongly affected the performance of the DSSCs. The revolutions per minute (RPM) speed were changed to control the thickness of film. The FE-SEM images of **Figure 17(a)-(c)** reveal that the thickness of films deposited with 500 RPM, 1000 RPM, and 2000 RPM was 5.1 μm, 1.2 μm, and 488 nm, respectively. UV-Vis spectrum of **Figure 18** also supports thinner thickness when the film coated with faster RPM. It described that higher transmittance could be achieved with increasing RPM speed because of thinner thickness. The changes in surface morphology with increasing thickness were also presented as described in FE-SEM surface images of **Figure 19(a)-(c)**. The more increasing the thickness of PANI/CSA film, the denser surface of film was obtained. This might lead to the decline in catalytic activity of the counter electrode because the catalytic

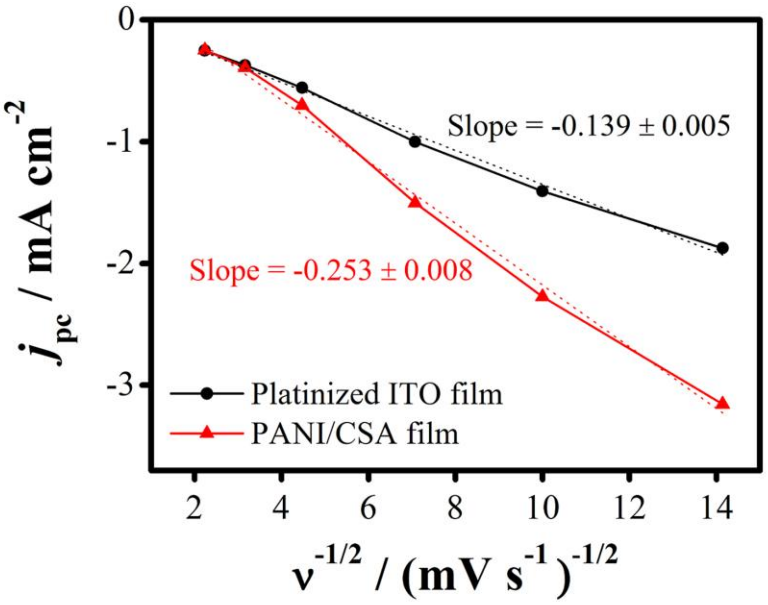

Figure 16. Comparison of redox performances of PANI/CSA counter electrode and the platinized TCO counter electrode under iodide redox electrolyte; relationship between (scan rate)$^{-1/2}$ ($\nu^{-1/2}$) and cathodic peak current density (j_{pc}).

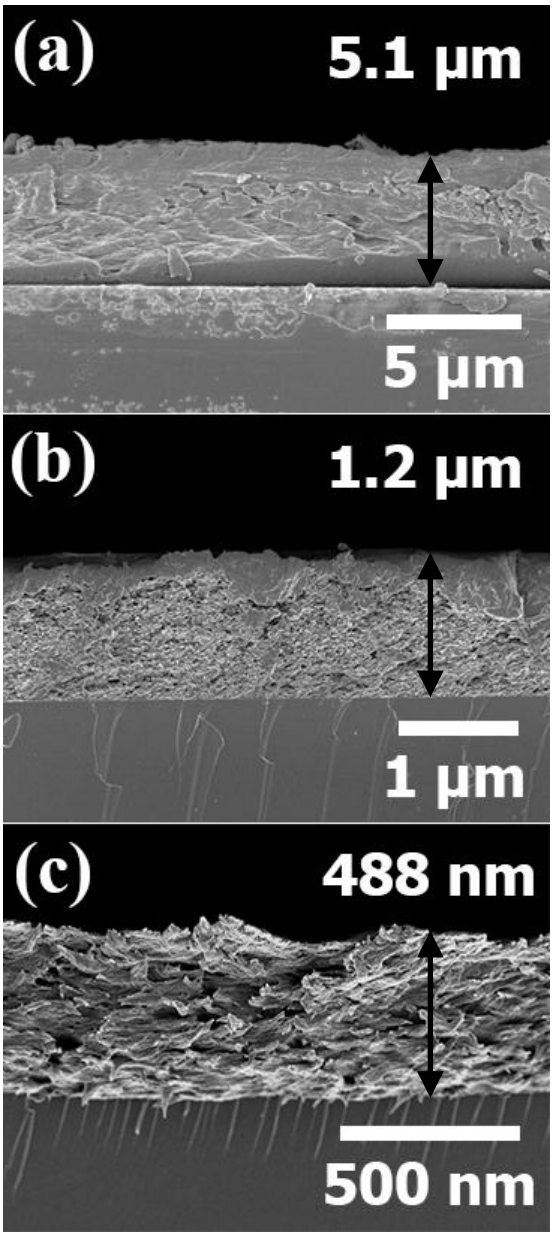

Figure 17. Cross-sectional FE-SEM images of PANI/CSA films spin-coated with different RPM speed; (a) 500, (b) 1000, and (c) 2000 RPM.

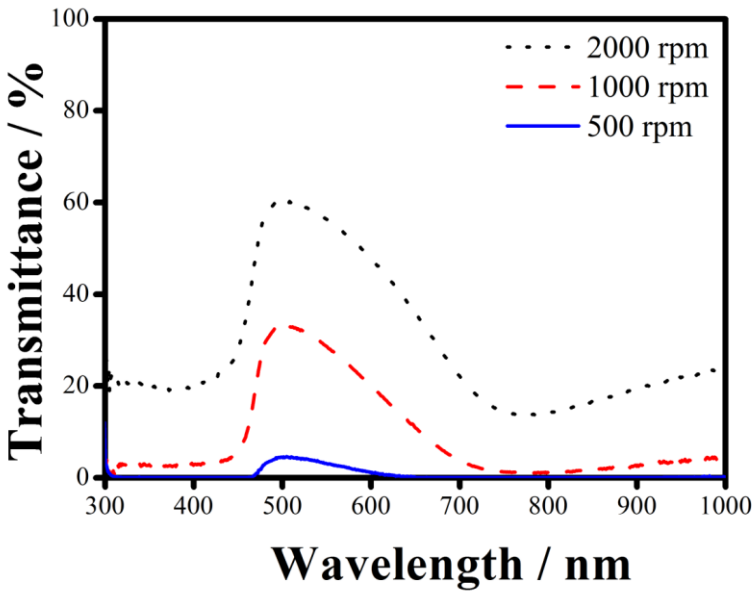

Figure 18. Comparison of the transmittance of the PANI/CSA film spin-coated with different RPM speed.

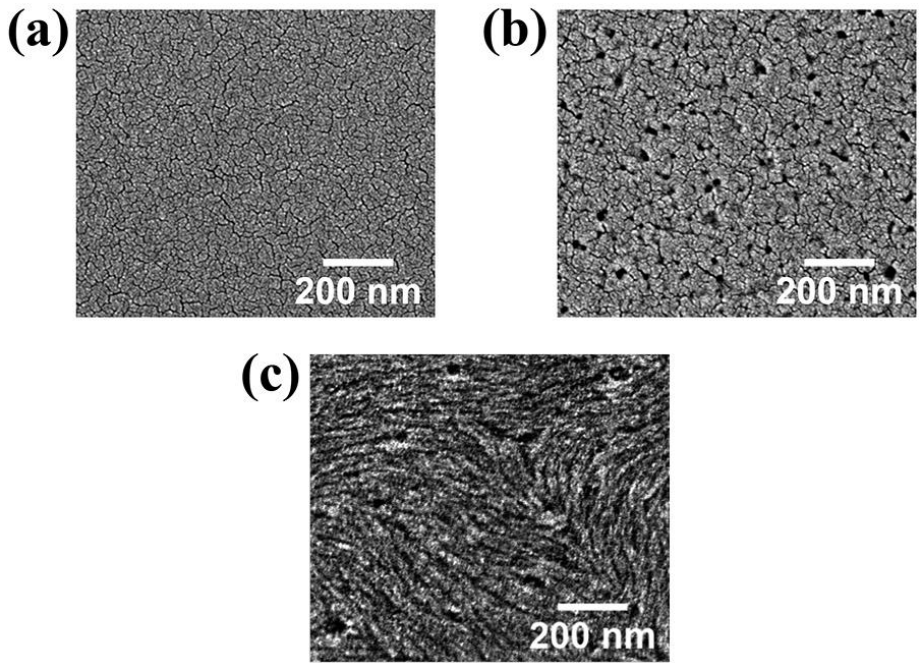

Figure 19. Surface FE-SEM images of the PANI/CSA film spin-coated with different RPM speed; (a) 500, (b) 1000, and (c) 2000 RPM.

activity generally depends on the surface area of the catalyst [194]. Therefore, this variation of thickness had a remarkable effect to performance of DSSCs. **Figure 20** shows the changes of performance with various thicknesses of PANI/CSA counter electrodes, and **Table 1** lists key parameters of these DSSCs. The conventional DSSC system which consisted of the photoanode, N719 dye-adsorbed 10 μm-thick anatase TiO_2 film on FTO substrate, and I^-/I_3^- redox couple was used at 1 sun front illumination condition. First of all, the short circuit current density of DSSCs was particularly changed from 10.5 mA cm^{-2} to 11.7 mA cm^{-2}. This increase of current density was also depicted in IPCE spectrums of **Figure 21**. It was attributed to changes of surface morphology as presented in FE-SEM images. The rough surface provided a large surface area to iodide redox couple in electrolyte [190], and it can lead to an elevation of the current density of DSSCs. In addition, mass transport limitations of the electrolyte were occurred in the thick film. As shown in current transient test (**Figure 22**), PANI/CSA film deposited by 500 RPM speed was presented this tendency due to thick thickness. The PANI/CSA counter electrodes exhibited higher substrate resistance and lower catalytic activity in EIS curves, **Figure 23**, compared to platinized ITO counter electrode (inset plot in **Figure 23**). The sheet resistance (R_s) was decreased with decreasing the RPM speed due to thicker thickness of PANI/CSA film. The higher charge transfer resistance (R_{ct}) at the counter electrode and electrolyte, high frequency in EIS [195,196], was observed with decreasing thickness. It was noted that the lower catalytic activity was exhibited at thinner

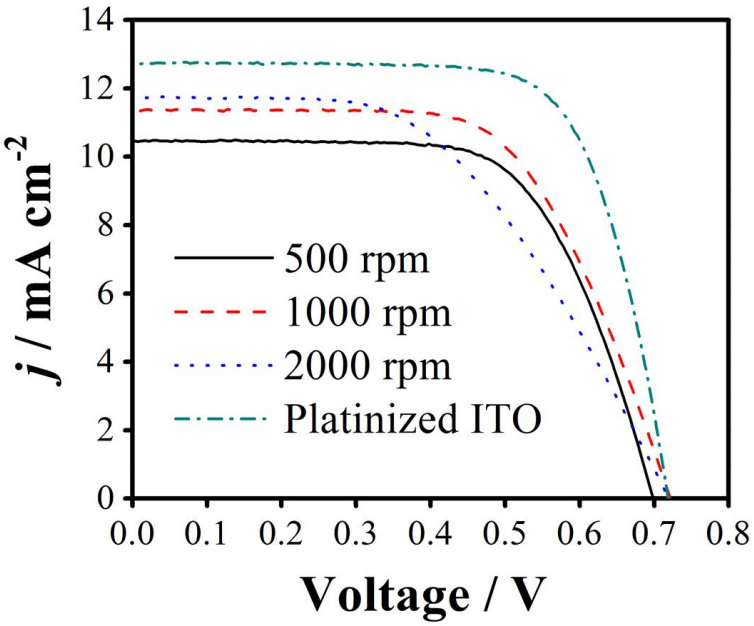

Figure 20. Comparison of the DSSC performance of the PANI/CSA counter electrode and the platinized TCO counter electrode under iodide redox electrolyte; current density–voltage (*j*-V) characteristics measurement of the DSSCs.

Table 1. Summary of the *j*–V characteristics of the DSSCs with various PANI/CSA counter electrodes differentiated by controlling RPM speed.

	Thickness (μm)	**V_{oc} (V)**	**j_{sc} (mA cm^{-2})**	**FF**	**η (%)**
500 RPM	5.1	0.70	10.50	0.66	4.82
1000 RPM	1.2	0.72	11.37	0.63	5.15
2000 RPM	0.49	0.72	11.72	0.51	4.32
Platinized ITO	-	0.72	12.72	0.71	6.56

* The dimension of the TiO_2 electrode was 0.22 cm^2.

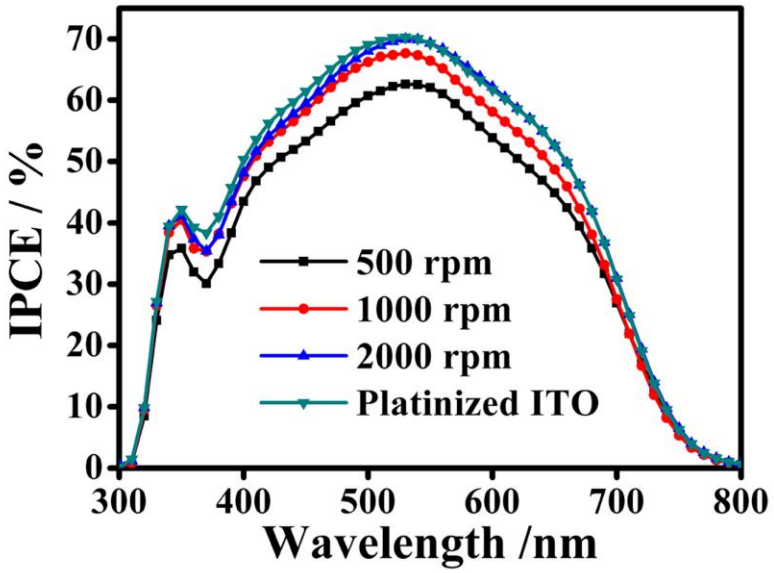

Figure 21. IPCE spectrum of DSSCs to compare the DSSC performance of the PANI/CSA counter electrode with different film thicknesses and the platinized TCO counter electrode under iodide redox electrolyte.

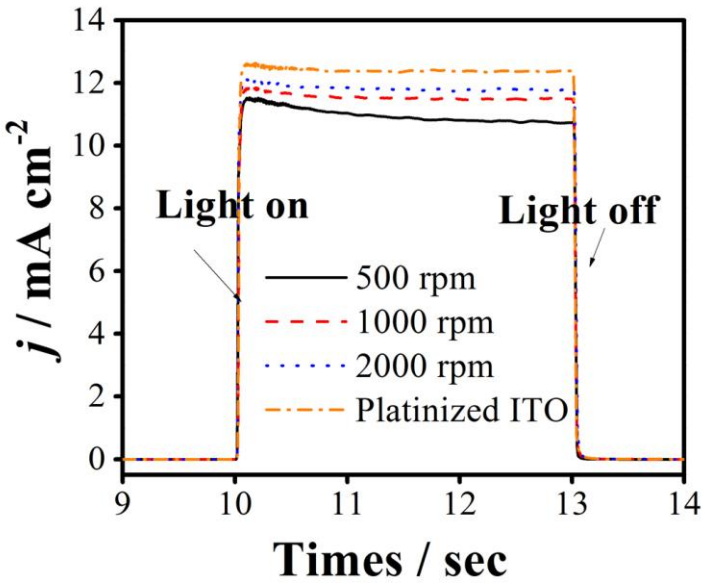

Figure 22. Comparison of the DSSC performance of the PANI/CSA counter electrode and the platinized TCO counter electrode under iodide redox electrolyte; plots of the short circuit current density versus time by current transient measurement.

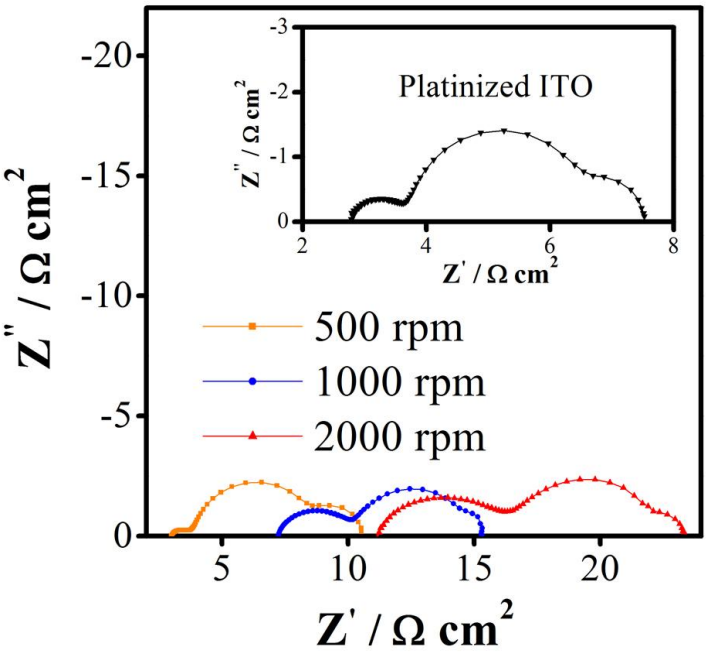

Figure 23. Comparison of the DSSC performance of the PANI/CSA counter electrode and the platinized TCO counter electrode under iodide redox electrolyte; Nyquist plots of the DSSCs from EIS curves.

thickness of PANI/CSA film. To optimize the performance of DSSCs, the rotation speed for spin-coating needs to be fixed to 1000 RPM in order to get best photovoltaic performance.

Thermal treatment temperature of the PANI/CSA film was varied to improve DSSC performance. Suitable temperature during the process was an essential to fabricate efficient conducting polymer film because it could affect the surface morphology and conductivity of the film. **Figure 24** displays the AFM surface images of PANI/CSA film heated at various temperatures from 50 to 200 ℃. With the exception of the film heated at 100 ℃, the root mean square (RMS) roughness of PANI/CSA film slightly raised from 3.43 to 3.89 nm with increasing thermal treatment temperature as presented in **Figure 24(a)-(d)**. It could be considered that the increment in roughness was attributed to solvent evaporation. *m*-cresol (b.p. 202.8 ℃) evaporated from the film during the heating step, resulting in the roughness increase of film. This rougher surface provides a larger surface area with potential chances to transfer electrons between the counter electrode and electrolyte [194]. However, this rough surface could also reduce carrier mobility along the polymer film, which might lead to the decrease of electrocatalytic activity. Indeed, Jung et al. have already reported that the very small change of surface roughness can strongly affect the charge transport property [197].

The thermal treatment temperature influenced the structure of PANI/CSA film as can be known from XRD patterns of **Figure 25**. The diffraction peak at 25° corresponding to the face-to-face inter-chain stacking distance between

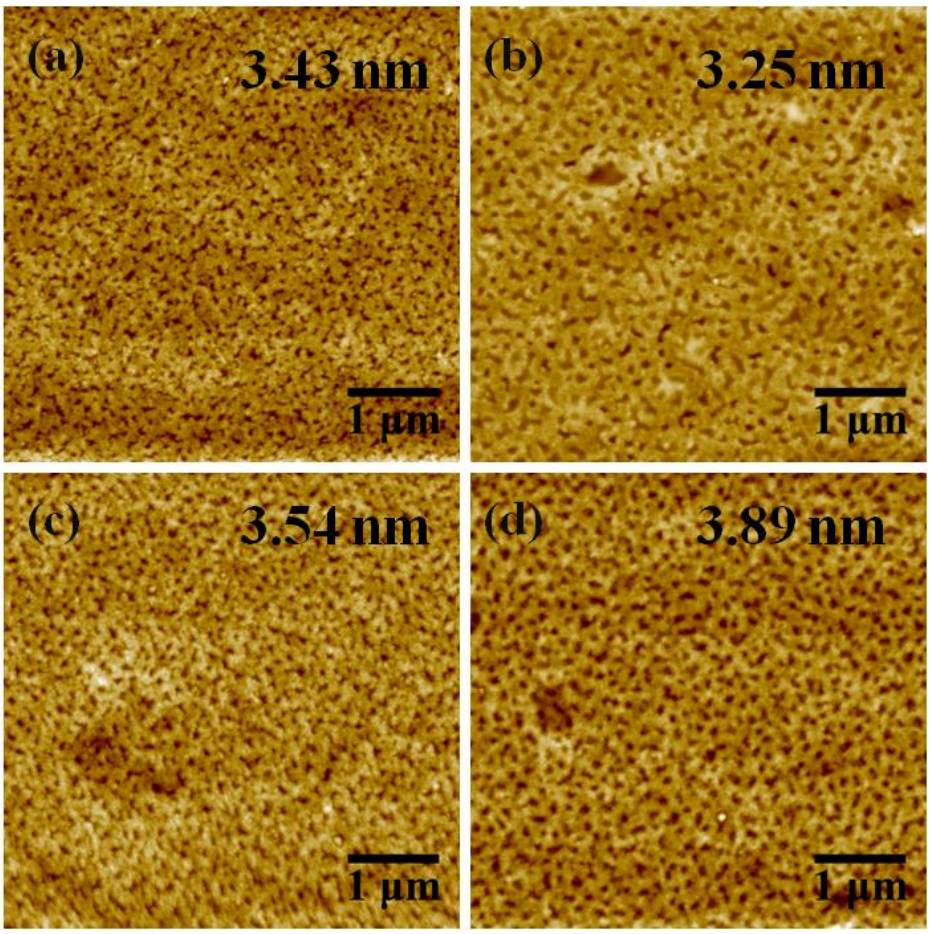

Figure 24. AFM images of the PANI/CSA film with different thermal treatment temperature; (a) 50, (b) 100, (c) 150, and (d) 200 ℃. RMS roughness values are also described on each figure.

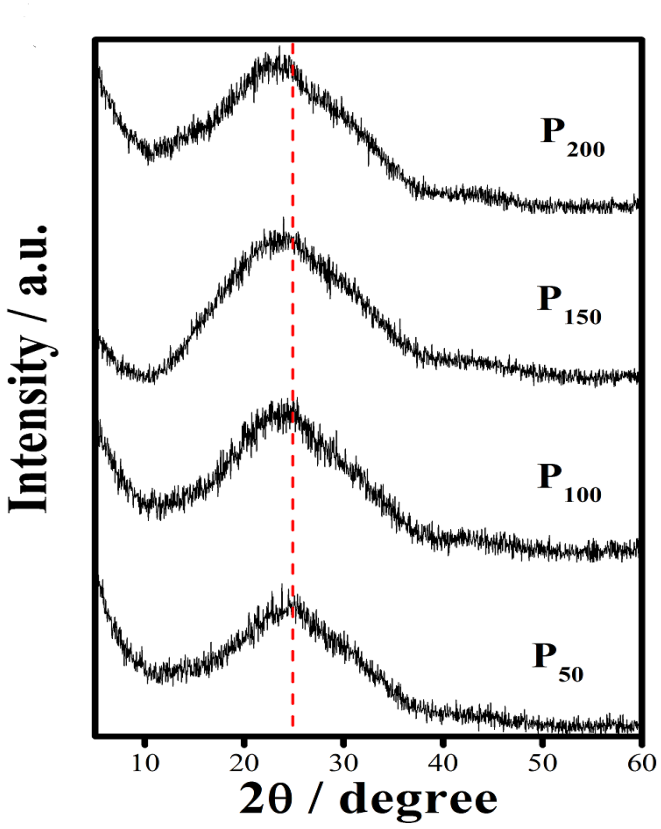

Figure 25. XRD patterns of the PANI/CSA films heated at 50 (P50), 100 (P100), 150 (P150), and 200 ℃ (P200).

phenyl rings presented a more planar chain conformation between the phenyl ring and the plane of the backbone, which resulting in conductivity in polymer materials [194,198]. However, the XRD patterns revealed noticeable changes in peak at 25° after the film heated over 150 ℃. It was considered that the heating over 150 ℃ was significantly affected to structure of the PANI/CSA, and this result meant that conducting polymer was damaged by high temperature heating process. It could be also supported by UV-Vis-NIR spectra in the range from visible and near-IR region (**Figure 26**). Free-carrier tail starting from ~1000 nm reduced as increasing the thermal treatment temperature compared to absorption peak at 440 nm [199]. A steadily increasing free-carrier tail relates to the extended coil conformation of the PANI [200]. Accordingly, weakening of free-carrier tail means transition of the PANI coil conformation, in turn, which leads to the decrease of charge transport ability associated with counter electrode performance. In particular, it seems like that the conformation of the PANI totally transforms to compact coil state at 200 ℃. Furthermore, the heat treatment temperature affected the CV curves for measuring electrocatalytic activity and electrochromic properties. **Figure 27** illustrates the comparison of the CV curves about the PANI/CSA film treated with different temperatures and **Figure 28** is the *in-situ* normalized transmittance curve at 633 nm wavelength (He-Ne laser) during continuous CV measurement. As presented in the CV curves in **Figure 27**, the PANI/CSA film heated at 100 ℃ shows the highest anodic and cathodic peak current compared to other films which were heated at 50, 150,

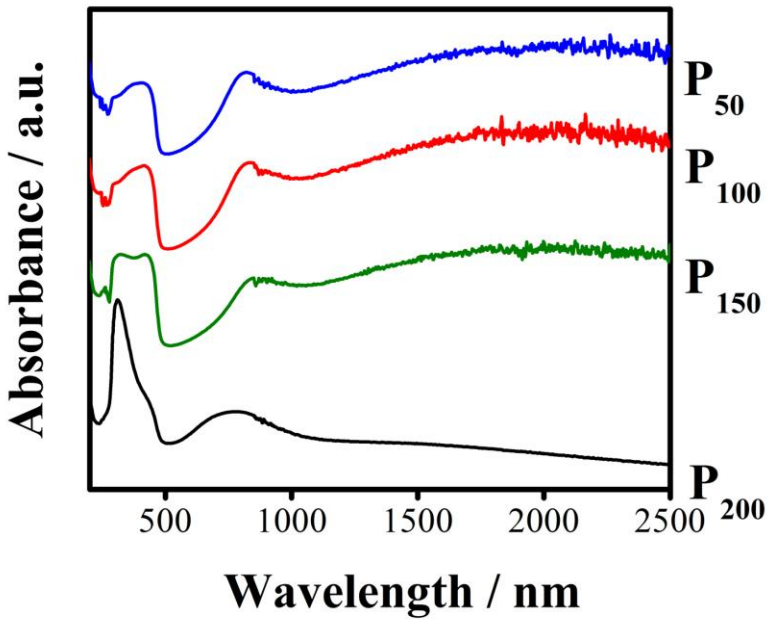

Figure 26. UV-Vis-NIR spectrum of the PANI/CSA film with different thermal treatment temperatures.

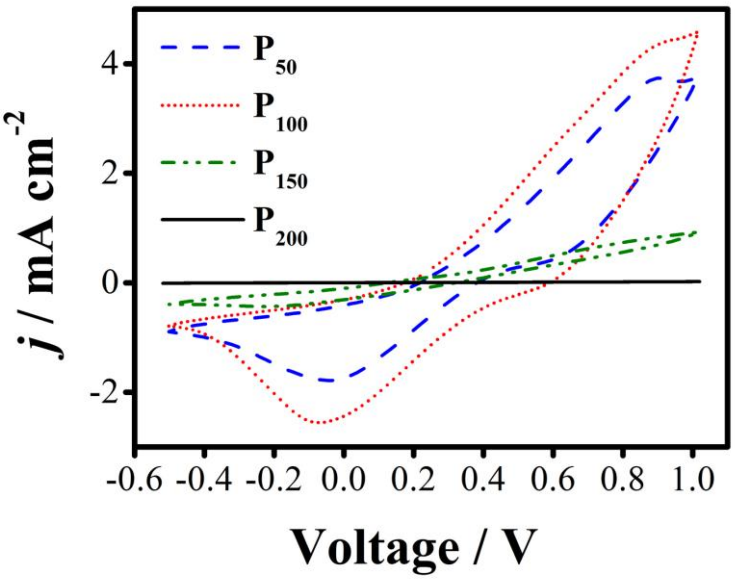

Figure 27. Electrochemical properties of PANI/CSA films with different thermal treatment temperatures; CV plots of PANI/CSA films.

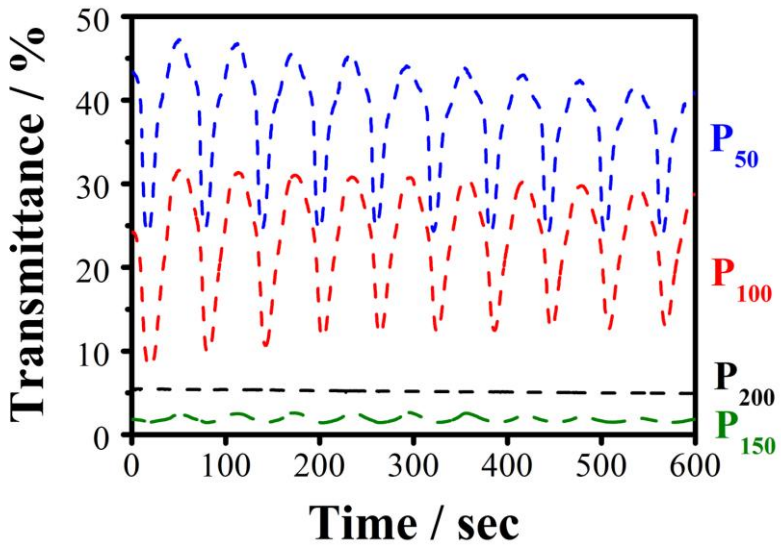

Figure 28. Optical transmittance changes of PANI/CSA films with different thermal treatment temperatures in *in-situ* optical transmittance during continuous potential cycling.

and 200 ℃. These results suggest that the higher redox current density describes the stronger electrocatalytic activity of PANI/CSA film toward the reduction of the iodide redox couple with thermal treatment at 100 ℃. On the other hands, electrochemical properties decreased significantly when the thermal treatment temperature was over 100 ℃. This phenomenon might be due to structural change of PANI which has three unique structures and colors depending upon the oxidation state; a fully reduced leucoemeraldine base, a fully oxidized pernigraniline base, and a half oxidized/half reduced emeraldine base (EB) state [188]. All of them are insulating materials, but EB can be conductive form, emeraldine salt (ES), by doping of various protonic acids. In addition, the ES state PANI can only be presented electrochromism which is convertible between ES and EB state by electrochemical reactions. The PANI/CSA counter electrodes heated at 50 and 100 ℃ reveal similar electrochromic properties which showed 22 % difference in optical transmittance change between colored/bleach states as indicated in **Figure 28**. However, PANI/CSA counter electrodes heated at 150 and 200 ℃ cannot show electrochromic properties. Therefore, it could be argued that the PANI/CSA under the condition below 150 ℃ has electrochemical property which can conduct reaction with electrolyte under DSSC system due to the structural deformation.

Figure 29 reveals the comparison of DSSC performances using the counter electrodes with platinized ITO glass and differently heated PANI/CSA films. **Table 2** lists performance parameters of DSSCs with these counter

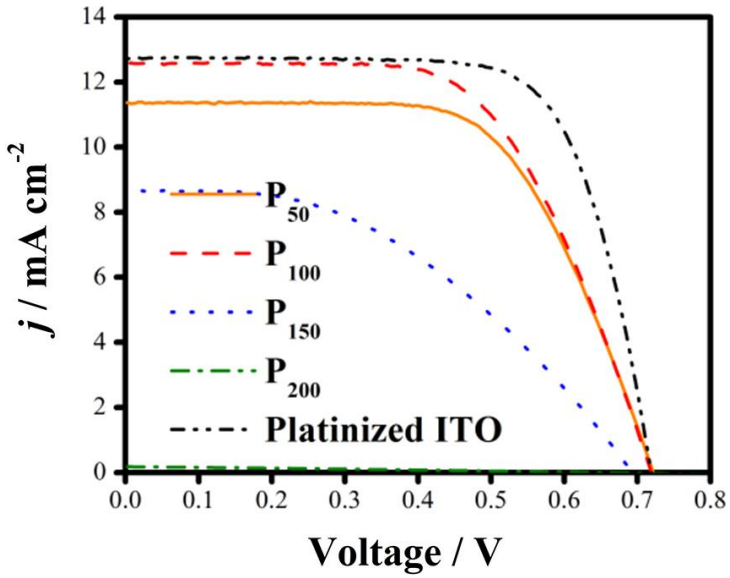

Figure 29. DSSC performances of PANI/CSA counter electrodes with different thermal treatment temperatures; current density–voltage characteristics of the DSSCs with iodide redox electrolyte.

Table 2. Summary of the *j*–V characteristics of the DSSCs with PANI/CSA counter electrodes differentiated by thermal treatment temperature.

	V_{oc} (V)	j_{sc} (mA cm^{-2})	FF	η (%)
P_{50}	0.72	11.37	0.63	5.15
P_{100}	0.72	12.58	0.61	5.50
P_{150}	0.69	8.67	0.44	2.65
P_{200}	0.65	0.18	0.28	0.03
Platinized ITO	0.72	12.72	0.71	6.56

* The dimension of the TiO_2 electrode was 0.22 cm^2.

electrodes. **Figure 29** shows the current density–voltage (*j*–*V*) curves under front illumination. First of all, the open-circuit voltage (V_{oc}) of the DSSCs decreased slightly with increasing thermal treatment temperature. This tendency might be due to the depredated electrochemical properties of PANI/CSA films during the heating process. On the other hand, the short circuit current (j_{sc}) was greatly affected by the thermal treatment temperatures. Comparing to the film heated at 50 ℃, the film heated at 100 ℃ gives higher short circuit current resulting from the improved conductivity during the heating process, which has lowest sheet resistance of 103 Ω/sq heated at 100 °C while the sheet resistance of the film heated at 50 °C was 117 Ω/sq. It was considered that more conductive film attributed easier electron transfer and the short circuit current density increased through heating process. However, when the PANI/CSA film was heated at 150 ℃, the sheet resistance of the film increased up to 192 Ω/sq and that of the film heated at 200 ℃ increased dramatically up to 725 kΩ/sq. The electrochemical properties of the films were also reduced as described in **Figure 27**. Thus, the short circuit currents of DSSCs with these overheated films decreased and the DSSC with the PANI/CSA counter electrode heated at 100 ℃ achieved the highest short circuit current. The Nyquist plot of EIS plotted in it was fitted using Z-view software [196]. In **Figure 30**, all kinds of resistance in DSSCs with PANI/CSA counter electrode were higher than that in DSSCs with platinized ITO counter electrode. Therefore, fill factor of DSSCs with PANI/CSA counter electrode was lower than that of DSSCs with platinized ITO counter

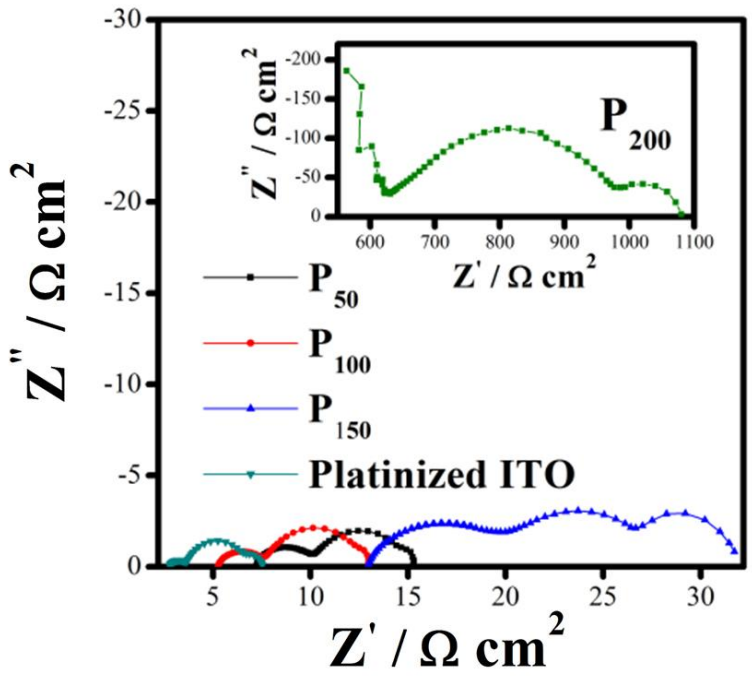

Figure 30. DSSC performances of PANI/CSA counter electrodes with different thermal treatment temperatures; Nyquist plots of DSSCs from EIS curves.

electrode. The diffusion resistance (W_s) values increased with increasing thermal treatment time. In addition, the lowest value of ohmic series resistance (R_s) and charge transfer resistance at counter electrode/electrolyte interface (R_{ct}) were observed in the film heated at 100 ℃. It is noteworthy that the PANI/CSA film heated at 100 ℃ could be the best functioned counter electrode for DSSCs. Therefore, thermal treatment at 100 ℃ is the optimized condition for efficient PANI/CSA counter electrode of DSSCs. This device exhibited comparable DSSC performance, j_{sc}, V_{oc}, fill factor and cell efficiency, compared to the reference cell, DSSC with the platinized ITO counter electrode which was displayed cell efficiency of 6.56 % as represented in **Figure 29**. The DSSC with PANI/CSA counter electrode presented 84 % of conversion efficiency compared to conventional counter electrode of DSSC. This result is remarkable because this DSSC device was not used expensive Pt and TCO materials on the counter electrode. The PANI/CSA film has transparency as shown in inset picture of **Figure 31**. It should be noted that the half-transparent PANI/CSA film could be applied to bifacial DSSC because transparency was crucial for high performance of the bifacial DSSC when the light was cast from the rear side [15]. As described in **Figure 31**, the UV-Vis spectrum of PANI/CSA and platinized ITO counter electrodes after electrolyte injection demonstrate different transmittance patterns. The PANI/CSA counter electrode had higher transmittance in the range above 470 nm while platinized ITO had higher transmittance in the range below 470 nm. Because maximum absorption value of dye is 510 nm, the PANI/CSA counter electrode which

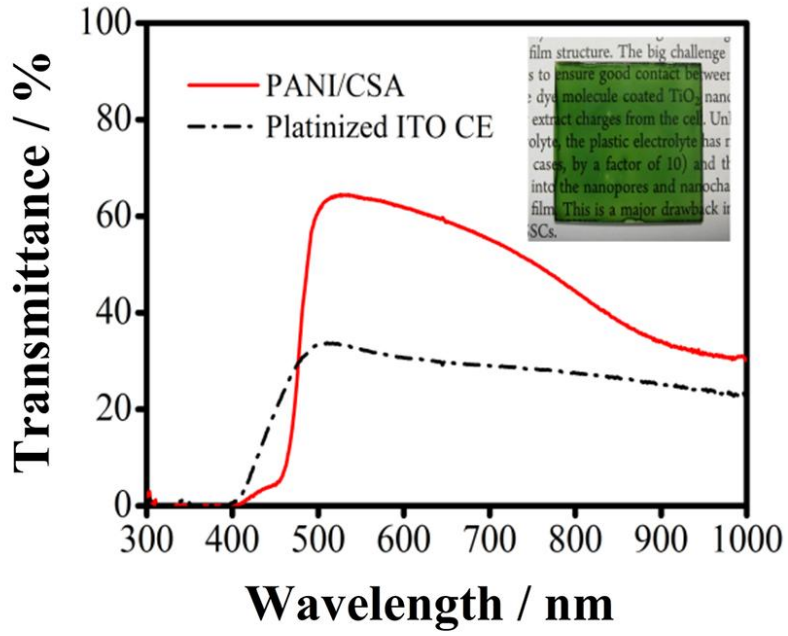

Figure 31. Comparison of DSSC performances of PANI/CSA counter electrode and the platinized TCO counter electrode from rear illumination; transmittance spectrum after electrolyte injection (inset picture is digital image of transparent PANI/CSA counter electrode).

showed higher transmittance in the range of 450 nm to 650 nm has benefit to light absorption from rear side illumination [186]. It was clearly indicated in IPCE spectrum of **Figure 32**. The DSSC with PANI/CSA counter electrode exhibited higher quantum efficiency from 500 nm to 700 nm. It was noted that the large amount of light could be absorbed on dye due to the complementary absorption properties of PANI film and dye [192]. In additions, the improved transparency of PANI/CSA film because of electrochromic properties which was illustrated in **Figure 18(b)** can help to increase light absorption from rear side illumination. Hence, the comparable j_{sc} was observed in DSSC with PANI/CSA counter electrode. The PANI/CSA film heated at 100 ℃, which exhibited the best performance in front illumination, was applied as the counter electrode of bifacial DSSC. As a result, the DSSC with the PANI/CSA film coated on TCO-free glass provided a j_{sc} of 5.44 mA cm^{-2} and cell efficiency of 2.67 % from rear illumination. It was considered that this comparable efficiency was originated from the effective absorption from rear illumination. (The DSSC with platinized ITO glass represented a j_{sc} of 5.46 mA cm^{-2} and cell efficiency of 2.86 % under rear illumination.)

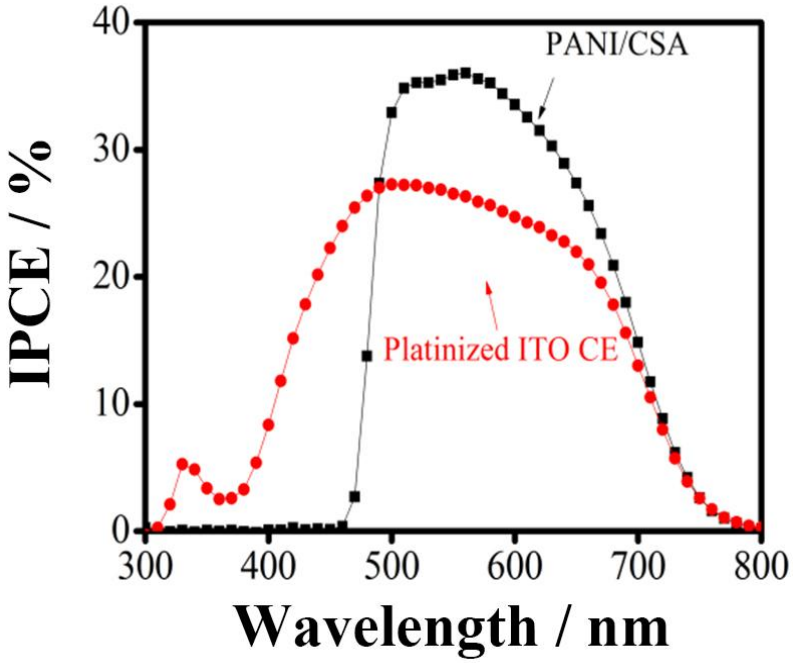

Figure 32. Comparison of DSSC performances of PANI/CSA counter electrode and the platinized TCO counter electrode from rear illumination; IPCE spectrum of the DSSCs.

3.2.2. PANI/CSA counter electrode for a novel organic dye-sensitized solar cell

Dye-sensitized solar cells (DSSCs) have received wide attention due to their high performance and low-cost of production. DSSCs based on Ru-complex photosensitizers such as N3, N719 and black dyes can provide efficient solar energy-to-electricity conversion efficiencies of up to 10% [201,202]. Compared to Ru-complexes, organic dyes have many advantages as photosensitizers, such as large molar extinction coefficient, control of absorption wavelength, facile design and synthesis, and lower cost than Ru complexes [203–205]. Efficient organic dyes such as perylene dyes, cyanine, xanthene, merocyanine, coumarin, hemicyanine and indoline dyes have been investigated as sensitizers [206–210]. In this part, the potential application of PANI/CSA counter electrode have been examined as a model system for the preparation of high-efficiency DSSCs based on a novel metal-free organic dye. For conventional DSSCs based on N719 (di-tetrabutylammonium-*cis*-*bis*(isothiocyanato)*bis*(2,2′-bipyridyl-4,4′-dicarboxylato) ruthenium(II)), the difference between the redox potential of the dye, $E(D/D^+)$ (1.0–1.1 V), and the I/I_3^- redox couple, $E(I^-/I_3^-)$, is in excess of 600 mV (**Figure 33**). (E^0 ranges from 0.35 V in acetonitrile [211] to typically 0.4 V for electrolytes optimized for ruthenium sensitizer-based DSSCs [212]) A novel metal-free organic dye (Carbz-PAHTDTT, S9) was used for this study. A detail synthetic route was demonstrated in **Figure 34**. S9 affords excellent light-harvesting properties when used in conjunction with thin TiO_2 electrodes comprising a 2.2 μm

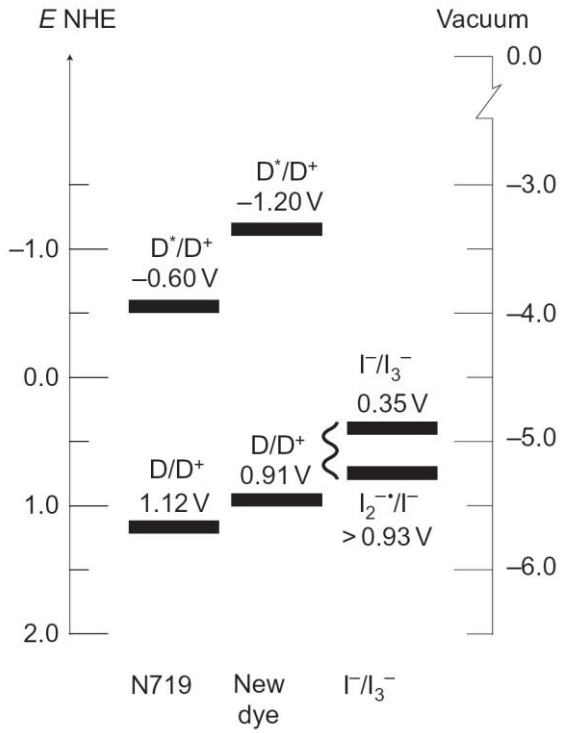

Figure 33. Energy levels of DSSC components, approximate redox potentials and band energies of the different components. Data for N719, Carbz-PAHTDTT (new dye), and I^-/I_3^- versus normal hydrogen electrode (NHE) [211,213,214].

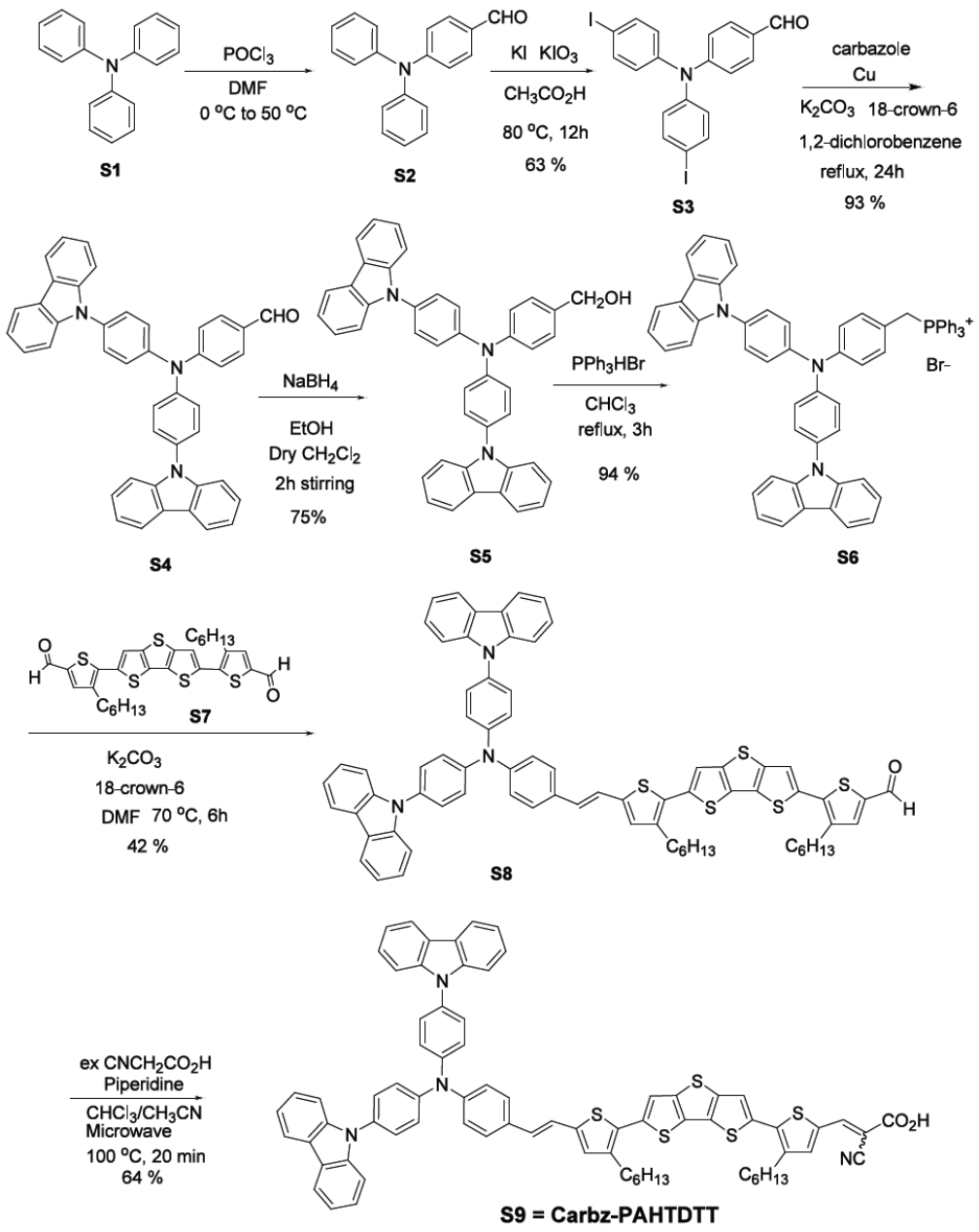

Figure 34. Synthesis of Carbz-PAHTDTT (S9). Reproduced with permission.

mesoporous TiO_2 layer (particle size, 18 nm) and a 4.4 μm TiO_2 scattering layer (particle size, 400 nm). The combination of thin TiO_2 electrodes and organic dyes with high extinction coefficients has previously been proven to be beneficial for solid-state DSSCs based on organic charge transport materials, where accelerated charge recombination is of equal concern [215].

Adsorption of S9 onto TiO_2 was routinely performed in the presence of chenodeoxycholic acid (cheno) (**Figure 35**) as co-adsorbent, as this consistently led to improved DSSC performances for all the electrolyte systems studied. This is in agreement with previous studies applying metal-free organic dyes, and is typically explained in terms of a reduction in dye aggregation and improved surface passivation [216].

The IPCE spectra of S9-sensitized solar cells with optimized I^-/I_3^- electrolyte compositions are shown in **Figure 36**. These spectra provide the conversion efficiency quantification of absorbed photons into current. The addition of cheno had no effect on the IPCE of the I^-/I_3^- devices (DSSC-C not shown). The absorptivity exceeding 80% at wavelengths up to 600 nm illustrates the excellent light-harvesting properties of the S9-sensitized TiO_2 films. The current/voltage characteristics under simulated one sun solar illumination (AM1.5; 1,000 W m^{-2}) of DSSCs are presented in **Figure 37** and **Table 4**. There are two types of counter electrodes for organic DSSCs using PANI/CSA; PANI/CSA coated on FTO substrate and normal glass substrate. PANI/CSA coating method on the substrates and cell assembly process are same with previous part **3.2.1.** Remarkable conversion efficiency was observed

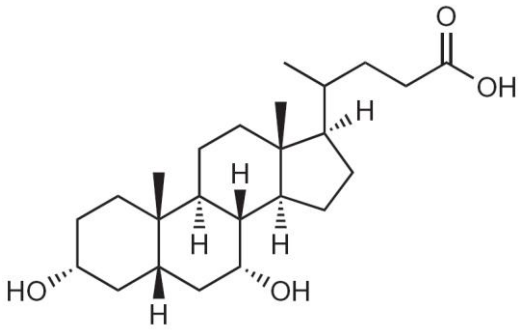

Figure 35. Structure of the co-adsorbent and electrolyte additive chenodeoxycholic acid (cheno). Reproduced with permission. Copyright 2011 Right Managed by Nature Publishing Group.

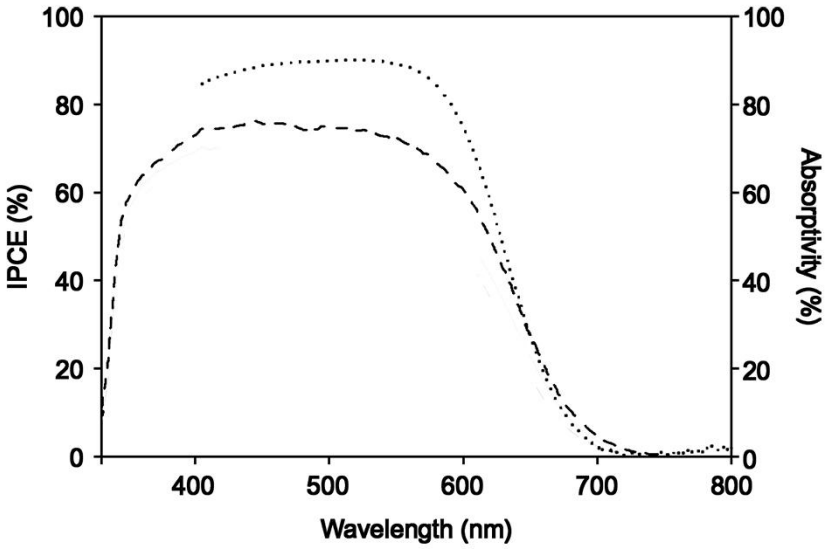

Figure 36. IPCE results and absorptivity of the S9-sensitized TiO_2 film. Black dotted line indicates the absorptivity of the sensitized TiO_2 film. IPCE spectra are recorded at low light conditions (<2% sun). Electrolyte composition is summarized in **Table 3**. Double layer TiO_2 films (2.2 μm mesoporous TiO_2 (18 nm) + 4.4 μm scattering TiO_2 (400 nm)) were used for constructing all DSSCs.

Table 3. Electrolyte compositions used throughout the study.

	ox:red ratio	I_2 (M)	PMII (M)	t-BP (M)	Cheno (M)	GuSCN (M)	Solvent
DSSC	1:5	0.05	0.6	0.5		0.1	ACN:VN 85:15
DSSC-C	1:5	0.05	0.6	0.5	0.01	0.1	ACN:VN 85:15

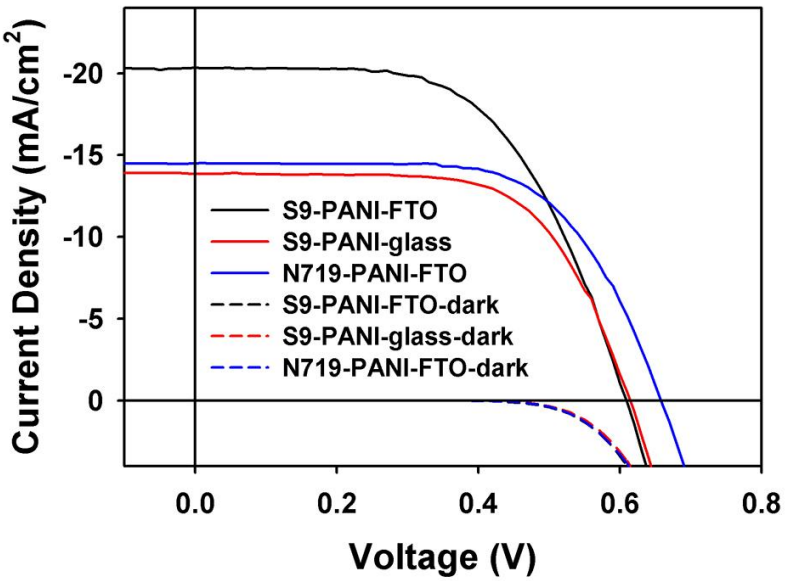

Figure 37. Photocurrent density–voltage curves at simulated one sun (1,000 Wm^{-2}) irradiation (AM1.5).

Table 4. Tabulated photovoltaic performance data of the DSSC in **Figure 37**, measured at one sun simulated sunlight (AM1.5).

	V_{oc} (V)	j_{sc} (mA cm^{-2})	FF	η (%)
S9-PANI-FTO	0.61	− 20.36	0.58	7.16
S9-PANI-Glass	0.61	− 13.86	0.65	5.51
N719-PANI-FTO	0.66	− 14.49	0.61	6.13

* The dimension of the TiO_2 electrode was 0.16 cm^2.

when using S9-sensitized solar cell with FTO substrate up to 7.16 % compared to Ru-based solar cell. Main reason for this enhancement is thought that the j_{sc} of the cell is largely increased due to higher molar extinction coefficient of S9 than that of N719 [217] in the range of visible light as depicted in **Figure 38**. In addition, the cheno used as co-adsorbent of S9 dye significantly increases the electron lifetime for both redox systems, presumably by blocking interfacial charge recombination. In the case of using glass substrate in counter electrode for the metal-free solar cells, conversion efficiency has decreased to 5.51% as compared with FTO substrate, showing vary comparable performance with previous part **3.2.1.** It is noteworthy that S9-sensitized solar cells present relatively low V_{oc} values due to the carrier trapping in the organic dye. It has been shown that charge carrier trapping and detrapping are responsible for current instabilities and bias stress effect in OTFTs and OLEDs and reduction of open circuit voltage in OSCs [218–221]. In spite of this structural defect, the large increase in j_{sc} compensated the decrease in V_{oc}, which lead to overall increase of cell performance.

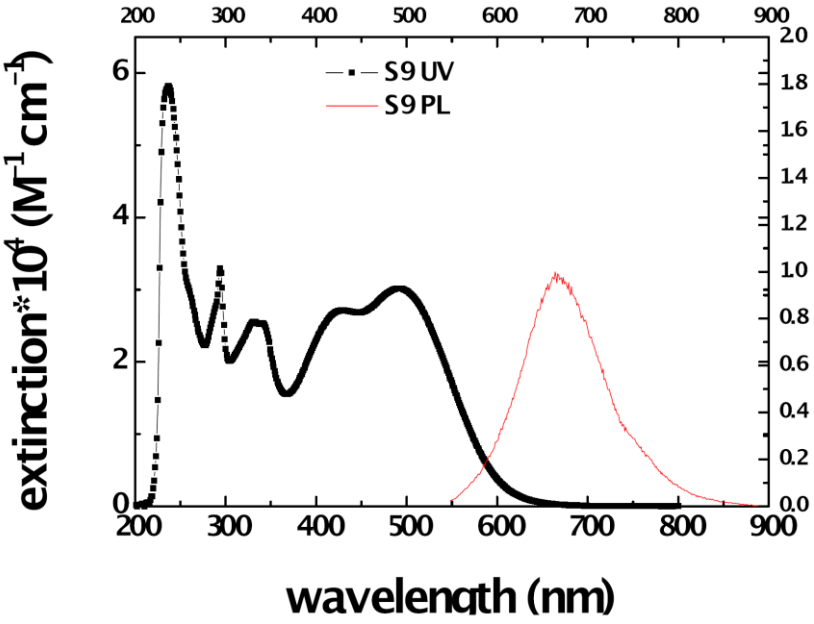

Figure 38. UV-Vis and photoluminescence spectra for S9, measured as a 0.02 mM solution in CH_2Cl_2. Reproduced with permission. Copyright 2011 Right Managed by Nature Publishing Group.

Table 5. Summary of electrochemical and photophysical data for S9 (Carbz-PAHTDTT). Reproduced with permission. Copyright 2011 Right Managed by Nature Publishing Group.

	Abs ($\varepsilon \times 10^4$ $cm^{-1}mol^{-1}$)[a]	PL (λ_{max})[a]	E_{ox} (V) vs (NHE)[b]	$E_{0\text{-}0}$ (V) vs (Abs/Em)[c]	E_{ox}-$E_{0\text{-}0}$ (V) vs (NHE)
S9	235 (1.7), 294 (3.3), 330 (2.5), 426 (2.7), 491 (3.0)	664	0.91	2.11	− 1.20

[a]0.02 mM CH_2Cl_2 solution at 298 K. [b]Cyclic voltammogram of the onset point of the dyes were measured in dry CH_2Cl_2 containing 0.1 M $TBAPF_6$ (tetrabutylammonium hexafluorophosphate) as supporting electrolyte, Ag/AgCl as a reference electrode, and glassy carbon as working electrode. [c]The $E_{0\text{-}0}$ transition energy was estimated from the intersection of the absorption and emission spectra, using the following equation *x* $V = 10^7/(\lambda_{intersection}\ nm \times 8065.48\ cm^{-1})$

3.3. Organic Electrodes for Organic Thin Film Transistor

3.3.1. Polypyrrole source/drain electrode by using inkjet printing-mediated vapor deposition polymerization for organic thin film transistor

The development of a printing process for the fabrication of organic thin-film transistors (OTFTs) has focused on printed flexible electronics. Among established printing methods, including inkjet printing (IJP) [139], spray printing [222], screen printing [223], and μ-contact printing [224], IJP has received attention because it is a direct, simple process that can print over a large area, does not leave residual ink due to drop-on-demand patterning, and is widely compatible with various materials without the need for a pre-patterned mold or mask. Recently, a customized high-resolution inkjet printer designed specifically for laboratory and industrial use was developed and distributed. However, conventional desktop inkjet printer enables low-cost fabrication of printed patterns using word-processing software.

Conducting polymers are promising materials as printable electrodes for flexible electronic devices due to their high conductivity and environmental stability [225]. However, most conductive polymers cannot be dispersed in common solvents; thus, little attention has been paid to these conducting materials and their application as S/D electrodes for printed electronics. Few studies have reported the use of patterned conducting polymers in OTFTs for printing S/D electrodes using different methods and structures. PEDOT:PSS *via* IJP acted as functional S/D electrodes with a bottom-gate, bottom-contact structure [226]. Wang et al. studied inkjet-printed S/D PEDOT:PSS with top-

gate geometry in polymer TFTs [227]. Patterning electrodes based on polyaniline-poly(2-acrylamido-2-methyl-1-propane-sulfonic acid) (PANI-PAAMPSA) were printed on a silane-treated substrate by μ-contact printing in bottom-contact transistors [228]. Stamping technique with PEDOT S/D electrodes for bottom-contact OTFTs was reported by D. Li et al. [229] These reports, all of which used water-dispersive conducting polymers as electrodes for printed patterns, showed relatively low device performance compared with Au S/D electrode devices or good performance with different printing methods. The integration of nondispersive conducting polymer materials into top-contact OTFTs by inkjet printing technique has been a challenge in flexible electronics.

Vapor deposition polymerization (VDP) has been suggested as a method for thin-film electrode of conducting polymers. In VDP, vaporized monomers absorb only on an initiator and subsequently facilitate the polymerization of pyrrole. VDP, introduced in our previous report [230], was used to modify inorganic nanomaterials with polymer, resulting in a new type of nanomaterial with an inorganic-polymer core–shell structure.

In this part, a versatile route to overcome the limitations of printing nondispersive conducting polymer PPy was introduced by combining inkjet printing with vapor deposition polymerization (IJP-VDP) for the fabrication of top-contact S/D electrodes in flexible OTFTs. PPy was chosen because it could be substituted for expensive Au electrodes and opened a way to pattern of nondispersive conducting polymer in common solvents. An initiator solution

was deposited on the organic semiconductor layer by IJP, and subsequent exposure to vaporized monomers induced selective polymerization, producing a conducting polymer on the printed initiator. IJP-VDP is emerging as a useful method for printing an electrode pattern of nondispersive conducting polymers in top-contact OTFTs instead of metal electrodes. To the best of our knowledge, this is the first report of high-performance flexible pentacene transistors with top-contact S/D electrodes of a patterned conducting polymer using IJP-VDP, where illustrate the simplicity and versatility of the patterning process with a nondispersive conducting polymer.

Figure 39 shows IJP-VDP patterning applied to the fabrication of S/D electrodes in an OTFT, exhibiting a well-defined PPy pattern with a channel length of ~135 μm and thickness of ~450 nm. To confirm the polymerization of pyrrole monomers, Fourier transform infrared-attenuated total reflection (FTIR-ATR) analysis was used. Peaks at 1549, 1410, and 723 cm^{-1} were attributed to ring stretching, conjugated C–N stretching, and C–H wagging vibrations, respectively, and were in good agreement with FTIR spectra of PPy in our previous work [148]. The OTFT device with a bottom-gate, top-contact structure was built on a PES plastic film. A control device using evaporated Au was also fabricated as the top-contact S/D electrodes instead of printed PPy.

In IJP, the patterning resolution, or minimum feature accuracy, is affected by several factors, including properties of the substrate, ink viscosity, and printing method [231]. A stabilizer or surfactant, formulated with the proper viscosity and surface energy, is added to the conductive dispersive solution

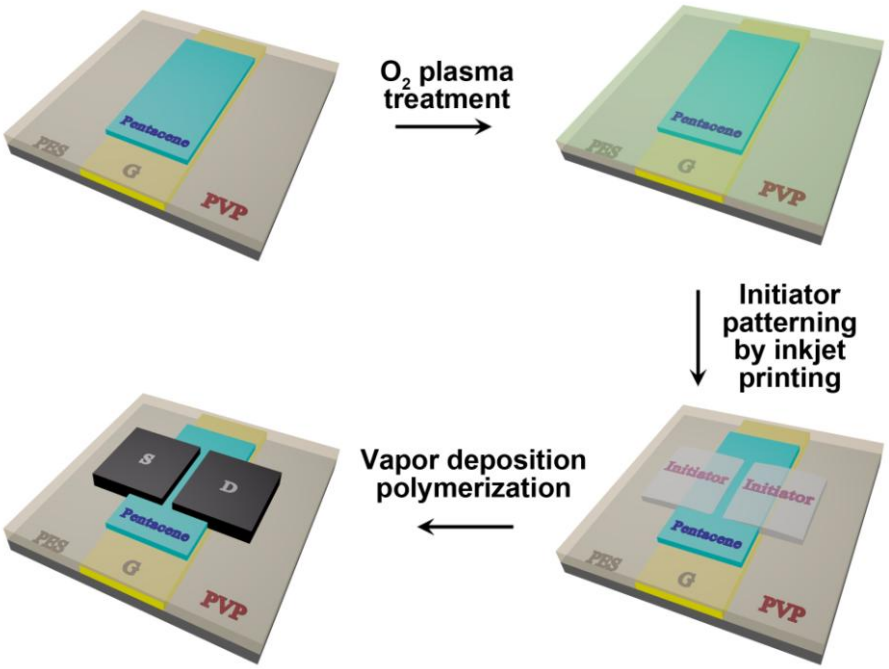

Figure 39. The schematic illustration of bottom-gate and top-contact OTFTs configuration via IJP-VDP method.

to modify ink properties for IJP applications [232]. This modification was applied to the initiator solution for IJP patterning of a nondispersive conducting polymer by using additives.

The edge waviness of printed PPy electrodes is shown in **Figure 40**. This phenomenon is often observed for IJP of conducting polymer patterns, inducing a large current variation compared with conventional evaporated metal electrodes with a shadow mask [233]. Thus, control of edge waviness is an important issue in the design of printed OTFTs. In this study, distinctive channel lengths were obtained according to the amount of PSS added to the initiator solution by IJP. The variation in PSS concentration (0 to 12 wt%) correlated to the edge resolution and the surface resistance of the PPy electrode pattern, as shown in **Figure 41**. The protrusion edge decreased until PSS reached 6 wt% and then increased from 6 to 12 wt% PSS. After 6 wt% PSS, clogging in the printer nozzle started, resulting in the collapse of the edge resolution in the printed pattern. Since PSS chains typically consist of a few hundred monomer units, even rather small differences in surface energy between the components in the initiator solution are sufficient to lead to almost complete surface pattern coverage by the lowest energy component of long chain length in PSS polymer, leading to reduce the edge protrusion of the pattern. Moreover, the surface resistance increased as the amount of polymeric PSS in the initiator solution increased. The surface resistance of the PPy electrode pattern without PSS was measured at ~2.75×10^3 Ω/sq by the four-probe method and increased to ~8.61×10^4 Ω/sq with 12 wt% PSS in APS

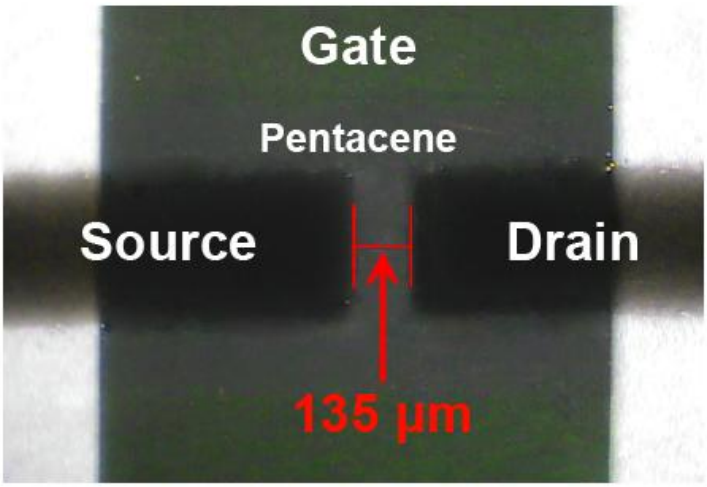

Figure 40. Optical image of patterned source and drain electrodes with PPy.

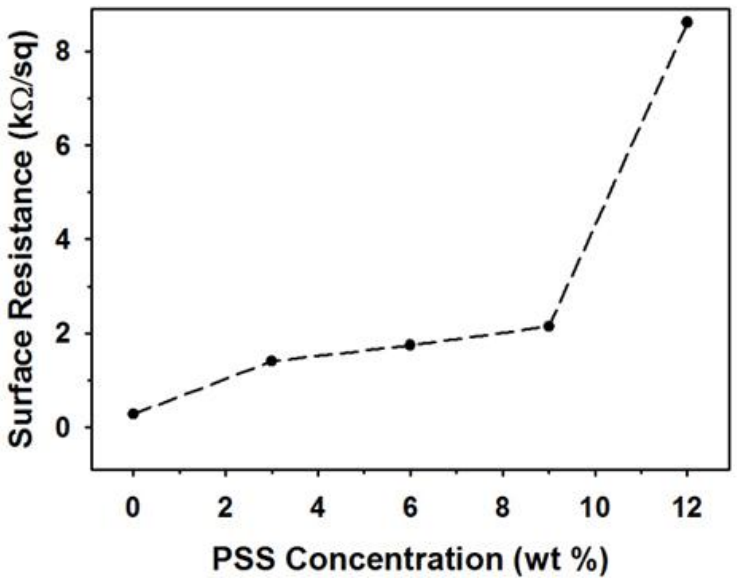

Figure 41. Surface resistances of PPy electrodes with different PSS concentrations.

solution. Arribas et al. demonstrated the synthesis of conductive PPy prepared by ferric chloride as an oxidant with PSS as a counterion [234]. According to their results, monomer/PSS ratio had little influence on the conductivity of PPy due to their insulating nature, while the increase of the conductivity was attributed to the monomer/oxidant concentration. In this work, the sheet resistance is rather stable against changes until 9 wt% of PSS concentration. The insulating function of PSS was found to result in an abrupt increase in sheet resistance at 12 wt% of PSS due to the hindrance of electrical percolation. With respect to both the edge resolution and the sheet resistance, the surface resistance was optimized at 1.74×10^4 Ω/sq and 6 wt% PSS, which was sufficient for application in organic electronic devices as an organic electrode [229,235,236]. Thus, conductive PPy patterns were achieved by modifying the initiator properties and using the proposed patterning process. Additionally, the vaporized pyrrole monomer was homogeneously deposited and polymerized directly on the printed oxidant pattern. The highly conductive polymer patterns were attributed to the continuous growth of a polymer film with no disconnections or cracks.

In order to check the electrical potential of the top-contact PPy electrodes fabricated by the proposed IJP-VDP method, thermally evaporated Au S/D electrodes were used in pentacene TFTs for comparison. **Figure 42** shows typical electrical output and transfer characteristics of a pentacene TFT with S/D electrodes of (a) PPy (PPy-OTFT) and (b) Au (Au-OTFT). Under our experimental conditions, a field-effect mobility of 0.18 ± 0.03 $cm^2 V^{-1} s^{-1}$, a

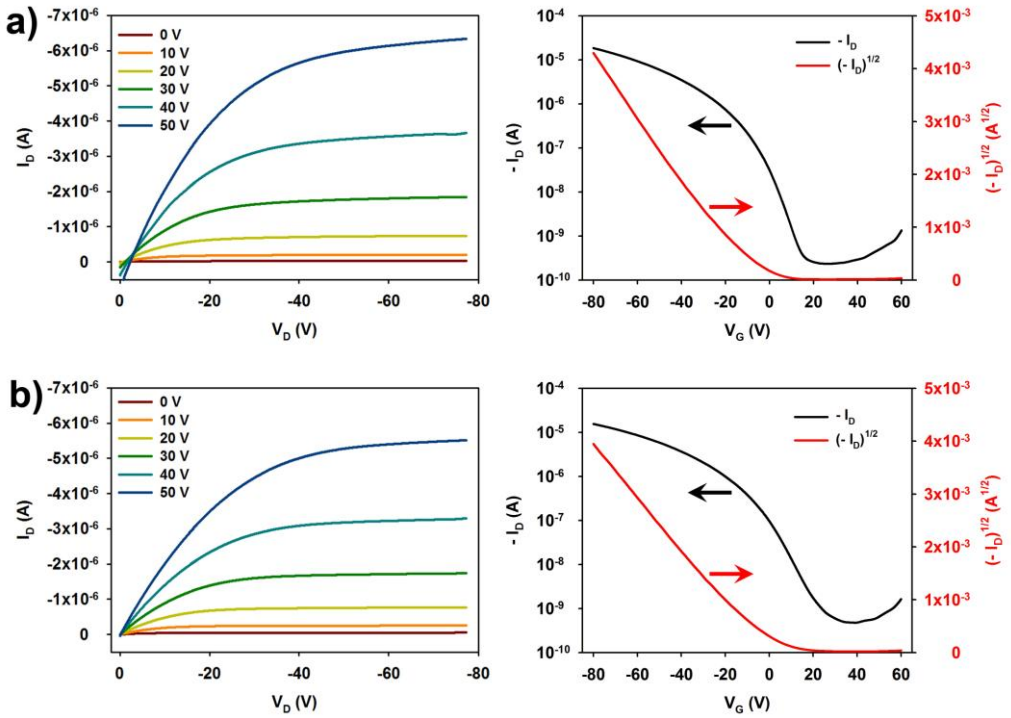

Figure 42. Electrical output and transfer characteristics of the pentacene TFTs with source and drain electrodes of (a) PPy and (b) Au.

threshold voltage of −1.99 V, and an on/off current ratio of 3.23×10^4 were obtained in the PPy-OTFT (**Figure 42(a)**). These results are comparable to the characteristics of the Au-OTFT with a field-effect mobility of 0.15 ± 0.02 $cm^2 V^{-1} s^{-1}$, a threshold voltage of −10.09 V, and an on/off current ratio of 8.05×10^4 (**Figure 42(b)**). In particular, the higher mobility of the PPy-OTFT was obtained at the same voltage applied to the Au-TFT. The leakage current was less than a few nanoamperes in both cases, which is typical for OTFTs.

It is known that the R_c between the electrode and the organic channel is primarily caused by the charge-injection barrier formed at the interface that strongly dominates the charge injection properties. Hill et al.[237] previously reported that the electronic structure of most metal-organic molecular semiconductor interface has the simple Schottky-Mott limit and exhibits a substantial interfacial dipole barrier, where a significant fraction of the interface dipole barriers at the interfaces corresponds to a lower metal work function due to adjacent organic molecules. In the case of a polymer-polymer interface, a conducting polymer has fewer free electrons than a metal. Its work function does not have a significant surface electron tail contribution and does not change, unlike the modification on a metal–polymer surface. This, in turn, makes it possible to form smaller hole-injection barriers at the interface between the polymer electrode and organic semiconductor compared with the Au electrode/pentacene contact even though both metal and polymer electrodes have similar work function [238].

The R_C of PPy and Au electrodes was investigated using the transfer-line

method (TLM). When the on resistances (R_{on}) for low V_{DS} = −2 V were normalized, linear ohmic contacts were observed with increasing channel length. As shown in **Figure 43**, the R_c decreased with V_G becoming more negative for both Au-OTFTs and PPy-OTFTs. Such a decrease in R_c with more negative V_G is correlated to the higher density of charge in the conducting channel in the large channel-length regime [239]. For the Au-TFT patterns from TLM, the corresponding channel resistance was measured at a gate voltage of −30 V, providing a slope (R_s/W) of 4.1×10^5 Ω/sq, similar to that of the PPy-TFT shapes from TLM. Especially, the R_c of the printed PPy electrodes was approximately one order of magnitude lower than that of the Au electrodes. These results suggest that the channel resistance of both TFTs was similar regardless of contact; thus, reduced contact resistance was a primary reason for the increased mobility.

The slight decrease in the on/off current ratio and slight increase in the subthreshold slope of the printed PPy-TFTs are thought to be related to the formation of pentacenequinone during surface treatment of pentacene by IJP (**Figure 42**). In the fabrication process, O_2 plasma treatment was used to increase the surface energy of the pentacene semiconductor surface layer for printing the initiator solution to form a uniform PPy electrode. However, O_2 plasma plays an important role in obtaining successful initiator patterns on the pentacene surface and also limiting device performance. The conjugated carbons of pentacene were functionalized to C–O or C=O groups by O_2 plasma treatment [240], resulting in the formation of charge-scattering sites in

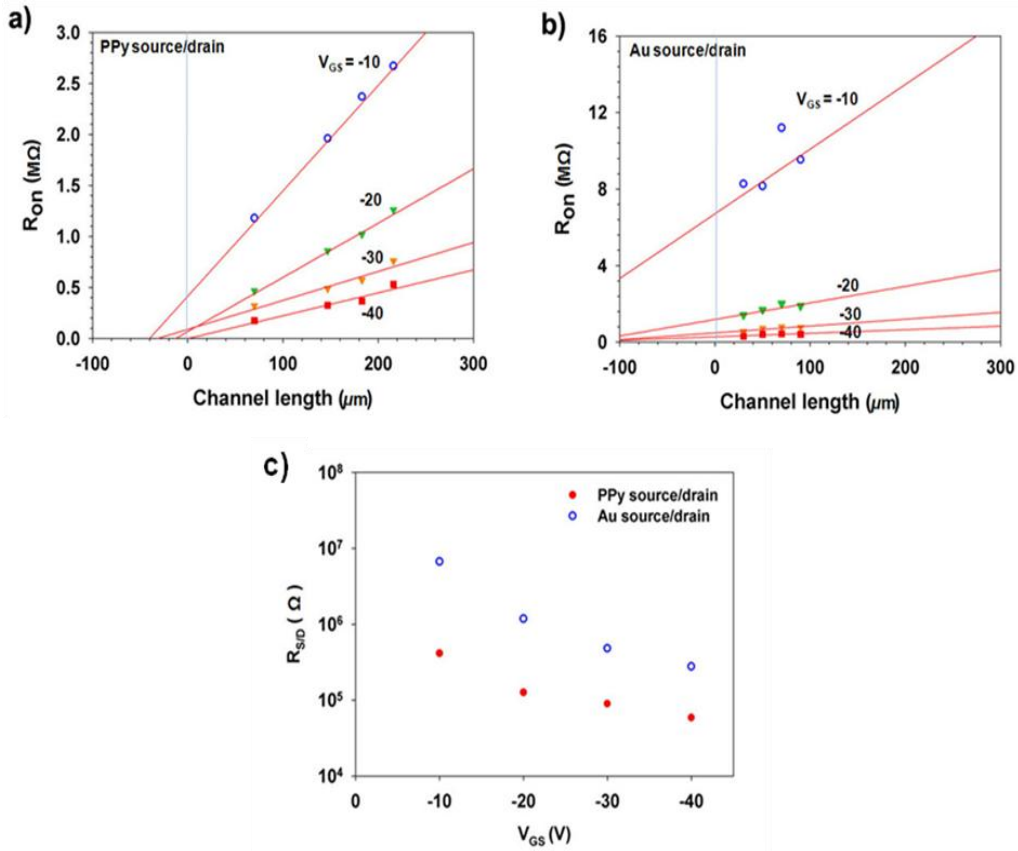

Figure 43. Channel width-normalized contact resistance in devices with source/drain electrodes of (a) PPy and (b) Au. (c) Total contact resistance ($R_{S/D}$) of both PPy and Au OTFTs as a function of applied gate voltage.

the molecules. To minimize pentacene damage for carrier transport and maximize device performance, O_2 plasma treatment was conducted at 80 W for 1 s. Subsequently, PPy S/D electrodes were baked for 10 min at 100℃ after IJP-VDP to remove residual moisture and increase electrical performance.

3.3.2. Graphene gate electrode by using pressure-assisted thermal reduction method for organic thin film transistor

Graphene-based conductive films have been studied as transparent electrodes for potential applications as field effect transistors [241], sensors [242] and organic photovoltaic devices [243]. Up to date, graphene can be produced by various synthetic routes including micromechanical exfoliation of graphite [244], chemical vapor deposition [245], epitaxial growth [246], and chemical exfoliation from bulk graphite. Solution-based synthesis of chemically exfoliated graphene oxide (GO) has received considerable attention compared to other approaches due to its low cost, scalability, and solution processability [247].

However, GO should be converted to rGO to restore the high conductivity of graphene. Many publications have demonstrated the various reduction processes for rGO, including thermal, microwave, photo, chemical, electrochemical, and solvothermal reduction. Geng et al. reported a simple approach for preparing a transparent and conductive graphene film using controlled chemical reduction of exfoliated GO [248]. Bao et al. reported that post-annealing process at high temperature (>800℃) was required to obtain rGO having good electrical properties [249]. Although conventional thermal reductions have been reported to be more effective than chemical reduction processes, most previous investigations were performed at high temperature with long reaction times (>70 h), making it difficult to apply these process to flexible substrates such as plastics. Moreover, these rGOs suffered from

limitations such as high surface resistance and low transparency, resulting in degraded electrical properties.

rGO electrodes prepared by the chemical reduction of GO for flexible and transparent thin film applications did not perform as well as conventional metal electrodes due to insufficient electrical properties [250–253]. In particular, graphene-based conductive films have received less attention for use in multi-stacked organic electronic devices, which require controlled surface roughness [254]. Accordingly, an alternative reduction technique having the advantages of fast, efficient, cost-effective, and low temperature process applicable to plastic substrates is still highly desired for rGO-based thin film applications.

In this part, a novel and reliable approach was study for the preparation of rGO transparent electrodes through the combination of chemical and subsequent pressure-assisted thermal reduction at relatively low temperature (180℃) on a flexible plastic substrate. This reduction process produces rGO electrodes without the transferring or imprinting processes used in conventional synthetic approaches for graphene thin film production. Furthermore, the electrical performance of the conductive film obtained by this process was enhanced due to the dense packing of each graphene sheet. The densified rGO film formed a uniform surface with low surface resistance, allowing in practical application to gate electrode of flexible OTFTs. In a proof-of-concept demonstration, the rGO thin film-gated OTFT exhibited superior device performance in terms of mobility and on/off ratio.

rGO thin films were fabricated by three different reduction methods

involving several stepwise procedures, as shown in **Figure 44**. GO precursors were produced by Hummers methods [147]. First, the surface of polyethersulfone (PES) film was modified by O_2 plasma treatment at ambient pressure to increase the wettability of the relatively hydrophobic substrate. In addition, the solution wettability of the substrate is affected by the chemical interaction between the GO solution and the substrate. In this study, GO thin films were readily deposited on the PES substrate with a good uniformity and coverage using a mixed solvent of ethanol and water. Additive ethanol in the GO suspension can also control the surface chemistry and increase the uniformity and coverage of GO on the modified hydrophilic PES substrate [247]. Although enhanced wettability increased the coverage of GO flakes on the substrate, it can also become thermodynamically unstable and discontinuous within several nanometers [244]. Therefore, repeated spin-coating and drying steps were carried out to create a continuous two-dimensional (2-D) GO thin film electrode with thickness of ~10 nm (**Figure 45**) that completely covered the substrate for incorporation into large-area electronics.

After spin-coating, electrically conductive rGO thin films were fabricated by reduction using chemical, chemical with thermal, and chemical with pressure-assisted thermal treatments. Hydrazine vapor at 100℃ was introduced to reduce the GO thin film, resulting in agglomerated rGO layers that formed a chemically reduced graphene oxide (CRGO) thin film. Additional thermal reduction at relatively high temperature is required because chemical reduction alone is not sufficient to achieve the theoretical reduction

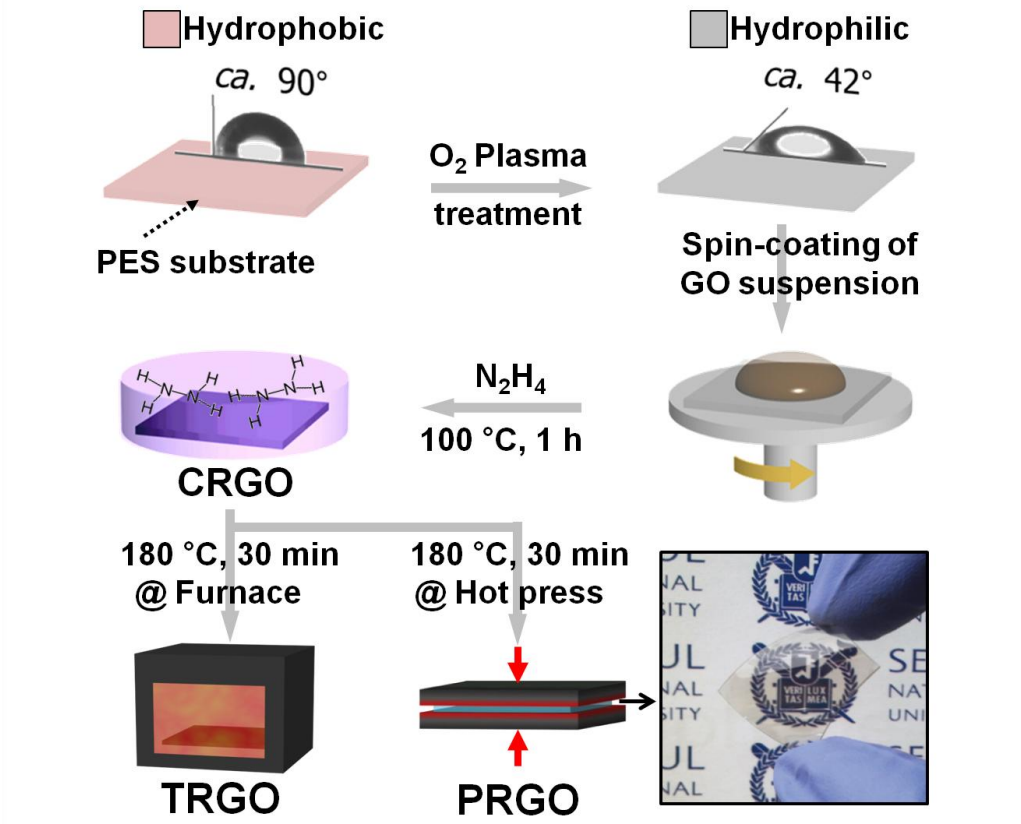

Figure 44. Schematic illustration of PRGO thin film electrode fabrication by pressure-assisted thermal reduction.

limit [255]. Therefore, subsequent reduction was carried out by loading the CRGO thin film in a furnace or hot press to enhance the reduction efficiency of thermally reduced graphene oxide (TRGO) or pressure-assisted thermally reduced graphene oxide (PRGO) thin films, respectively. The temperature of both processes was kept at 180℃ for performance comparisons. In conventional thermal reduction, high temperatures (>800℃) are necessary to restore the sp^2 carbon network; such temperature are not applicable for real application using plastic substrates [249,256]. After chemical treatment, thermal reduction occurred via heat transfer through the surrounding gas in a convection oven. Unlike the chemical and subsequent thermal reductions, sufficient dissociation energy was transferred at the interface between the heat source and the GO film via the PES substrate, resulting in enhanced heat flow from the heat source to the multi-stacked GO layers. Therefore, a new approach with pressure-assisted thermal reduction at relatively low temperature allows sufficient energy to reduce GO films compared to conventional chemical and/or high-temperature reduction.

A low sheet resistance is a prerequisite for rGO thin film applications to organic electrodes in electronic devices. **Figure 46** shows sheet resistance values for various reduction methods measured by the four-probe method. Minimum sheet resistance values for CRGO, TRGO, and PRGO films were determined to be 190, 8.0, and 1.1 kΩ/sq, respectively. Sheet resistance was highly dependent on the degree of reduction, the presence of residual oxygen and nitrogen moieties, and the defects. The CRGO thin film exhibited the

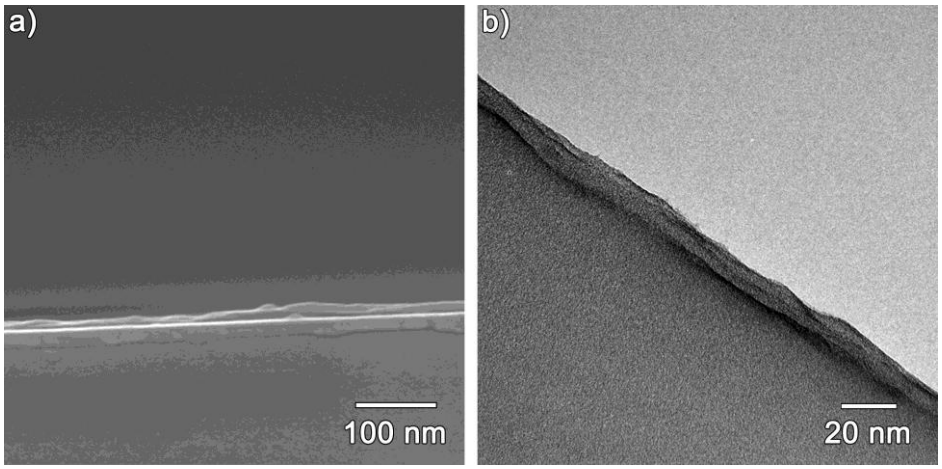

Figure 45. (a) SEM and (b) microtomed TEM image for cross sectional view of CRGO thin film.

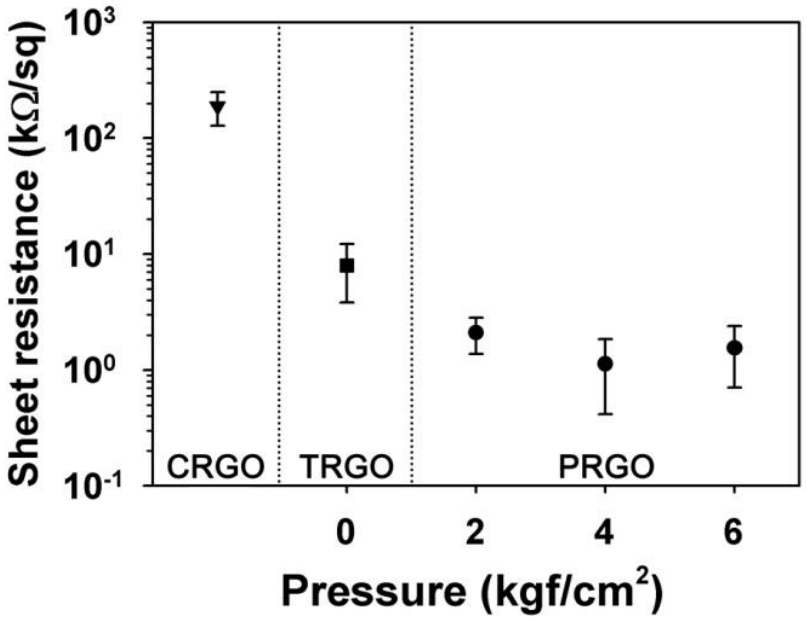

Figure 46. Comparison of surface resistance for different reduction methods according to pressure.

highest sheet resistance among three films prepared by different reduction methods [257]. For the PRGO film, sheet resistances decreased to ~10^0 kΩ/sq with increasing pressure at about 78% of optical transparency (**Figure 47**). Notably, the sheet resistance of the PRGO thin film was approximately two orders of magnitude less than that of the CRGO thin film because the sp^2 carbon network was further restored during pressure-assisted thermal reduction. Furthermore, the mechanical fatigue was investigated using a bending test machine to confirm the feasibility of using PRGO films as flexible organic electrodes. **Figure 48** shows that the sheet resistance of PRGO thin film varied little up to 3000 bending cycles and perfectly recovered after unbending. Thus, electrical properties were improved over several orders of magnitude by pressure-assisted thermal reduction, and mechanical flexibility was maintained over thousands of cycles, making PRGO films potentially useful for flexible, transparent, and conductive electrodes.

To elucidate the origin of the decrease of sheet resistance, the surface morphologies of CRGO, TRGO, and PRGO thin films were further investigated by FE-SEM and AFM. The surface of the PRGO thin film was dramatically flattened compared to those of CRGO and TRGO thin films. The wrinkles shown in **Figure 49(a)** are characteristic of CRGO, corresponding to the images of published in the literatures [258,259]. In general, the wrinkles are associated with the thermal expansion coefficient difference between the substrate and GO layers [260]. Furthermore, the wrinkles cause surface roughness that acts as defects to higher sheet resistance. Not only the high

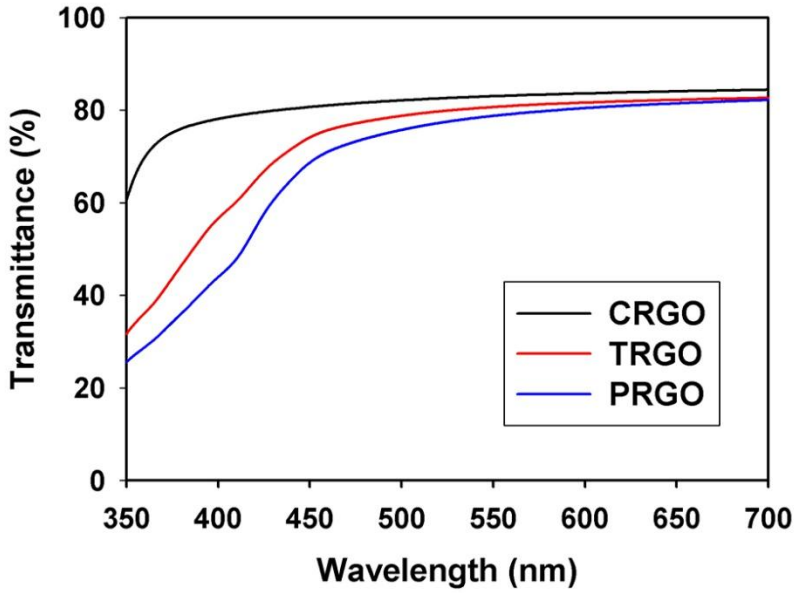

Figure 47. UV-Vis spectra of CRGO, TRGO, and PRGO. Transmittances of each material at 550 nm are 83.0, 80.6, and 78.7 %, respectively.

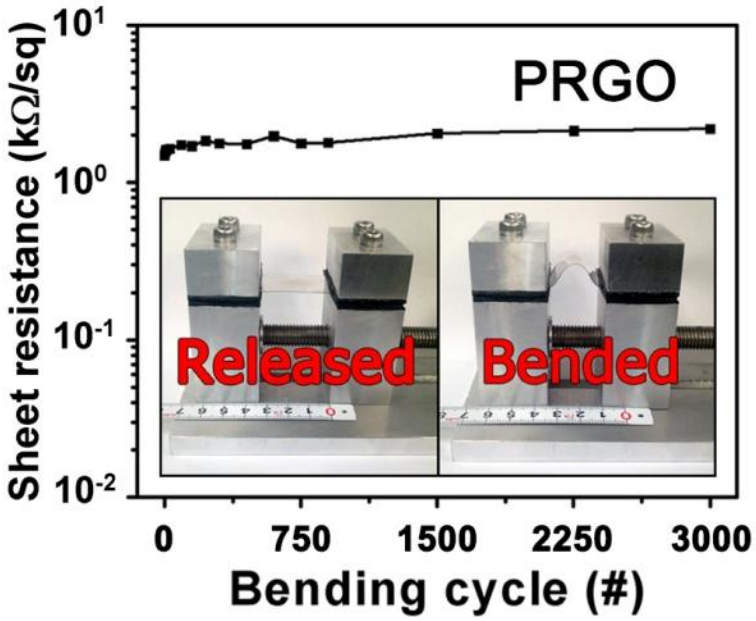

Figure 48. Continuous bending fatigue test of the PRGO thin film.

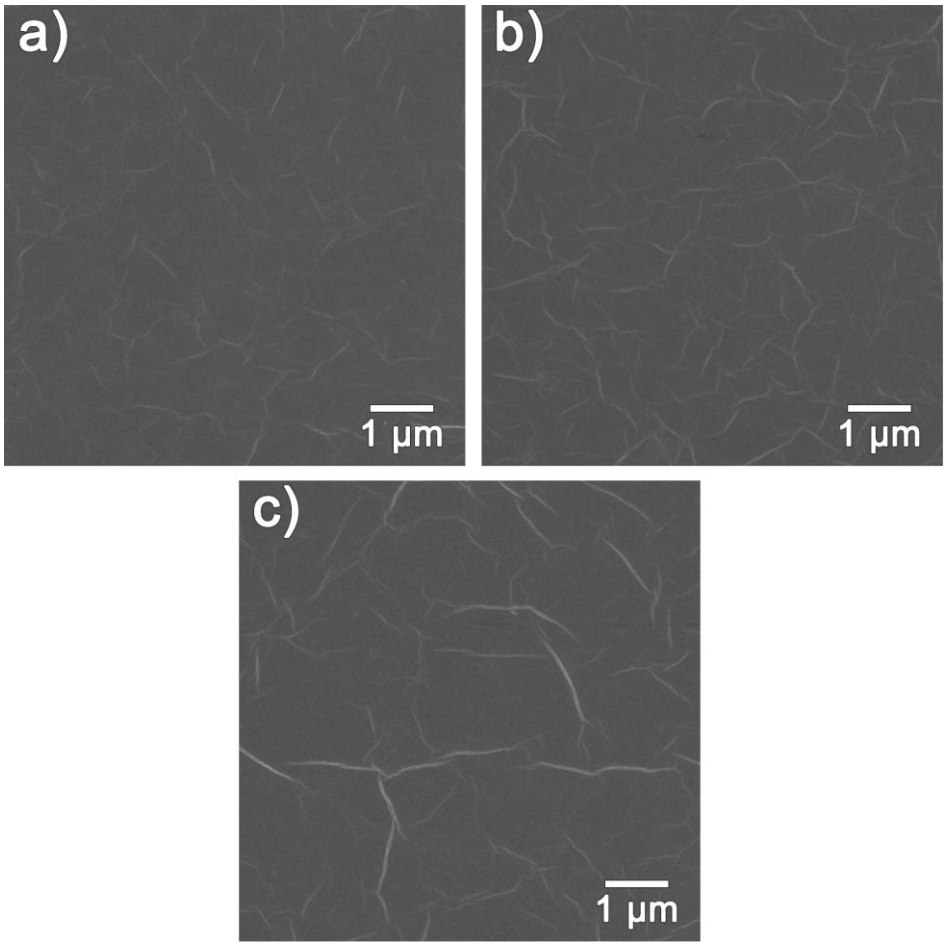

Figure 49. SEM images of (a) CRGO, (b) TRGO, and (c) PRGO films, respectively.

sheet resistance of the CRGO film but also its rough surface can potentially limit the integration of CRGO film into organic electronics because the roughness of the bottom layer of a device often governs the interface and morphology of the upper layer, which may result in highly torturous current flow [261]. In contrast, the TRGO and PRGO thin films had fewer wrinkles compared to the CRGO film in **Figure 49(b) and (c)**. Particularly, there is very little existence of wrinkles in the PRGO thin film because the thermal expansion coefficient of PRGO shifted to the positive direction due to increased interaction between the PRGO sheets and the substrate [262]. Moreover, the transparent and flexible PES substrate used in these experiments has two benzene rings in its monomer structure. The substrate also provides greater interaction with graphene sheets compared to conventional SiO_2 substrates, leading to fewer wrinkles and decreased surface roughness.

Figure 50(a), (b) and (c) illustrate 2-D AFM images of the surface topographies of CRGO, TRGO and PRGO, respectively. Based on AFM measurements, the RMS roughness values of CRGO, TRGO, and PRGO thin films were 10.1, 4.78, and 1.61 nm, respectively, and were measured for an area of 5 μm × 5 μm. The decreasing trend in surface roughness indicated that the pressure-assisted thermal reduction process provided a much smoother PRGO thin film compared to conventional chemical and/or thermal reduction processes. Low surface roughness is closely related to low sheet resistance [263,264]. Thus, the PRGO thin film with a flat surface topography exhibited superior electrical properties, which could have potential application in organic

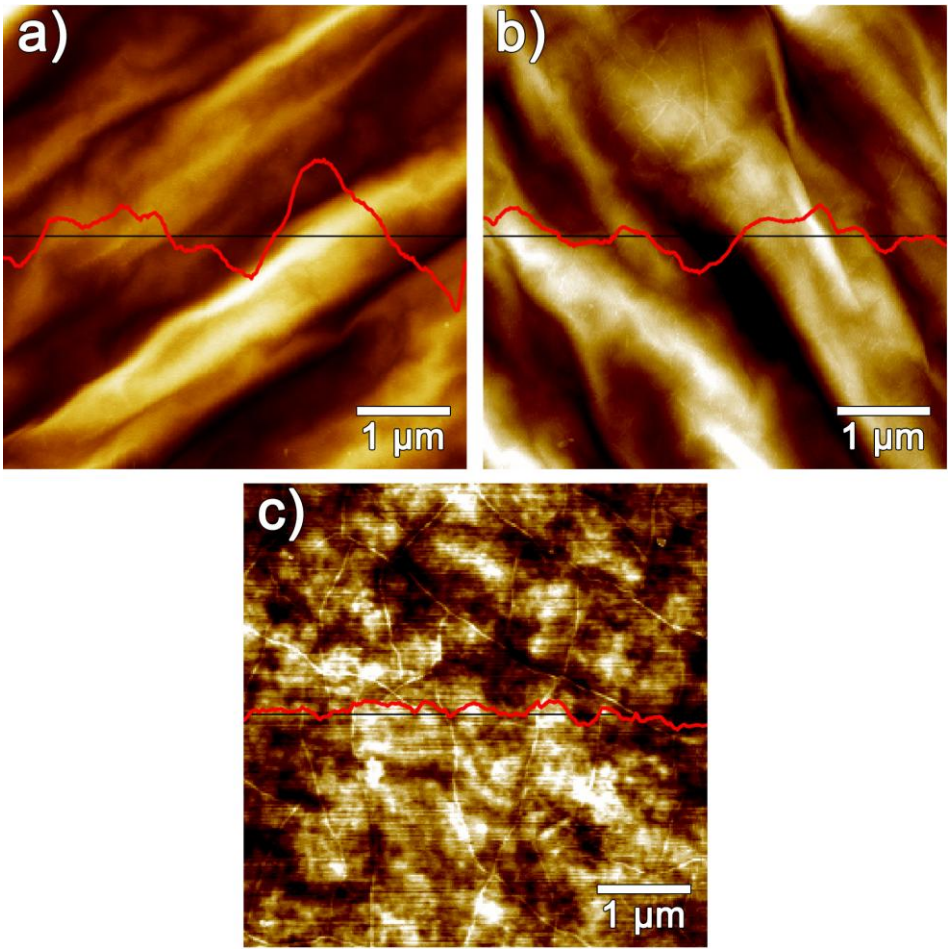

Figure 50. AFM images of (a) CRGO, (b) TRGO, and (c) PRGO films, respectively.

electronic devices.

XPS analysis was performed to determine the content and configuration of carbon, oxygen, and nitrogen in rGO films prepared by different reduction methods. The conventional CRGO showed the characteristic C−C peak at 284.5 eV, as well as four additional peaks that were deconvoluted, indicating the presence of functional groups; C–N at 285.5 eV, C–O at 285.5 eV, C=O at 287.5 eV, and O–C=O at 289.4 eV. Less oxygen and nitrogen were observed in PRGO compared to CRGO and the TRGO in **Figure 51**. Furthermore, the C/O atomic ratio was analyzed to evaluate the degree of reduction of GO. The C/O atomic ratio of GO, CRGO, TRGO and PRGO were 3.0, 6.9, 8.6, and 10, respectively (**Table 6**). The high C/O ratio of PRGO resulted from the high degree of reduction, providing higher electrical conductivity compared to CRGO and TRGO. These results correspond to low sheet resistance as shown in **Figure 46**. Thus, the pressure-assisted thermal reduction process is an outstanding method for removing functional groups and impurities at a low temperature of 180℃.

XRD analysis was used to measure the interlayer spacing between graphene multi-layers, which corresponded to the degree of reduction of rGO. In **Figure 52**, the XRD patterns of rGO prepared using different reduction methods exhibited a peak at around 24°, which is a typical characteristic of rGO. The rGO peak appeared at a higher angle in PRGO than in CRGO and TRGO. The interlayer spacings of CRGO, TRGO, and PRGO, calculated based on their 2θ position using Bragg's law, were 0.430, 0.382 and 0.364 nm,

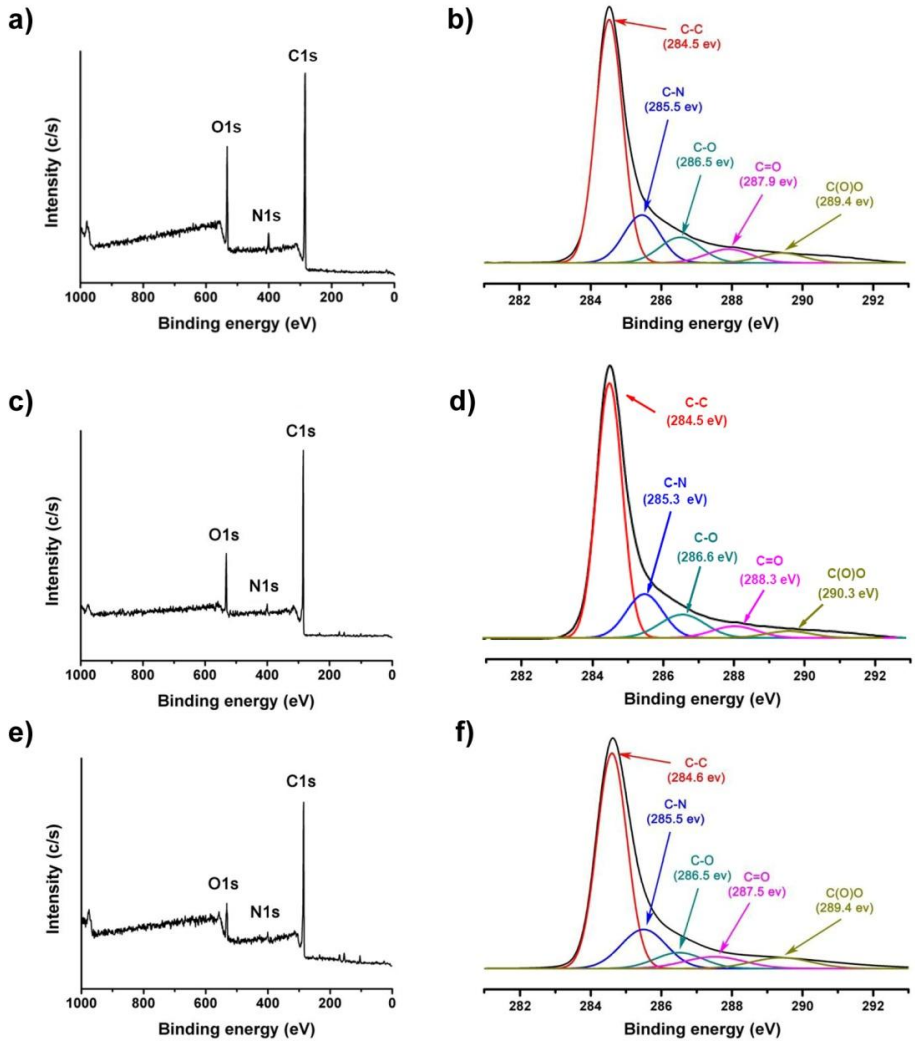

Figure 51. High-resolution XPS analysis of the effect of different reduction treatments on rGO thin films. (a), (c), (e) XPS survey spectra and (b), (d), (f) XPS C1s spectra of CRGO, TRGO, and PRGO, respectively.

Table 6. C/O atomic ratios of GO and rGO according to reduction method.

	GO	CRGO	TRGO	PRGO
C/O ratio	3.0	6.9	8.6	10

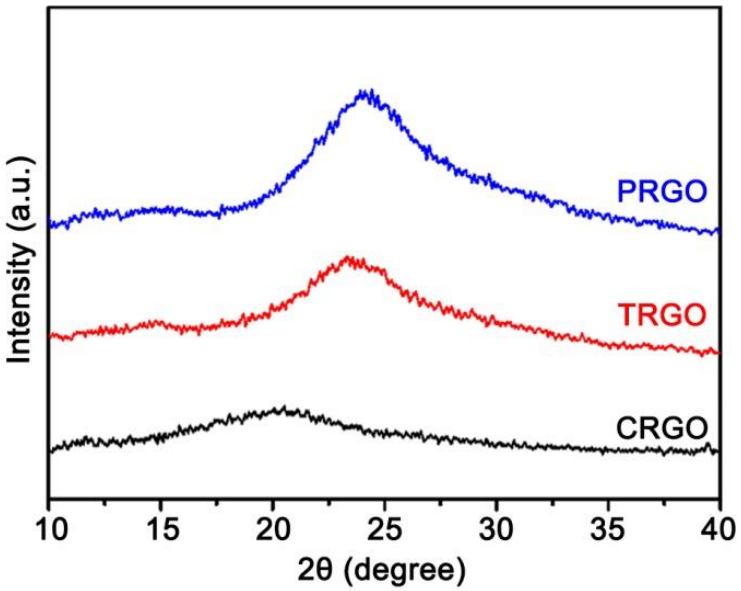

Figure 52. XRD patterns of CRGO, TRGO, and PRGO.

respectively. The relatively small interlayer spacing of PRGO suggests a denser packing of multi-layers compared to CRGO or TRGO [265]. These results are similar to the intrinsic interlayer spacing of graphite, indicating good reduction of GO by pressure-assisted thermal reduction [266]. Thus, a small interlayer spacing indicates the removal of oxygen- and nitrogen-containing functional groups from GO and subsequent restoration of the sp^2 carbon network.

The novel reduction process used in this study resulted in PRGO thin film with low sheet resistance and low surface roughness due to higher restoration of the conjugated π-orbital system and smaller interlayer spacing compared to CRGO and TRGO thin films. In this point of view, understanding the mechanism by which the pressure-assisted thermal reduction process reduces GO is important. **Figure 53** shows a schematic diagram comparing the heat flow during thermal reduction in the furnace and the hot press. The heat flow via different reduction processes was correlated with reduction efficiency based on the contact area at the interface between the heat source and the PES substrate. In the case of thermal reduction in a furnace, the surfaces of the two bodies, consisting of the upper side of the heat source and the bottom face of PES film, were not uniform, leading to the formation of voids. Heat transfer by thermal reduction process can occur in voids as well as between two solid bodies via electromagnetic fields, heat diffusion, and direct contact. In the case of pressure-assisted thermal reduction, however, pressure can squeeze the two bodies between the CRGO film and the substrate, minimizing the number of

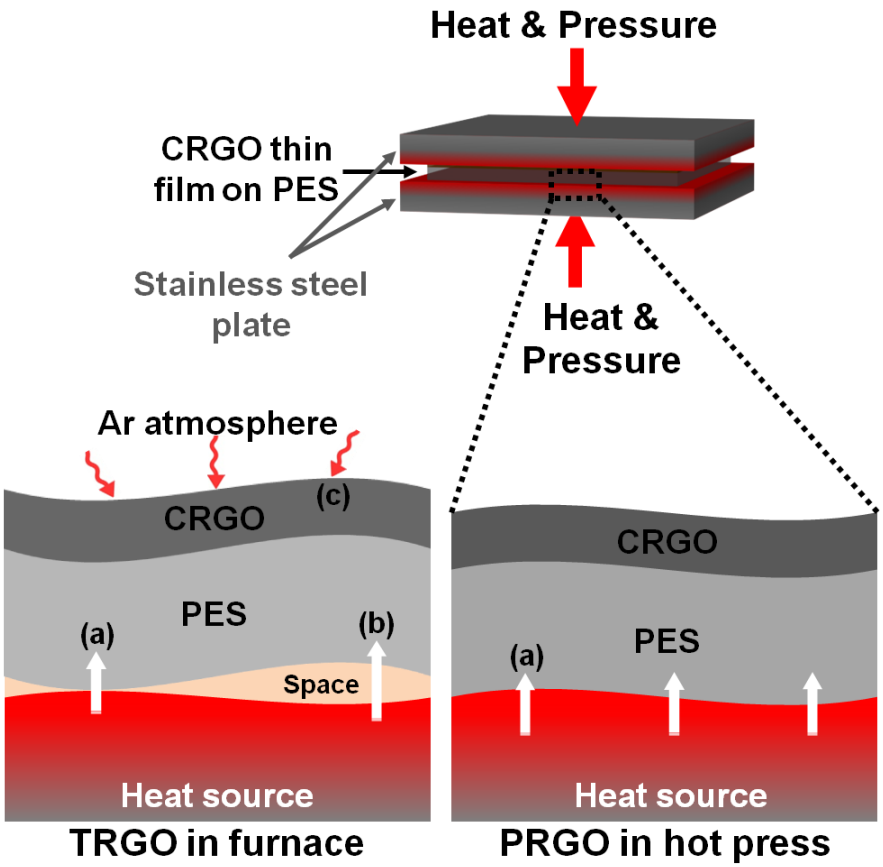

Figure 53. Schematic illustration of heat transfer from the heat source to CRGO thin films via (a) direct contact, (b) electromagnetic field and/or heat diffusion, and (c) convection and radiation.

voids and to maximizing the area of direct contact. Heat flow by direct contact in a hot press is 100 times stronger than that by indirect and convective heat transfer in a furnace at the same reduction temperature [267]. Furthermore, the upper body of the hot press confines the thermal energy inside GO layers, thereby enhancing the heat transfer from the heat source to GO. As a result, pressure-assisted thermal reduction transfers sufficient energy to dissociate functional groups from GO thin films, increasing the reduction efficiency and C/O ratio. This hypothesis is consistent with our experimental data. Therefore, the proposed process offers an alternative route for the reduction of GO from a GO suspension, allowing device fabrication on any plastic substrate.

Pressure-assisted thermal reduction enabled the simple fabrication of a high-performance OTFT with a flexible, transparent, and flat PRGO thin-film electrode having superior electrical properties. Bottom-gate OTFTs were prepared using thermally evaporated gold and pentacene as a source/drain (S/D) electrode and semiconductor, respectively (**Figure 54**). **Figure 55** shows (a) drain current–drain voltage (I_D–V_D) and (b) drain current–gate voltage (I_D–V_G) characteristics of fabricated OTFTs. Under the experimental conditions, a field-effect mobility of 0.18 ± 0.04 $cm^2 V^{-1} s^{-1}$, a threshold voltage of −18.18 V, and an on/off current ratio of 6.94×10^4 were obtained. The PRGO electrodes showed superior electrical performance due to reduced contact resistance resulting from the smooth surface of the graphene electrode [268].

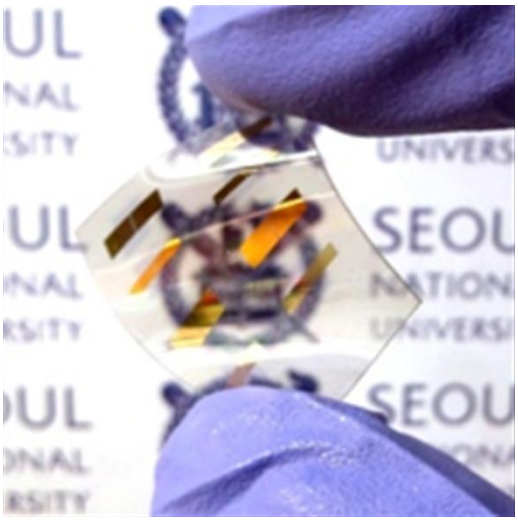

Figure 54. Optical image of the PRGO-gated OTFTs.

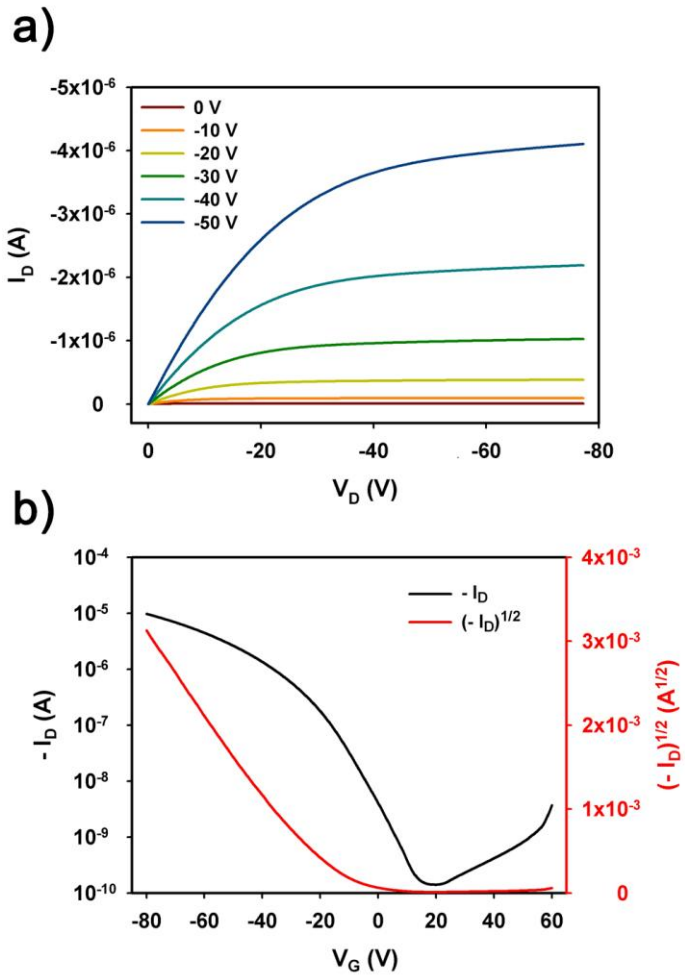

Figure 55. Electrical output and transfer characteristics of pentacene OTFT with PRGO gate electrode.

3.3.3. PANI/CSA gate and Ag source/drain electrode by using inkjet printing method for organic thin film transistor

Organic TFTs are envisaged as key electronic components for future electronic devices [269–272]. Along with the advancement in organic electronics in general, organic TFTs will lead to development of flexible, shatterproof, light-weight, and highly portable displays, like those in the future-generation smart phones and tablet PCs, by enabling the flexible pixel-switching devices. However, most of conventional organic TFTs have so far been constructed with electrodes made of expensive materials such as gold, silver, or ITO, and brittle inorganic gate insulators such as silicon dioxide (SiO_2). Especially, these inorganic materials for electrodes are processed with low yield, despite their energy-intensive, high-cost processing, which have been a main obstacle in realizing flexible displays. For this reason, it has become more important to investigate various materials as alternative flexible electrodes. Among them, PANI has been considered as a promising candidate for low-cost and flexible electrodes because of its high conductivity, solution processability, long-term stability, and superior mechanical flexibility [273,274]. Secondary doping of PANI with CSA in *m*-cresol enables highly-conductive solution-processed electrodes on various substrates [275,276].

In this study, all-solution-processed flexible organic TFTs were fabricated with TIPS-pentacene as a semiconductor. TIPS-pentacene was chosen because it is solution-processable and has high mobility [277,278]. In order to demonstrate fabrication of flexible devices by full solution-processing, it was

applied that PANI/CSA as gate electrodes, PES as a substrate, crosslinked pentaerythritol triacrylate (PETA) as a gate insulator, and silver ink as source and drain electrodes. The PANI/CSA and PETA have good compatibility with the PES substrate, enabling mechanically stable and flexible devices. The optimized fabrication conditions of TIPS-pentacene TFTs with PANI-based gate electrodes are shown. This study also, for the first time, compares performance of TIPS-pentacene devices based on PANI/PETA systems and Si/SiO_2 systems showing better performance from PANI/PETA-based devices, and correlates the performance with the surface morphology of TIPS-pentacene.

Bottom-gate TIPS-pentacene TFTs were fabricated, consisting of printed silver source/drain electrodes, and SiO_2 gate insulator (GI) on a Si substrate as a gate electrode or a polymer insulator on a PANI gate electrode with a PES substrate (**Figure 56**). Highly conductive PANI gate electrodes were formed on the PES substrate by spin-coating a PANI/CSA solution. PANI strongly adhered to PES (**Figure 57**) to make the substrate with gate electrodes mechanically stable and flexible. The PANI gate electrodes (~700 nm thick), having macroporous structure originated from its intrinsic fibrous morphology (**Figure 58**) [279], showed a very low sheet resistance of 60 Ω/sq measured by 4-point probe system and a fair transparency of 61.2 % at 550 nm wavelength (**Figure 59**). PETA, which has a pendant hydroxyl group, is a fast curing monomer with low volatility and used for GI in organic TFT. The formation of the GI layer was facilitated by the UV curing process within a minute. Silver

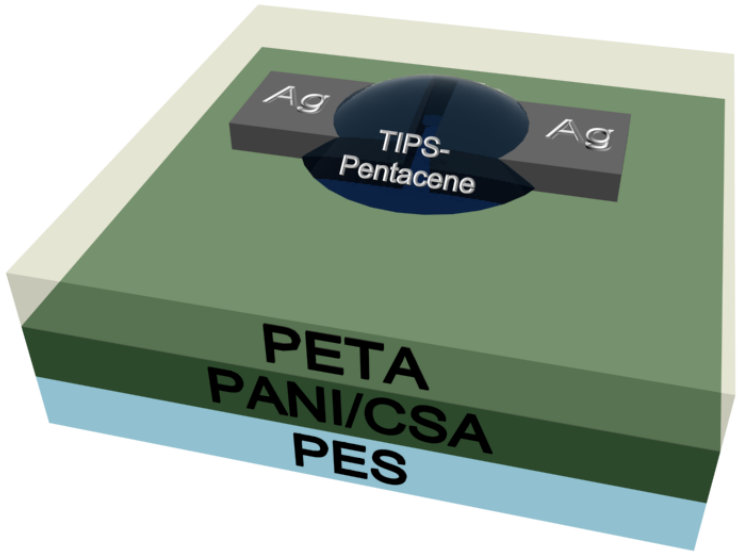

Figure 56. Schematic diagram of the PANI-gated TIPS-pentacene TFT device.

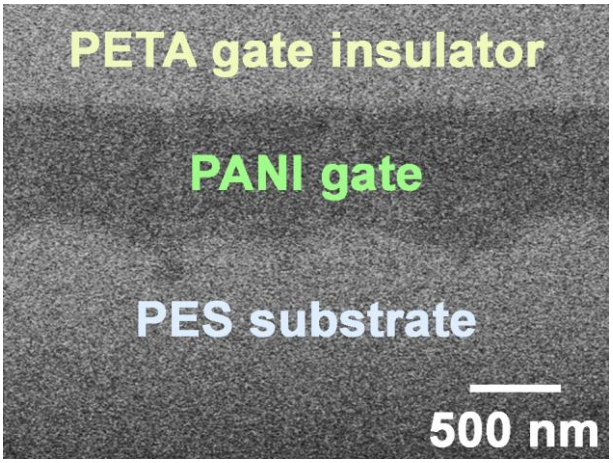

Figure 57. Cross-sectional SEM image of PANI gate electrode coated with PETA gate insulator.

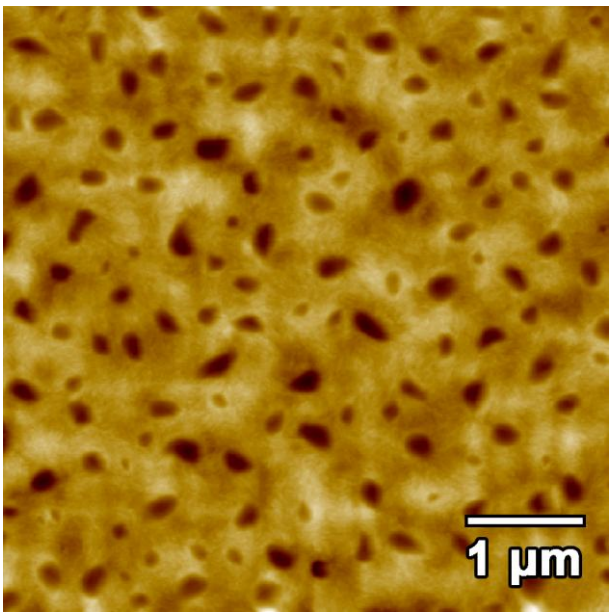

Figure 58. AFM height image of a PANI gate electrode (vertical scale 30 nm).

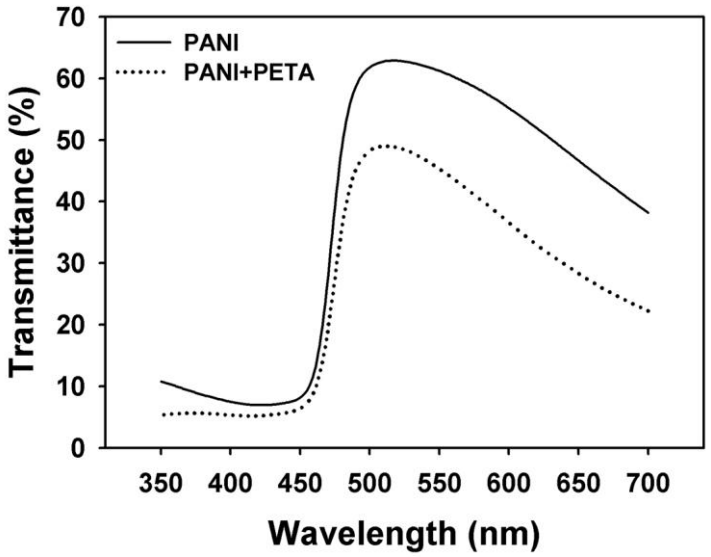

Figure 59. Optical transmittance of PANI and PANI with PETA gate insulator.

(Ag) source/drain electrodes with a rectangular shape (3 mm × 1.5 mm) were constructed on the GI layer by using inkjet printing method with a channel length of 100 μm. TIPS-pentacene was drop-casted as a semiconductor onto the channel between Ag source and drain electrodes.

The mobility of TIPS-pentacene mainly depends on the size and quality of the crystalline domains, which could be affected by deposition conditions and the nature of insulator surface [278,280,281]. Because it is predicted that the crystal of TIPS-pentacene on PETA layer above PANI gate electrode will show different growth way compared to the case of conventional architecture using Si/SiO_2, it is needed to investigate the correlation between the device performance and the crystal growth depending on the different experimental conditions. First of all, solvent effect was investigated to optimize TIPS-pentacene deposition conditions for TFTs. **Figure 60** presents electrical output and transfer characteristics of PANI-gated TFTs with three different solvents for TIPS-pentacene; (a),(b) anisole, (c),(d) chlorobenzene, and (e),(f) 1,2-dichlorobenzene. TIPS-pentacene was dissolved into each solvent for 3 h. Boiling point of anisole, chlorobenzene, and 1,2-dichlorobenzene is 154, 131, and 180 ℃, respectively. It has been reported in literatures that high field-effect mobilities are observed from slow crystal growth obtained from high boiling-point solvents or from a binary mixture of solvents when Si/SiO_2 wafers were used as gate electrode and insulator [281–284]. However, our results from PANI/PETA polymer gate electrode/insulator systems shows different results, the highest drain current (I_{DS}) and the corresponding field-effect mobility when

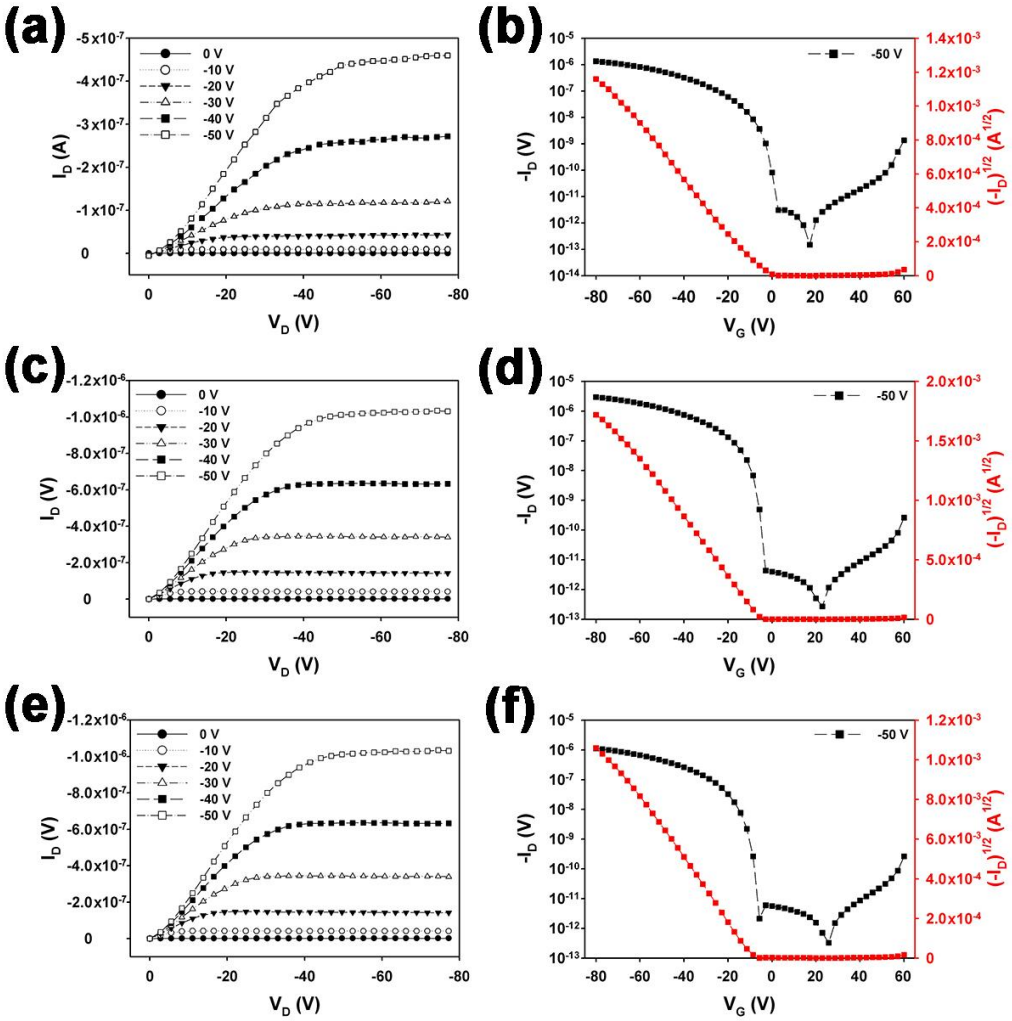

Figure 60. Electrical output and transfer characteristics of PANI-gated TFTs with three different active material solvents; (a),(b) anisole, (c),(d) chlorobenzene, and (e),(f) 1,2-dichlorobenzene.

using chlorobenzene as a solvent (**Figure 60** and **Table 7**). Therefore, different factors should be considered to understand our results on the flexible polymer gate electrode and insulator.

Next, the effect of dissolving time of TIPS-pentacene in chlorobenzene was examined. **Figure 61** displays electrical output and transfer characteristics of PANI-gated TFTs with three different dissolving times for semiconducting material; (a),(b) 3 h, (c),(d) 24 h, and (e),(f) 48 h in chlorobenzene. The best average mobility value of 0.13 cm^2/Vs was measured when TIPS-pentacene dissolved for 24 h. Therefore, it could be inferred that 3 and 48 h of dissolving time for TIPS-pentacene is not appropriate in the case of using chlorobenzene as a solvent. First, it is considered that 3 h is not enough time to disperse TIPS-pentacene molecules into chlorobenzene completely. Before the dissolving, original TIPS-pentacene agglomerated like a sharp crystal with dark blue color so that it should have more than 3 h to disperse into solvent perfectly. Second, oxygen effect could be contemplated because the TIPS-pentacene solution was prepared under ambient air condition. It is well known that the interaction of organic semiconductor with oxygen and moisture could result in the degradation of TFT performance [285,286]. It was thought that long preparation time over 24 h might lead to damage to TIPS-pentacene molecule by O-element functionalization, which could hinder regular π-π stacking arrangement of the active material. Therefore, optimized preparation time of TIPS-pentacene solution in chlorobenzene is confirmed as 24 h for this TFT configuration.

Table 7. Main parameters of all TFTs.

Parameter	Variables	Mobility* (cm^2/Vs)	On/off ratio	V_{th} (V)
TIPS-pentacene Solvent	Anisole	0.026	8.99×10^6	− 6.10
	Chlorobenzene	0.066	1.23×10^7	− 5.15
	1,2-Dichlorobenzene	0.021	3.38×10^6	− 7.94
Preparation Time	3 h	0.059	4.98×10^6	− 13.2
	24 h	0.135	1.72×10^7	− 5.82
	48 h	0.056	1.34×10^7	− 14.9
Substrate Type	PANI	0.109	8.04×10^6	− 6.19
	Si	0.019	2.23×10^5	− 13.2

*Saturation mobility at V_{DS} = − 50 V

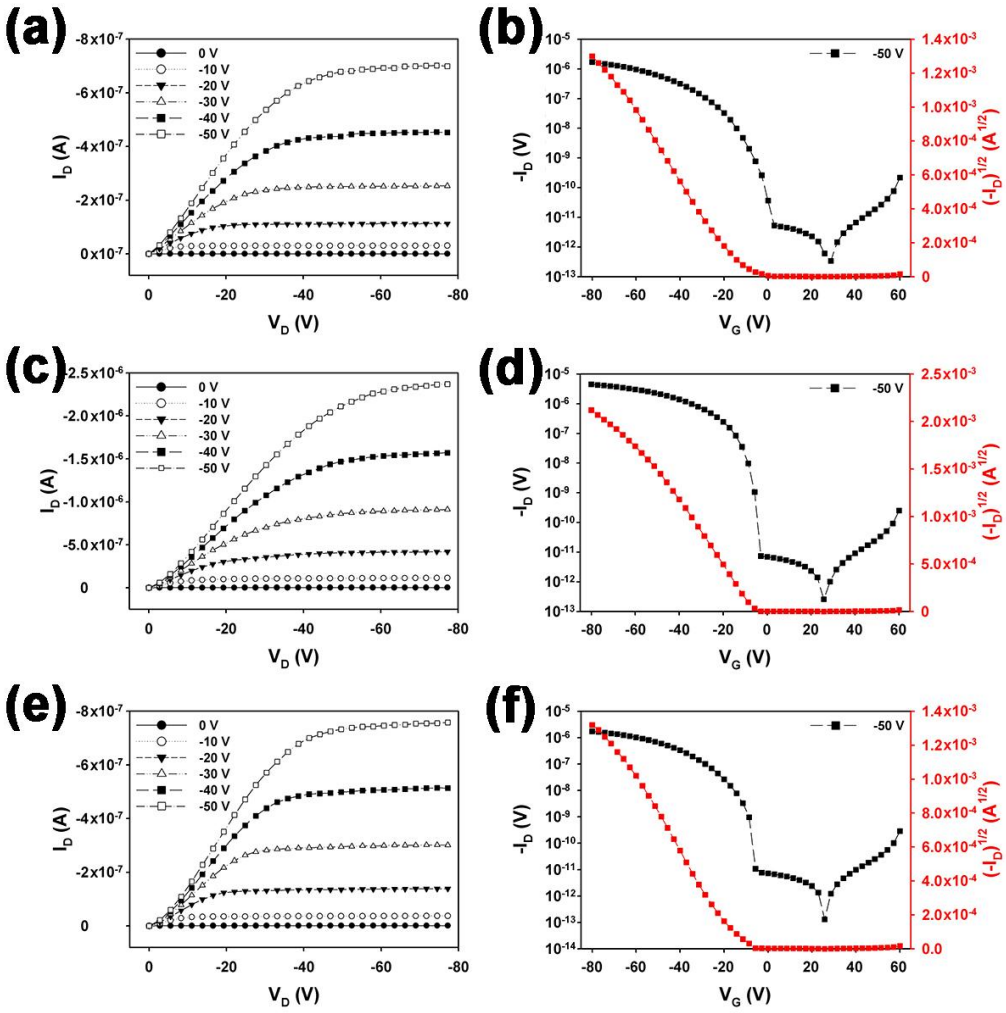

Figure 61. Electrical output and transfer characteristics of PANI-gated TFTs with three different active material dissolving times; (a),(b) 3 h, (c),(d) 24 h, and (e),(f) 48 h.

Figure 62 illustrates electrical output and transfer characteristics of PANI- and Si-gated TFTs for comparison and main parameters of the TFTs were tabulated in **Table 7**. The calculated mobility of the PANI-gated TFT is 6 times higher than that of the Si-based device. Moreover, it is noted that there is a difference in the shape of output curves of PANI- and Si-gated TFTs. As shown in **Figure 62(a)**, output curves of PANI-gated TFT look like S-shape in the linear region. These curve patterns at the small V_{DS} regime could be attributed to the charge trapping at the interface between PETA and TIPS-pentacene, resulting from the surface roughness of PETA which is almost as twice as that of SiO_2. Root-mean-square (RMS) roughness of PETA was 0.786 nm measured by AFM (**Figure 63**) and it is known that the roughness of SiO_2 is 0.3~0.4 nm depending on the surface treatment. Charges transport on the rough surface are vulnerable to be trapped compared to the smooth surface [287,288].

In spite of the disadvantage of large roughness of PETA, there are some reasons that PANI-gated TFT shows better performance. Self-assembled monolayer treatment for SiO_2 using variously functionalized chemicals has been explored to improve the device performance [289–293]. In this study, any surface modifications have been avoided for the purpose of direct comparison between PANI/PETA and Si/SiO_2 configuration. Furthermore, unlike surface roughness of GI, crystalline domain structure in the semiconductor film might have affected the mobility of both samples. The mobility of TIPS-pentacene mainly depends on the size and quality of the crystalline domains, which could

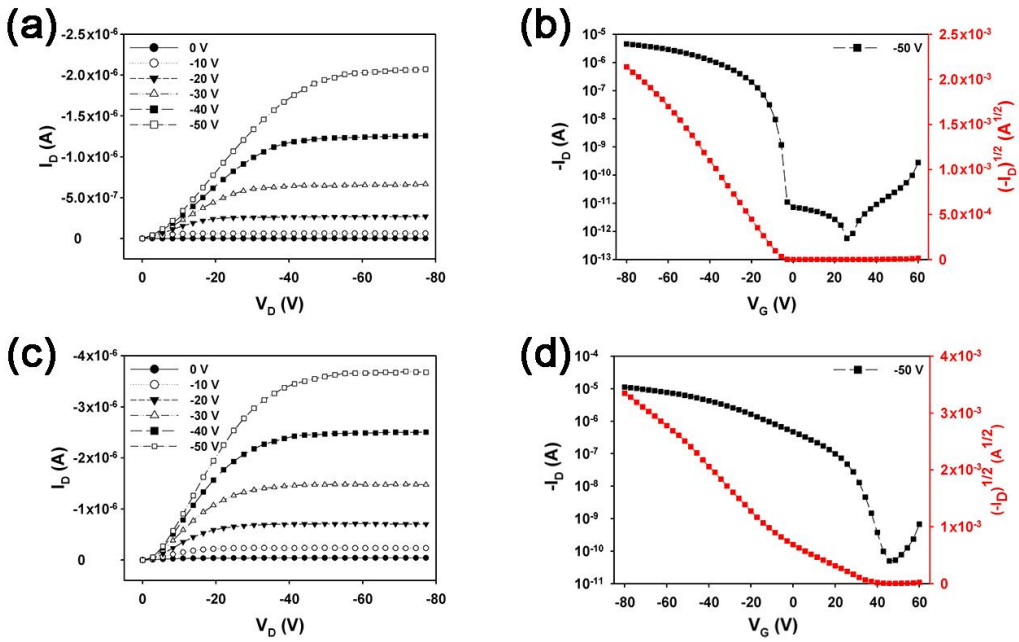

Figure 62. Current-voltage characteristics of TIPS-pentacene TFTs with (a),(b) PANI/PETA and (c),(d) Si/SiO_2 as gate electrode/gate insulator.

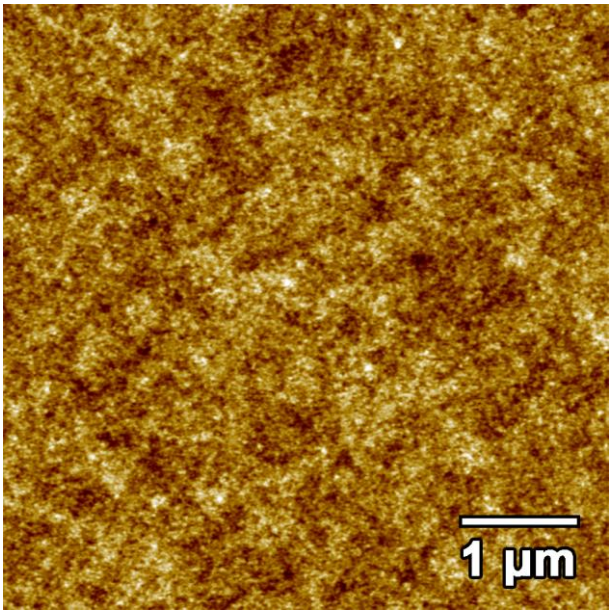

Figure 63. AFM image of a PETA GI layer (vertical scale 4 nm).

be affected by deposition conditions and the nature of insulator surface [278,280,281]. Therefore, it was needed to investigate the different growth pattern of the semiconductor on PANI/PETA and Si/SiO_2 to corroborate the correlation between the device performance and the crystal growth depending on the underlying layer.

Figure 64 reveals the photographic images of PANI- and Si-gated TFTs. As-mentioned above, high compatibility between PANI and PES produces a very clear, conductive, and flexible gate electrode. In **Figure 64(a)**, it could be seen that the area covered with gate insulator looks brighter than the bottom gate-contact area due to the pale yellow color of PETA. Gate-contact area of Si-gated TFT was formed by grinding the corner of substrate with grinder as shown in **Figure 64(b)**. Source/drain electrodes in the bottom-left corner of both TFTs do not have its active material for the purpose of measuring capacitance voltage characteristics.

Figure 65(a) and (b) demonstrate the optical microscope images of channel area in PANI-gated TFTs and **(c) and (d)** show the images in Si-gated TFTs, respectively. It could be easily observed that the morphology of TIPS-pentacene crystal is largely dependent on that of the below layer material. This different growth of crystal reconfirms assumes that the flexible PANI gate electrode has a positive effect on the performance of TIPS-pentacene TFTs compared to metal-gated devices.

AFM analysis was performed to gain insight into the difference of the surface morphology of TIPS-pentacene growth depending on the different

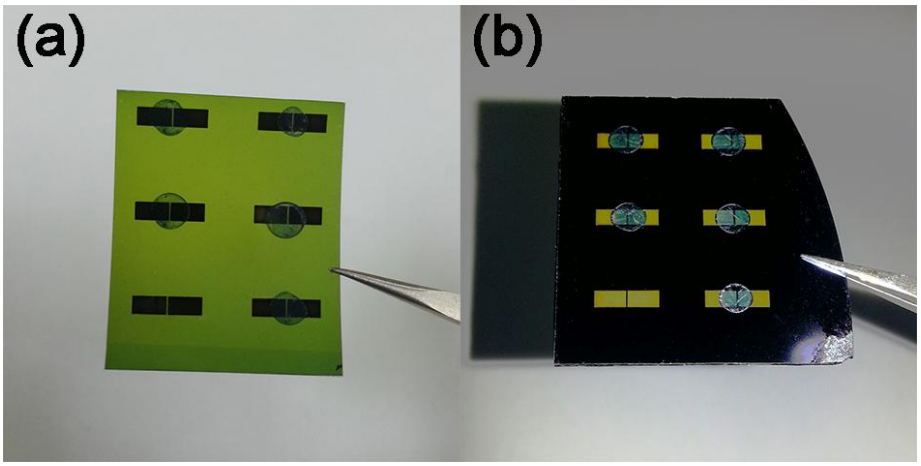

Figure 64. Photographic images of TIPS-pentacene TFTs with (a) PES/PANI/PETA and (b) Si/SiO_2.

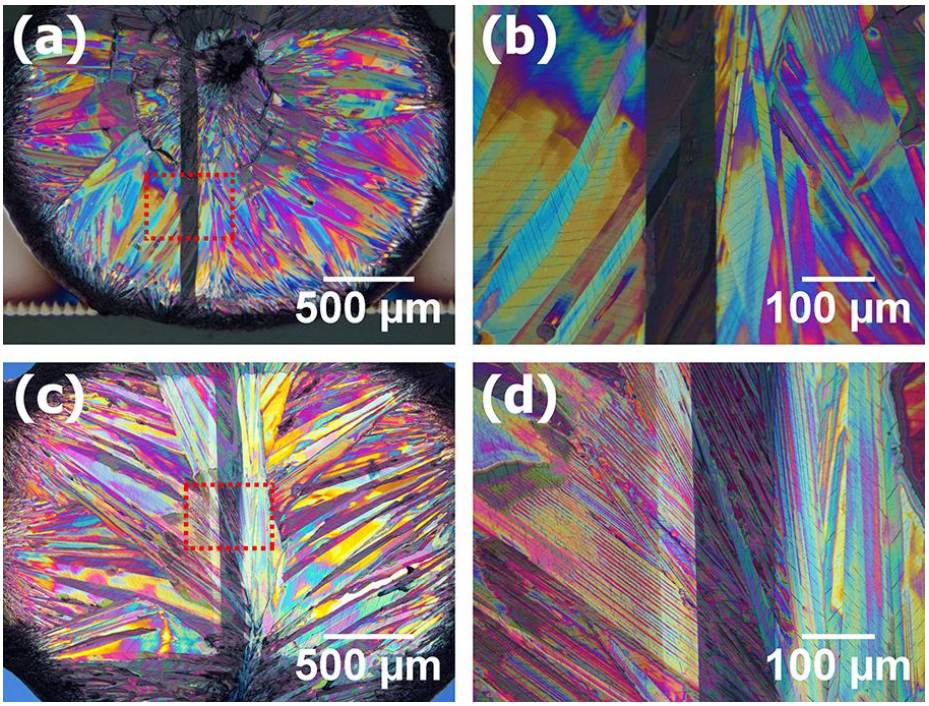

Figure 65. Optical microscope images of channel area in (a),(b) PANI- and (c),(d) Si-gated TFTs.

underlying layer. **Figure 66** exhibits AFM images of TIPS-pentacene in the channel area of each TFTs. In both PANI/PETA- and Si/SiO_2-based TFTs, three different regions can be distinguished along the transistor channel: center region as shown as **(a) and (d)**, the transition region as **(b) and (e)**, and the outer region as **(c) and (f)**. Bao et al. have also reported that the TIPS-pentacene channel can be divided into three different regions according to the morphology, and have showed that the largest field-effect mobility is observed in the transition region [294]. However, there is a significant difference in the morphology of the transition region between PANI/PETA- and Si/SiO_2-based TFTs. As presented in **Figure 66(b) and (e)**, the width of the narrow elongated crystalline domains on the PETA is larger than that on the SiO_2. It is believed that this morphological difference of the transition region is a dominant factor concerning higher mobility of PANI/PETA-based TFTs than Si/SiO_2-based TFTs. A small width of the crystalline domains in Si/SiO_2-based TFTs could yield a large resistance between crystalline domains in the channel, resulting in the reduction of the carrier mobility. Therefore, the employment of PANI/PETA systems has a great advantage in the device performance as well as high flexibility and transparency compared to Si/SiO_2 substrate.

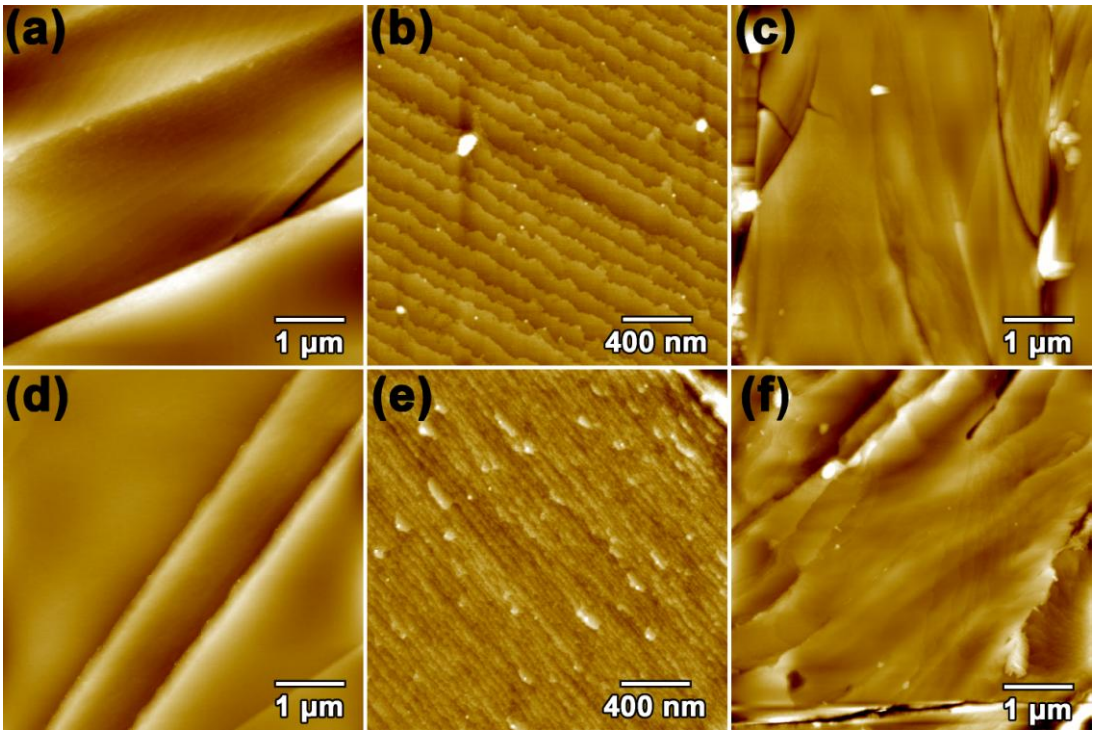

Figure 66. AFM images of TIPS-pentacene in the channel area of (a-c) PANI- and (d-f) Si-gated TFTs.

4. Conclusion

The organic electrodes were prepared using PANI, PPy and graphene. Furthermore, the organic electrodes were successfully applied to chemical sensor, dye-sensitized solar cells and organic thin film transistors. The subtopics could be concluded as follows;

1. PANI was synthesized via interfacial polymerization method and the highly conductive PANI/CSA films were fabricated by introducing novel *m*-cresol/$CHCl_3$ co-solvent system. The conductivity of PANI/CSA film increased with increasing $CHCl_3$ concentration up to 20 vol.-%. The highest average conductivity value exceeded more than 2500 S cm^{-1}, which was higher than the previously reported value (1300 S cm^{-1}). Furthermore, the highly conductive film could be applied to transducing materials for sensing NH_3 gas and the PANI/CSA sensor successfully detected as low as 2 ppm of NH_3 concentration. From these novel approaches and excellent sensor performance, this highly conductive PANI could be used for various applications such as transistor, switching element, supercapacitor, photovoltaic cell and electrochromic device.
2. A Pt and TCO-free counter electrode for DSSCs was fabricated using PANI/CSA with high conductivity and excellent catalytic ability at optimized condition. In order to obtain optimized PANI/CSA film, the thickness of film and the thermal treatment temperature were controlled.

The 1.2 μm thick PANI/CSA film heated at 100 °C demonstrated the most comparable cell performance, 84 % from front illumination and 93 % from rear illumination, compared to the performance of DSSCs with the platinized ITO counter electrode. This polymer counter electrode was specially shown the benefit of light absorption from rear side illumination because the complementary absorption properties PANI film and dye and improved transparency of PANI/CSA film by electrochromic properties. Therefore, it could be concluded that this optically transparent PANI/CSA film is a quite suitable application as a Pt and TCO-free counter electrode of bifacial DSSC.

3. PANI/CSA counter electrode was applied to organic DSSCs successfully. A novel S9 dye represents excellent light harvesting properties so that gives great energy conversion efficiency as high as 7.16 % when assembled with PANI/CSA counter electrode, which is a more improved performance than conventional metal-based N719 DSSCs. The main reason of the enhancement is due to the high molar extinction coefficient of S9 dye. Even though intrinsic structural disorder of organic material reduces the V_{oc} of the cell, large increase of the j_{sc} can make the outstanding conversion efficiency. It is clearly confirmed that the PANI/CSA counter electrode is a universal electrode which can be operated under the solar cell configuration using a novel organic dye. The application of organic dye and conducting polymer counter electrode not only provides a pretty good strategy to fabricate metal-free organic DSSCs

but also plays an important role for flexible solar cell manufacturing process.

4. OTFTs with conducting polymer S/D electrodes were fabricated by the proposed IJP-VDP method. In particular, the substitution of expensive Au electrodes to nondispersive conducting polymer PPy with top-contact structure was demonstrated for the first time in this work. Pentacene transistors based on printed PPy electrodes exhibited electrical characteristics superior to those of transistors based on thermally evaporated Au electrodes. Patterned PPy electrodes had low contact resistance at the semiconductor interface, resulting in the improved performance. This approach offers a practical strategy for patterning a nondispersive conductive polymer electrode by combining direct-write printing with VDP for flexible electronic devices.
5. A reliable and effective method was proposed for fabricating graphene-based conductive films using pressure-assisted thermal reduction. As-prepared graphene-based thin films exhibited superior optoelectronic properties, including high transparency, low sheet resistance, and mechanical flexibility. SEM and AFM analysis showed few wrinkles on the PRGO surface, leading to superior electrical properties. XPS spectra confirmed the removal of oxygen- and nitrogen-containing functional groups, corresponding to the small interlayer spacing of PRGO; these results were consistent with XRD analysis. The origin of these PRGO properties was attributed to the increased heat flow caused by greater direct

contact between heat source and the plastic substrate compared to conventional convective thermal reduction in a furnace. The proposed reduction process offers an alternative route for incorporating the fundamental properties of rGO into technologically viable devices. Finally, PRGO thin films were applied to the gate electrode of an OTFT, exhibiting superior performance compared with the conventional gold electrode. This approach is versatile and scalable, and adaptable to a wide variety of applications.

6. A highly conductive, flexible, and half-transparent polymer gate electrode was successfully prepared by spin-coating the PANI/CSA solution onto PES substrate and it was applied to TIPS-pentacene TFTs through all-solution process under the ambient air condition. It was observed that TIPS-pentacene crystal on PANI gate electrode shows different growth morphology compared to conventional Si, which might lead to enhancement of carrier mobility. Further optimizing of TIPS-pentacene preparation condition such as various solvents and dissolution time make it possible to maximize the device performance. Therefore, this approach suggests a practical strategy for fabrication of flexible electronic devices by introducing highly conductive and flexible PANI electrode.

In summary, fabrication of organic electrodes with conducting polymers and graphene has been demonstrated. A PANI electrode was prepared by drop-casting and/or spin-coating of PANI solution which was secondary-

doped with CSA dissolving in *m*-cresol. The PANI electrode was applied to chemical sensor for NH_3 gas detection, serving as a transducer at the same time. The PANI electrode worked as a counter electrode in DSSCs replacing conventional Pt counter electrode successfully. The PANI electrode also played a role of gate electrode perfectly in OTFTs with unprecedented high conductivity, flexibility and half-transparency. A PPy electrode was micro-patterned *via* inkjet printing-mediated vapor deposition polymerization method. This superb method made it possible to pattern a conducting polymer electrode even on the active material. A graphene electrode was produced *via* novel and simple pressure-assisted thermal reduction method. This highly conductive, transparent, and flexible reduced graphene oxide thin film was chosen as a gate electrode of OTFTs with high flexibility and transparency. These results strongly suggest that these organic electrodes should be potentially very useful in many new types of applications related to organic electronic devices such as actuators, sensors, photovoltaics, transistors, and supercapacitors.

References

[1] D. J. Gundlach, *Nat. Mater.* **2007**, *6*, 173.

[2] W. F. Smith, *Nat. Nanotechnol.* **2007**, *2*, 77.

[3] M. Berggren, D. Nilsson, N. D. Robinson, *Nat. Mater.* **2007**, *6*, 3.

[4] H. Klauk, *Nat. Mater.* **2007**, *6*, 397.

[5] H. Nakada, *J. Photopolym. Sci. Technol.* **2007**, *20*, 35.

[6] H. Sirringhaus, N. Tessler, R. H. Friend, *Science* **1998**, *280*, 1741.

[7] M. Baibarac, P. Gómez-Romero, *J. Nanosci. Nanotechnol.* **2006**, *6*, 289.

[8] A. Moliton, J.-M. Nunzi, *Polym. Int.* **2006**, *55*, 583.

[9] C. Waldauf, P. Schilinsky, J. Hauch, C. J. Brabec, *Thin Solid Films* **2004**, *451–452*, 503.

[10] S. Logothetidis, *Proceedings SPIE, International Offshore and Polar Engineering Conference* **2007**, p. 6732.

[11] M. Yanaka, B. M. Henry, A. P. Roberts, C. R. M. Grovenor, G. A. D. Briggs, A. P. Sutton, T. Miyamoto, Y. Tsukahara, N. Takeda, R. J. Chater, *Thin Solid Films* **2001**, *397*, 176.

[12] A. Laskarakis, S. Logothetidis, *J. Appl. Phys.* **2006**, *99*, 66101.

[13] S. Logothetidis, *Rev. Adv. Mater. Sci.* **2005**, *10*, 387.

[14] K.-H. Haas, S. Amberg-Schwab, K. Rose, G. Schottner, *Surf. Coat. Technol.* **1999**, *111*, 72.

[15] D. S. Hecht, L. B. Hu, G. Irvin, *Adv. Mater.* **2011**, *23*, 1482.

[16] Q. Wan, E. N. Dattoli, W. Y. Fung, W. Guo, Y. B. Chen, X. Q. Pan, W. Lu, *Nano Lett.* **2006**, *6*, 2909.

[17] C. Goebbert, R. Nonninger, M. A. Aegerter, H. Schmidt, *Thin Solid Films* **1999**, *351*, 79.

[18] M. Mahajeri, M. Voigt, R. N. K. Taylor, A. Reindl, W. Peukert, *Thin Solid Films* **2010**, *518*, 3373.

[19] S. Kirchmeyer, K. Reuter, *J. Mater. Chem.* **2005**, *15*, 2077.

[20] J. Yue, A. J. Epstein, Z. Zhong, P. K. Gallagher, A. G. Macdiarmid, *Synth. Met.* **1991**, *41*, 765.

[21] Y. H. Ha, N. Nikolov, S. K. Pollack, J. Mastrangelo, B. D. Martin, R. Shashidhar, *Adv. Funct. Mater.* **2004**, *14*, 615.

[22] S. De, T. M. Higgins, P. E. Lyons, E. M. Doherty, P. N. Nirmalraj, W. J. Blau, J. J. Boland, J. N. Coleman, *ACS Nano* **2009**, *3*, 1767.

[23] S. Lai, C. Ou, C. Tsai, B. Chuang, M. Ma, S. Liang, *SID Digest* **2008**.

[24] J. Y. Lee, S. T. Connor, Y. Cui, P. Peumans, *Nano Lett.* **2008**, *8*, 689.

[25] L. Hu, H. S. Kim, J. Y. Lee, P. Peumans, Y. Cui, *ACS Nano* **2010**, *4*, 2955.

[26] L. B. Hu, D. S. Hecht, G. Gruner, *Chem. Rev.* **2010**, *110*, 5790.

[27] L. Hu, D. S. Hecht, G. Gruner, *Nano Lett.* **2004**, *4*, 2513.

[28] Z. C. Wu, Z. H. Chen, X. Du, J. M. Logan, J. Sippel, M. Nikolou, K. Kamaras, J. R. Reynolds, D. B. Tanner, A. F. Hebard, A. G. Rinzler, *Science* **2004**, *305*, 1273.

[29] J. K. Wassei, R. B. Kaner, *Mater. Today* **2010**, *13*, 52.

[30] W. W. Cai, Y. W. Zhu, X. S. Li, R. D. Piner, R. S. Ruoff, *Appl. Phys. Lett.* **2009**, *95*, 123115.

[31] K. Lota, V. Khomenko, E. Frackowiak, *J. Phys. Chem. Solids* **2004**, *65*, 295.

[32] S. Suematsu, Y. Oura, H. Tsujimoto, H. Kanno, K. Naoi, *Electrochim. Acta* **2000**, *45*, 3813.

[33] J. Heinze, B. A. Frontana-Uribe, S. Ludwigs, *Chem. Rev.* **2010**, *110*, 4724.

[34] F. Louwet, D. Vanderzande, J. Gelan, J. Mullens, *Macromolecules* **1995**, *28*, 1330.

[35] R. A. Wessling, *J. Polym. Sci.: Polym. Symp.* **1985**, *72*, 55.

[36] J. H. P. Utley, J. Gruber, *J. Mater. Chem.* **2002**, *12*, 1613.

[37] N. Alpatova, G. Girina, *Russ. J. Electrochem.* **2006**, *42*, 670.

[38] M. Mueller, M. Fabretto, D. Evans, P. Hojati-Talemi, C. Gruber, P. Murphy, *Polymer* **2012**, *53*, 2146.

[39] J. Huang, J. A. Moore, J. H. Acquaye, R. B. Kaner, *Macromolecules* **2004**, *38*, 317.

[40] T. Yokozawa, Y. Nanashima, Y. Ohta, *ACS Macro Lett.* **2012**, *1*, 862.

[41] B. Carsten, F. He, H. J. Son, T. Xu, L. Yu, *Chem. Rev.* **2011**, *111*, 1493.

[42] D. C. Pina, E. Falletta, M. Rossi, *Catal. Today* **2011**, *160*, 11.

[43] T. Yamamoto, *Bull. Chem. Soc. Japan* **2010**, *83*, 431.

[44] M. C. Stefan, A. E. Javier, I. Osaka, R. D. McCullough, *Macromolecules* **2008**, *42*, 30.

[45] A. Facchetti, L. Vaccaro, A. Marrocchi, *Angew. Chem. Int. Ed.* **2012**, *51*, 3520.

[46] V. Senkovskyy, R. Tkachov, H. Komber, M. Sommer, M. Heuken, B. Voit, W. T. S. Huck, V. Kataev, A. Petr, A. Kiriy, *J. Am. Chem. Soc.* **2011**, *133*, 19966.

[47] P. Sivaraman, S. P. Mishra, A. R. Bhattacharrya, A. Thakur, K. Shashidhara, A. B. Samui, *Electrochim. Acta* **2012**, *69*, 134.

[48] Y. Z. Wang, Q. Wang, H. Y. Xie, L. P. Ho, D. M. F. Tan, Y. Y. Diao, W. Chen, X. N. Xie, *Nanoscale* **2012**, *4*, 3725.

[49] A. E. Javier, S. N. Patel, D. T. Hallinan, V. Srinivasan, N. P. Balsara, *Angew. Chem. Int. Ed.* **2011**, *50*, 9848.

[50] X. Zhou, X. Yang, *Carbon* **2012**, *50*, 4566.

[51] C. H. Lai, W. F. Lee, I. C. Wu, C. C. Kang, D. Y. Chen, L. J. Chen, P. T. Chou, *J. Mater. Chem.* **2009**, *19*, 7284.

[52] M. Kubo, C. Takimoto, Y. Minami, T. Uno, T. Itoh, M. Shoyama, *Macromolecules* **2005**, *38*, 7314.

[53] F. Huguenin, M. J. Giz, E. A. Ticianelli, R. M. Torresi, *J. Power Sources* **2001**, *103*, 113.

[54] L. Li, L. Ferng, Y. Wei, C. Yang, H. F. Ji, *J. Colloid Interface Sci.* **2012**, *381*, 11.

[55] K. S. Lee, G. B. Blanchet, F. Gao, Y. L. Loo, *Appl. Phys. Lett.* **2005**, *86*, 074102.

[56] B. Somboonsub, S. Thongyai, D. A. Scola, G. A. Sotzing, P. Praserthdam, *Synth. Met.* **2012**, *162*, 941.

[57] A. Angeli, *Gazz. Chim. Ital.* **1916**, *46*, 279.

[58] E. J. Oh, K. S. Jang, A. G. MacDiarmid, *Synth. Met.* **2002**, *125*, 297.

[59] M. C. Henry, C. C. Hsueh, B. P. Timko, M. S. Freunda, *J. Electrochem. Soc.* **2001**, *148*, 155.

[60] Q. Fang, D. G. Chetwynd, J. W. Gardner, *Sens. Actuators A* **2002**, *99*, 74.

[61] W. Schuhmann, R. Lammert, B. Uhe, H. L. Schmidt, *Sens. Actuators B* **1990**, *1*, 537.

[62] B. Deore, Z. D. Chen, T. Nagaoka, *Anal. Sci.* **1999**, *15*, 827.

[63] A. Ramanavicius, A. Kausaite, A. Ramanaviciene, *Sens. Actuators B* **2005**, *111*, 532.

[64] H. J. Liang, T. R. Ling, J. F. Rick, T. C. Chou, *Anal. Chim. Acta* **2005**, *542*, 83.

[65] B. S. Ebarvia, S. Cabanilla, F. Sevilla, *Talanta* **2005**, *66*, 145.

[66] M. Trojanowicz, M. Wcislo, *Anal. Lett.* **2005**, *38*, 523.

[67] A. Ramanaviciene, A. Ramanavicius, *Biosens. Bioelectron.* **2004**, *20*, 1076.

[68] A. de Barros, W. M. de Azevedo, F. M. de Aguiar, *Mater. Charact.* **2003**, *50*, 131.

[69] R. Pokrop, M. Zagorska, M. Kulik, B. I. Kulszewicz, B. Dufour, P. Rannou, A. Pron, E. Gondek, J. Sanetra, *Mol. Cryst. Liq. Cryst.* **2004**, *415*, 93.

[70] H. L. Schmidt, F. Gutberlet, W. Schuhmann, *Sens. Actuators B* **1993**, *13*, 366.

[71] Y. Kang, S. K. Kim, C. Lee, *Mater. Sci. Eng.* **2004**, *24*, 39.

[72] S. Pruneanu, E. Veress, I. Marian, L. Oniciu, *J. Mater. Sci.* **1999**, *34*, 2733.

[73] X. H. Wang, Y. H. Geng, L. X. Wang, X. B. Jing, F. S. Wang, *Synth. Met.* **1995**, *69*, 265.

[74] C. Chiang, A. G. MacDiarmid, *Synth. Met.* **1986**, *13*, 193.

[75] A. J. Heeger, *J. Phys. Chem.* **2001**, *105*, 8480.

[76] N. Chandrakanthl, M. A. Careem, *Polym. Bull.* **2000**, *44*, 101.

[77] T. A. Sergeyeva, N. V. Lavrik, S. A. Piletsky, A. E. Rachkov, A. V. Elskaya, *Sens. Actuators B* **1996**, *34*, 283.

[78] S. Bhadra, S. Chattopadhyay, N. K. Singha, D. Khastgir, *J. Appl. Polym. Sci.* **2008**, *108*, 57.

[79] A. V. Kulikov, V. R. Bogatyrenko, O. V. Belonogova, L. S. Fokeeva, A. V. Lebedev, T. A. Echmaeva, I. G. Shunina, *Russ. Chem. Bull., Int. Ed.* **2002**, *51*, 2216.

[80] S. Stafstrom, J. L. Bredas, A. J. Epstein, H. S. Woo, D. B. Tanner, W. S. Huang, A. G. MacDiarmid, *Phys. Rev. Lett.* **1987**, *59*, 1464.

[81] S.-K. Lee, B. J. Kim, H. Jang, S. C. Yoon, C. Lee, B. H. Hong, J. A. Rogers, J. H. Cho, J.-H. Ahn, *Nano Lett.* **2011**, *11*, 4642.

[82] H. Park, P. R. Brown, V. Bulovi, J. Kong, *Nano Lett.* **2011**, *12*, 133.

[83] T.-H. Han, Y. Lee, M.-R. Choi, S.-H. Woo, S.-H. Bae, B. H. Hong, J.-H. Ahn, T.-W. Lee, *Nat. Photonics* **2012**, *6*, 105.

[84] K. S. Kim, Y. Zhao, H. Jang, S. Y. Lee, J. M. Kim, K. S. Kim, J.-H. Ahn, P. Kim, J.-Y. Choi, B. H. Hong, *Nature* **2009**, *457*, 706.

[85] Y. Wang, Y. Shao, D. W. Matson, J. Li, Y. Lin, *ACS Nano* **2010**, *4*, 1790.

[86] T. Wang, S. Y. Zhang, C. J. Mao, J. M. Song, H. L. Niu, B. K. Jin, Y. P. Tian, *Biosens. Bioelectron.* **2012**, *31*, 369.

[87] H. L. Wang, Y. Yang, Y. Y. Liang, L. F. Cui, H. S. Casalongue, Y. G. Li, G. S. Hong, Y. Cui, H. J. Dai, *Angew. Chem. Int. Ed.* **2011**, *50*, 7364.

[88] G. H. Yu, L. B. Hu, N. A. Liu, H. L. Wang, M. Vosgueritchian, Y. Yang, Y. Cui, Z. Bao, *Nano Lett.* **2011**, *11*, 4438.

[89] W. Gao, N. Singh, L. Song, Z. Liu, A. L. M. Reddy, L. J. Ci, R. Vajtai, Q. Zhang, B. Q. Wei, P. M. Ajayan, *Nat. Nanotechnol.* **2011**, *6*, 496.

[90] S. Pang, Y. Hernandez, X. Feng, K. Müllen, *Adv. Mater.* **2011**, *23*, 2779.

[91] D. S. Hecht, L. Hu, G. Irvin, *Adv. Mater.* **2011**, *23*, 1482.

[92] D. R. Cairns, R. P. Witte II, D. K. Sparacin, S. M. Sachsman, D. C. Paine, G. P. Crawford, R. R. Newton, *Appl. Phys. Lett.* **2000**, *76*, 1425.

[93] X. Wang, L. J. Zhi, K. Mullen, *Nano Lett.* **2008**, *8*, 323.

[94] Y. H. Hu, H. Wang, B. Hu, *ChemSusChem* **2010**, *3*, 782.

[95] S. Bae, H. Kim, Y. Lee, X. Xu, J.-S. Park, Y. Zheng, J. Balakrishnan, T. Lei, H. Ri Kim, Y. I. Song, Y.-J. Kim, K. S. Kim, B. Ozyilmaz, J.-H. Ahn, B. H. Hong, S. Iijima, *Nat. Nanotechnol.* **2010**, *5*, 574.

[96] N. A. Kaskhedikar, J. Maier, *Adv. Mater.* **2009**, *21*, 2664.

[97] L. L. Zhang, X. S. Zhao, *Chem. Soc. Rev.* **2009**, *38*, 2520.

[98] R. L. McCreery, *Chem. Rev.* **2008**, *108*, 2646.

[99] D. Chen, L. Tang, J. Li, *Chem. Soc. Rev.* **2010**, *39*, 3157.

[100] A. K. Geim, K. S. Novoselov, *Nat. Mater.* **2007**, *6*, 183.

[101] T. Kim, H. Kim, S. W. Kwon, Y. Kim, W. K. Park, D. H. Yoon, A. R. Jang, H. S. Shin, K. S. Suh, W. S. Yang, *Nano Lett.* **2012**, *12*, 743.

[102] Z. Wen, S. Cui, H. Pu, S. Mao, K. Yu, X. Feng, J. Chen, *Adv. Mater.* **2011**, *23*, 5445.

[103] L. J. Cote, F. Kim, J. Huang, *J. Am. Chem. Soc.* **2008**, *131*, 1043.

[104] Z. Wang, S. Wu, J. Zhang, P. Chen, G. Yang, X. Zhou, Q. Zhang, Q. Yan, H. Zhang, *Nanoscale Res. Lett.* **2012**, *7*, 161.

[105] M. F. El-Kady, V. Strong, S. Dubin, R. B. Kaner, *Science* **2012**, *335*, 1326.

[106] M. Giovanni, A. Bonanni, M. Pumera, *Analyst* **2012**, *137*, 580.

[107] C. Nylabder, M. Armgrath, I. Lundstrom, *Anal. Chem. Symp. Ser.* **1983**, *17*, 203.

[108] A. Dubbe, *Sens. Actuators B* **2003**, *88*, 138.

[109] K. Zakrzewska, *Thin Solid Films* **2001**, *391*, 229.

[110] B. Timmer, W. Olthuis, A. van den Berg, *Sens. Actuators B* **2005**, *107*, 666.

[111] D. Nicolas-Debarnot, F. Poncin-Epaillard, *Anal. Chim. Acta* **2003**, *475*, 1.

[112] K. Maksymiuk, *Electroanalysis* **2006**, *18*, 1537.

[113] Q. Ameer, S. B. Adeloju, *Sens. Actuators B* **2005**, *106*, 541.

[114] S. Cosnier, *Electroanalysis* **2005**, *17*, 1701.

[115] U. Sree, Y. Yamamoto, B. Deore, H. Shugi, T. Nagaoka, *Synth. Met.* **2002**, *131*, 161.

[116] J. Chen, C. O. Too, G. G. Wallace, G. F. Swiegers, *Electrochim. Acta* **2004**, *49*, 691.

[117] S. Cosnier, M. Dawod, K. Gorgy, S. Da Silva, *Microchim. Acta* **2003**, *143*, 139.

[118] P. A. Fiorito, C. M. A. Brett, S. I. Córdoba de Torresi, *Talanta* **2006**, *69*, 403.

[119] M. Gerard, A. Chaubey, B. D. Malhotra, *Biosens. Bioelectron.* **2002**, *17*, 345.

[120] S. Alwarappan, A. Erdem, C. Liu, C.-Z. Li, *J. Phys. Chem. C* **2009**, *113*, 8853.

[121] N. G. Shang, P. Papakonstantinou, M. McMullan, M. Chu, A. Stamboulis, A. Potenza, S. S. Dhesi, H. Marchetto, *Adv. Funct. Mater.* **2008**, *18*, 3506.

[122] Y. Shao, S. Zhang, M. H. Engelhard, G. Li, G. Shao, Y. Wang, J. Liu, I. A. Aksay, Y. Lin, *J. Mater. Chem.* **2010**, *20*, 7491.

[123] S. Guo, D. Wen, Y. Zhai, S. Dong, E. Wang, *ACS Nano* **2010**, *4*, 3959.

[124] G. P. Keeley, A. O'Neill, N. McEvoy, N. Peltekis, J. N. Coleman, G. S. Duesberg, *J. Mater. Chem.* **2010**, *20*, 7864.

[125] T. Wang, S. Y. Zhang, C. J. Mao, J. M. Song, H. L. Niu, B. K. Jin, Y. P. Tian, *Biosens. Bioelectron.* **2012**, *31*, 369.

[126] Q. L. Hao, H. L. Wang, X. J. Yang, L. D. Lu, X. Wang, *Nano Res.* **2011**, *4*, 323.

[127] A. Bonanni, M. Pumera, *ACS Nano* **2011**, *5*, 2356.

[128] B. Zhang, Q. Li, T. H. Cui, *Biosens. Bioelectron.* **2012**, *31*, 105.

[129] J. Weickert, R. B. Dunbar, H. C. Hesse, W. Wiedemann, L. Schmidt-Mende, *Adv. Mater.* **2011**, *23*, 1810.

[130] S. Günes, H. Neugebauer, N. S. Sariciftci, *Chem. Rev.* **2007**, *107*, 1324.

[131] Y. Saito, T. Kitamura, Y. Wada, S. Yanagida, *Chem. Lett.* **2002**, *31*, 1060.

[132] Y. Saito, W. Kubo, T. Kitamura, Y. Wada, S. Yanagida, *J. Photochem. Photobiol. A. Chem.* **2004**, *164*, 153.

[133] T. Kitamura, M. Maitani, M. Matsuda, Y. Wada, S. Yanagida, *Chem. Lett.* **2001**, *30*, 1054.

[134] N. Ikeda, K. Teshima, T. Miyasaka, *Chem. Commun.* **2006**, *16*, 1733.

[135] X. Wang, L. J. Zhi, K. Müllen, *Nano Lett.* **2008**, *8*, 323.

[136] D. W. Zhang, X. D. Li, H. B. Li, S. Chen, Z. Sun, X. J. Yin, S. M. Huang, *Carbon* **2011**, *49*, 5382.

[137] Y. Kubozono, S. Haas, W. L. Kalb, P. Joris, F. Meng, A. Fujiwara, B. Batlogg, *Appl. Phys. Lett.* **2008**, *93*, 033316.

[138] A. L. Briseno, S. C. B. Mannsfeld, M. M. Ling, S. Liu, R. J. Tseng, C. Reese, M. E. Roberts, Y. Yang, F. Wudl, Z. Bao, *Nature* **2006**, *444*, 913.

[139] H. Sirringhaus, T. Kawase, R. H. Friend, T. Shimoda, M. Inbasekaran, W. Wu, E. P. Woo, *Science* **2000**, *290*, 2123.

[140] M. Halik, H. Klauk, U. Zschieschang, G. Schmid, W. Radlik, W. Weber, *Adv. Mater.* **2002**, *14*, 1717.

[141] P. Cosseddu, A. Bonfiglio, I. Salzmann, J. P. Rabe, N. Koch, *Org. Electron.* **2008**, *9*, 191.

[142] D. Li, L. J. Guo, *Appl. Phys. Lett.* **2006**, *88*, 063513.

[143] S. Kobayashi, T. Takenobu, S. Mori, A. Fujiwara, Y. Iwasa, *Appl. Phys. Lett.* **2003**, *82*, 4581.

[144] K. Hong, S. Y. Yang, C. Yang, S. H. Kim, D. Choi, C. E. Park, *Org. Electron.* **2008**, *9*, 864.

[145] C. Di, D. Wei, G. Yu, Y. Liu, Y. Guo, D. Zhu, *Adv. Mater.* **2008**, *20*, 3289.

[146] S. W. Hong, F. Du, W. Lan, S. Kim, H.-S. Kim, J. A. Rogers, *Adv. Mater.* **2011**, *23*, 3821.

[147] W. S. Hummers Jr., R. E. Offeman, *J. Am. Chem. Soc.* **1958**, *80*, 1339.

[148] J. Jang, J. H. Oh, G. D. Stucky, *Angew. Chem., Int. Ed.* **2002**, *41*, 4016.

[149] M. Wan, *Adv. Mater*. **2008**, *20*, 2926.

[150] B. S. Ong, Y. Wu, P. Liu, S. Gardner, *Adv. Mater.* **2005**, *17*, 1141.

[151] M. A. Khan, S. P. Armes, *Adv. Mater.* **2000**, *12*, 671.

[152] G. Yu, J. Gao, J. C. Hummelen, F. Wudl, A. J. Heeger, *Science* **1995**, *270*, 1789.

[153] A. G. MacDiarmid, *Angew. Chem., Int. Ed.* **2001**, *40*, 2581.

[154] T. A. Skotheim, Ed. *Handbook of Conducting Polymers*, Marcel Dekker, New York, **1986**.

[155] P. Novak, K. Muller, K. S. V. Santhanam, O. Hass, *Chem. Rev.* **1997**, *97*, 207.

[156] A. G. MacDiarmid, S. L. Mu, N. L. D. Somasiri, W. Wu, *Mol. Cryst. Liq. Cryst.* **1985**, *121*, 187.

[157] S. A. Chen, H. T. Lee, *Macromolecules* **1995**, *28*, 2858.

[158] A. G. MacDiarmid, A. J. Epstein, *Synth. Met.* **1994**, *65*, 103.

[159] T. Hino, S. Taniguchi, N. Kuramoto, *J. Polym. Sci. Part A: Polym. Chem.* **2006**, *44*, 718.

[160] S. H. Hosseini, M. Dabiri, M. Ashrafi, *Polym. Int.* **2006**, *55*, 1081.

[161] D. S. Lin, C. T. Chou, Y. W. Chen, K. T. Kuo, S. M. Yang, *J. Appl. Polym. Sci.* **2006**, *100*, 4023.

[162] Y. Cao, J. Qiu, P. Smith, *Synth. Met.* **1995**, *69*, 187.

[163] O. T. Ikkala, L. O. Pietilä, L. Ahjopalo, H. Ö sterholm, P. J. Passiniemi, *J. Chem. Phys.* **1995**, *103*, 9855.

[164] M. Reghu, C. O. Yoon, C. Y. Yang, D. Moses, P. Smith, A. J. Heeger, Y. Cao, *Phys. Rev. B* **1994**, *50*, 13931.

[165] D. Djurado, B. Gilles, P. Rannou, J. P. Travers, *Synth. Met.* **1999**, *101*, 803.

[166] J. Janata, M. Josowicz, *Nat. Mater.* **2003**, *2*, 19.

[167] Y. Cao, A. E. Kovalev, R. Xiao, J. Kim, T. S. Mayer, T. E. Mallouk, *Nano Lett.* **2008**, *8*, 4653.

[168] S. Christie, E. Scorsone, K. Persaud, F. Kvasnik, *Sens. Actuators B* **2003**, *90*, 163.

[169] D. Yang, P. N. Adams, B. R. Mattes, *Synth. Met.* **2001**, *119*, 301.

[170] W. R. Salaneck, B. Liedberg, O. Inganäs, R. Erlandsson, I. Lundström, A. G. MacDiarmid, M. Halpern, N. L. D. Somasiri, *Mol. Cryst. Liq. Cyst.* **1985**, *121*, 191.

[171] J. Tang, X. Jing, B. Wang, F. Wang, *Synth. Met.* **1988**, *24*, 231.

[172] T. Jana, A. K. Nandi, *Langmuir* **2000**, *16*, 3141.

[173] D. Yang, P. N. Adams, L. Brown, B. R. Mattes, *Synth. Met.* **2006**, *156*, 1225.

[174] O. P. Dimitriev, V. V. Kislyuk, P. S. Smertenko, *Org. Electron.* **2007**, *8*, 286.

[175] S. D. Wang, T. Miyadera, T. Minari, Y. Aoyagi, Y. Tsukagoshi, *Appl. Phys. Lett.* **2008**, *93*, 04331.

[176] G. Horowitz, M. E. Hajlaoui, *Adv. Mater.* **2000**, *12*, 1046.

[177] H. Yanagisawa, T. Tamaki, M. Nakamura, K. Kudo, *Thin Solid Films* **2004**, *464–465*, 398.

[178] C. J. Tavares, S. M. Marques, S. Lanceros-Méndez, V. Sencadas, V. Teixeira, J. O. Carneiro, A. J. Martins, A. J. Fernandes, *Thin Solid Films* **2008**, *516*, 1434.

[179] A. L. Kukla, Yu. M. Shirshov, S. A. Piletsky, *Sens. Actuators B* **1996**, *37*, 135.

[180] J. Liu, Y. Lin, L. Liang, J. A. Voigt, D. L. Huber, Z. R. Tian, E. Coker, B. Mckenzie, M. J. McDermott, *Chem. Eur. J.* **2003**, *9*, 604.

[181] B. O'Regan, M. Grätzel, *Nature* **1991**, *353*, 737.

[182] S. Colodrero, A. Mihi, L. Häggman, M. Ocaña, G. Boschloo, A. Hagfeldt, H. Míguez, *Adv. Mater.* **2009**, *21*,764.

[183] J. D. Roy-Mayhew, D. J. Bozym, C. Punckt, U. A. Aksqy, *ACS Nano* **2010**, *4*, 6203.

[184] L. Kavan, J.-H. Yum, M. K. Nazeeruddin, M. Grätzel, *ACS Nano* **2011**, *5*, 9171.

[185] M. Wu, X. Lin, A. Hagfeldt, T. Ma, *Angew. Chem. Int. Ed.* **2011**, *50*, 3520.

[186] Q. Tai, B. Chen, F. Guo, S. Xu, H. Hu, B. Sebo, X.-Z. Zhao, *ACS Nano* **2011**, *5*, 3795.

[187] K.-M. Lee, W.-H. Chiu, H.-Y. Wei, C.-W. Hu, V. Suryanarayanan, W.-F. Hsieh, K.-C. Ho, *Thin Solid Films* **2010**, *518*, 1716.

[188] J. Wang, S. Chan, R. R. Carlson, Y. Luo, G. Ge, R. S. Ries, J. R. Heath, H.-R. Tseng, *Nano Lett.* **2004**, *4*, 1693.

[189] H. D. Tran, D. Li, R. B. Kaner, *Adv. Mater.* **2009**, *21*, 1487.

[190] Q. Li, J. Wu, Q. Tang, Z. Lan, P. Li, J. Lin, L. Fan, *Electrochem. Commun.* **2008**, *10*, 1299.

[191] Z. Li, B. Ye, X. Hu, X. Ma, X. Zhang, Y. Deng, *Electrochem. Commun.* **2009**, *11*, 1768.

[192] S. Ameen, M. S. Akhtar, Y. S. Kim, O.-B. Yang, H.-S. Shin, *J. Phys. Chem. C* **2010**, *114*, 4760.

[193] N. Fuke, A. Fukui, R. Komiya, A. Islam, Y. Chiba, M. Yanagida, R. Yamanaka, L. Han, *Chem. Mater.* **2008**, *20*, 4974.

[194] X. Fang, T. Ma, G. Guan, M. Akiyama, E. Abe, *J. Photochem. Photobiol. A* **2004**, *164*, 179.

[195] Q. Wang, J.-E. Moser, M. Grätzel, *J. Phys. Chem. B* **2005**, *109*, 14945.

[196] M. Adachi, M. Sakamoto, J. Jiu, Y. Ogata, S. Isoda, *J. Phys. Chem. B* **2006**, *110*, 13872.

[197] Y. Jung, R. Joseph Kline, D. A. Fischer, R. J. Kline, M. Heeney, I. McCulloch, D. M. DeLongchamp, *Adv. Funct. Mater.* **2008**, *18*, 742.

[198] S.-H. Lee, D.-H. Lee, K. Lee, C.-W. Lee, *Adv. Funct. Mater.* **2005**, *15*, 1495.

[199] Y. Xia, J. M. Wiesinger, A. G. MacDiarmid, A. J. Epstein, *Chem. Mater.* **1995**, *7*, 443.

[200] A. P. Monkman, P. Adamas, *Synth. Met.* **1991**, *41*, 627.

[201] M. Grätzel, *Photochem. Photobiol.* **2003**, *4*, 145.

[202] M. Grätzel, *Photochem. Photobiol.* **2004**, *164*, 3.

[203] K. Hara, Z. S. Wang, T. Sato, A. Furube, R. Katoh, H. Sugihara, Y. Dan-oh, C. Kasada, A. Shinpo, S. Suga, *J. Phys. Chem. B* **2005**, *109*, 15476.

[204] K. Hara, T. Sato, R. Katoh, A. Furube, Y. Ohga, A. Shinpo, S. Suga, K. Sayama, H. Sugihara, H. Arakawa, *J. Phys. Chem. B* **2003**, *107*, 597.

[205] D. P. Hagberg, T. Edvinsson, T. Marinado, G. Boschloo, A. Hagfeldt, L. Sun, *Chem. Commun.* **2006**, *21*, 2245.

[206] S. Ferrere, B. A. Gregg, *New J. Chem.* **2002**, *26*, 1155.

[207] K. Sayama, K. Hara, Y. Ohga, A. Shinpou, S. Suga, H. Arakawa, *New J. Chem.* **2001**, *25*, 200.

[208] K. Hara, T. Horiguchi, T. Kinoshita, K. Sayama, H. Sugihara, H. Arakawa, *Chem. Lett.* **2000**, *29*, 316.

[209] K. Sayama, S. Tsukagoshi, T. Mori, K. Hara, Y. Ohga, A. Shinpou, Y. Abe, S. Suga, H. Arakawa, *Sol. Energy Mater. Sol. Cells* **2003**, *80*, 47.

[210] T. Horiuchi, H. Miura, S. Uchida, *Chem. Commun.* **2003**, *24*, 3036.

[211] G. Boschloo, A. Hagfeldt, *Acc. Chem. Res.* **2009**, *42*, 1819.

[212] Z. Zhang, P. Chen, T. N. Murakami, S. M. Zakeeruddin, M. Grätzel, *Adv. Funct. Mater.* **2008**, *18*, 341.

[213] V. V. Pavlishchuk, A. W. Addison, *Inorg. Chim. Acta* **2000**, *298*, 97.

[214] T. Bessho, E. Yoneda, J.-H. Yum, M. Guglielmi, L. Tavernelli, H. Lmai, U. Rothlisberger, M. K. Nazeeruddin, M. Grätzel, *J. Am. Chem. Soc*. **2009**, *131*, 5930.

[215] L. Schmidt-Mende, U. Bach, R. Humphry-Baker, T. Horiuchi, H. Miura, S. Ito, S. Uchida, M. Grätzel, *Adv. Mater.* **2005**, *17*, 813.

[216] Z.-S. Wang, Y. Cui, Y. Dan-oh, C. Kasada, A. Shinpo, K. Hara, *J. Phys. Chem. C* **2007**, *111*, 7224.

[217] N. Onozawa-Komatsuzaki, O. Kitao, M. Yanagida, Y. Himeda, H. Sugihara, K. Kasuga, *New J. Chem.* **2006**, *30*, 689.

[218] A. Fleissner, H. Schmid, C. Melzer, H. Von Seggern, *Appl. Phys. Lett.* **2007**, *91*, 242103.

[219] T. Miyadera, S. D. Wang, T. Minari, K. Tsukagoshi, Y. Aoyagi, *Appl. Phys. Lett.* **2008**, *93*, 033304.

[220] A. Carbone, C. Pennetta, L. Reggiani, *Appl. Phys. Lett.* **2009**, *95*, 233303.

[221] X. Y. Chen, H. Zhu, S. D. Wang, *Appl. Phys. Lett.* **2010**, *97*, 243301.

[222] Y. Jang, Y. D. Park, J. A. Lim, H. S. Lee, W. H. Lee, K. Cho, *Appl. Phys. Lett.* **2006**, *89*, 183501.

[223] Z. Bao, Y. Feng, A. Dodabalapur, V. R. Raju, A. J. Lovinger, *Chem. Mater*. **1997**, *9*, 1299.

[224] B. J. Kim, H. J. Kim, T. S. Yoon, Y. S. Kim, D. H. Lee, Y. Choi, B. H. Ryu, H. H. Lee, *J. Ind. Eng. Chem.* **2003**, *9*, 25.

[225] M. Halik, H. Klauk, U. Zschieschang, T. Kriem, G. Schmid, W. Radlik, K. Wussow, *Appl. Phys. Lett.* **2002**, *81*, 289.

[226] I. Pang, H. Kim, S. Kim, K. Jeong, H. S. Jung, C.-J. Yu, H. Soh, J. Lee, *Org. Electron.* **2010**, *11*, 338.

[227] J. Z. Wang, Z. H. Zheng, H. W. Li, W. T. S. Huck, H. Sirringhaus, *Nat. Mater.* **2004**, *3*, 171.

[228] K. S. Lee, G. B. Blanchet, F. Gao, Y. Loo, *Appl. Phys. Lett.* **2005**, *86*, 074012.

[229] D. Li, L. J. Guo, *Appl. Phys. Lett.* **2006**, *88*, 063513.

[230] J. Jang, B. Lim, Angew. Chem. Int. Ed. 42 (2003) 5600.

[231] D. Soltman, V. Subramanian, *Langmuir* **2008**, *24*, 2224.

[232] B.-J. De Gans, U. S. Schubert, *Macromol. Rapid Commun.* **2003**, *24*, 659.

[233] M. Lefenfeld, G. Blanchet, J. A. Rogers, *Adv. Mater.* **2003**, *15*, 1188.

[234] C. Arribas, D. Rueda, *Synth. Met.* **1996**, *79*, 23.

[235] T. Kawase, H. Sirringhaus, R. H. Friend, T. Shimoda, *Adv. Mater.* **2001**, *13*, 1601.

[236] J. A. Lim, J. H. Cho, Y. D. Park, D. H. Kim, M. Hwang, K. Cho, *Appl. Phys. Lett.* **2006**, *88*, 082102.

[237] I. G. Hill, A. Rajagopal, A. Kahn, Y. Hu, *Appl. Phys. Lett.* **1998**, *73*, 662.

[238] N. Koch, A. Kahn, J. Ghijsen, J.-J. Pireaux, J. Schwartz, R. L. Johnson, A. Elschner, *Appl. Phys. Lett.* **2003**, *82*, 70.

[239] G. Jo, J. Maeng, T.-W. Kim, W.-K. Hong, B.-S. Choi, T. Lee, *J. Appl. Phys.* **2007**, *102*, 084508.

[240] O. D. Jurchescu, J. Baas, T. T. M. Palstra, *Appl. Phys. Lett.* **2004**, *84*, 3061.

[241] L. Liao, Y. C. Lin, M. Q. Bao, R. Cheng, J. W. Bai, Y. Liu, Y. Q. Qu, K. L. Wang, Y. Huang, X. Duan, *Nature* **2010**, *467*, 305.

[242] H. Jang, Y.-K. Kim, H.-M. Kwon, W.-S. Yeo, D. E. Kim, D.-H. Min, *Angew. Chem. Int. Ed.* **2010**, *49*, 5703.

[243] Z. Yin, S. Sun, T. Salim, S. Wu, X. Huang, Q. He, Y. M. Lam, H. Zhang, *ACS Nano* **2010**, *4*, 5263.

[244] K. S. Novoselov, A. K. Geim, S. V. Morozov, D. Jiang, Y. Zhang, S. V. Dubonos, I. V. Grigorieva, A. A. Firsov, *Science* **2004**, *306*, 666.

[245] C. Berger, Z. Song, X. Li, X. Wu, N. Brown, C. Naud, D. Mayou, T. Li, J. Hass, A. N. Marchenkov, E. H. Conrad, P. N. First, W. A. De Heer, *Science* **2006**, *312*, 1191.

[246] K. S. Kim, Y. Zhao, H. Jang, S. Y. Lee, J. M. Kim, K. S. Kim, J.-H. Ahn, P. Kim, J.-Y. Choi, B. H. Hong, *Nature* **2009**, *457*, 706.

[247] Y. Guo, C.-A. Di, H. Liu, J. Zheng, L. Zhang, G. Yu, Y. Liu, *ACS nano* **2010**, *4*, 5749.

[248] J. Geng, L. Liu, S. B. Yang, S.-C. Youn, D. W. Kim, J.-S. Lee, J.-K. Choi, H.-T. Jung, *J. Phys. Chem. C* **2010**, *114*, 14433.

[249] H. A. Becerril, J. Mao, Z. Liu, R. M. Stoltenberg, Z. Bao, Y. Chen, *ACS Nano* **2008**, *2*, 463.

[250] K. Suganuma, S. Watanabe, T. Gotou, K. Ueno, *Appl. Phys. Express* **2011**, *4*, 021603.

[251] G. Eda, G. Fanchini, M. Chhowalla, *Nat. Nanotechnol.* **2008**, *3*, 270.

[252] T.-K. Hong, D. W. Lee, H. J. Choi, H. S. Shin, B.-S. Kim, *ACS Nano* **2010**, *4*, 3861.

[253] L. Gomez De Arco, Y. Zhang, C. W. Schlenker, K. Ryu, M. E. Thompson, C. Zhou, *ACS Nano* **2010**, *4*, 2865.

[254] M. Samal, J. M. Lee, I. P. Won, D. K. Yi, U. Paik, C.-L. Lee, *J. Nanosci. Nanotechnol.* **2011**, *11*, 10069.

[255] X. Wang, L. Zhi, K. Mullen, *Nano Lett.* **2007**, *8*, 323.

[256] D. Yang, A. Velamakanni, G. Bozoklu, S. Park, M. Stoller, R. D. Piner, S. Stankovich, I. Jung, D. A. Field, C. A. Ventrice Jr., R. S. Ruoff, *Carbon* **2009**, *47*, 145.

[257] S. Pei, H.-M. Cheng, *Carbon* **2012**, *50*, 3210.

[258] N. Camara, J.-R. Huntzinger, G. Rius, A. Tiberj, N. Mestres, F. Pérez-Murano, P. Godignon, J. Camassel, *Phys. Rev. B: Condens. Matter* **2009**, *80*, 125410.

[259] Q. Zheng, W. H. Ip, X. Lin, N. Yousefi, K. K. Yeung, Z. Li, J.-K. Kim, *ACS Nano* **2011**, *5*, 6039.

[260] V. Singh, S. Sengupta, H. S. Solanki, R. Dhall, A. Allain, S. Dhara, P. Pant, M. M. Deshmukh, *Nanotechnology* **2010**, *21*, 165204.

[261] W. Zhu, T. Low, V. Perebeinos, A. A. Bol, Y. Zhu, H. Yan, J. Tersoff, P. Avouris, *Nano Letters* **2012**, *12*, 3431.

[262] J.-W. Jiang, J.-S. Wang, B. Li, *Phys. Rev. B: Condens. Matter* **2009**, *80*, 205429.

[263] A. K. Kulkarni, T. Lim, M. Khan, K. H. Schulz, *J. Vac. Sci. Technol. A* **1998**, *16*, 1636.

[264] K.-J. Lee, A. P. Chandrakasan, J. Kong, *IEEE Electr. Device L.* **2011**, *32*, 557.

[265] R. Singh, P. Kroll, *J. Phys.: Condens. Matter* **2009**, *21*, 196002.

[266] H. Hwang, P. Joo, M. S. Kang, G. Ahn, J. T. Han, B.-S. Kim, J. H. Cho, *ACS Nano* **2012**, *6*, 2432.

[267] B. N. J. Persson, H. Ueba, *J. Phys.: Condens. Matter* **2010**, *22*, 462201.

[268] K.-H. Shin, J. Cho, J. Jang, H. S. Jang, E. S. Park, K. Song, S. H. Kim, *Org. Electron.* **2012**, *13*, 715.

[269] A. N. Sokolov, M. E. Roberts, O. B. Johnson, Y. Cao, Z. Bao, *Adv. Mater.* **2010**, *22*, 2349.

[270] J. Liu, D. Haynes, C. Balliet, R. Zhang, T. Kowalewski, R. D. McCullough, *Adv. Funct. Mater.* **2012**, *22*, 1024.

[271] G. Lu, J. Blakesley, S. Himmelberger, P. Pingel, J. Frisch, I. Lieberwirth, I. Salzmann, M. Oehzelt, R. Di Pietro, A. Salleo, N. Koch, D. Neher, *Nat. Commun.* **2013**, *4*, 1588.

[272] S. Xiao, S. J. Kang, Y. Zhong, S. Zhang, A. M. Scott, A. Moscatelli, N. J. Turro, M. L. Steigerwald, H. Li, C. Nuckolls, *Angew. Chem. Int. Ed.* **2013**, *52*, 4558.

[273] R. V. Salvatierra, C. E. Cava, L. S. Roman, A. J. G. Zarbin, *Adv. Funct. Mater.* **2013**, *23*, 1490.

[274] H.-P. Cong, X.-C. Ren, P. Wang, S.-H. Yu, *Energy Environ. Sci.* **2013**, *6*, 1185.

[275] A. G. MacDiarmid, A. J. Epstein, *Synth. Met.* **1994**, *65*, 103.

[276] A. G. MacDiarmid, A. J. Epstein, *Synth. Met.* **1995**, *69*, 85.

[277] D. H. Kim, D. Y. Lee, H. S. Lee, W. H. Lee, Y. H. Kim, J. I. Han, K. Cho, *Adv. Mater.* **2007**, *19*, 678.

[278] C. W. Sele, B. K. C. Kjellander, B. Niesen, M. J. Thornton, J. B. P. H. van der Putten, K. Myny, H. J. Wondergem, A. Moser, R. Resel, A. J. J. M. van Breemen, N. van Aerle, P. Heremans, J. E. Anthony, G. H. Gelinck, *Adv. Mater.* **2009**, *21*, 4926.

[279] J. Huang, R. B. Kaner, *Angew. Chem. Int. Ed.* **2004**, *43*, 5817.

[280] J. Chen, C. K. Tee, M. Shtein, D. C. Martin, J. Anthony, *Org. Electron.* **2009**, *10*, 696.

[281] R. Z. Rogowski, A. Dzwilewski, M. Kemerink, A. A. Darhuber, *J. Phys. Chem. C* **2011**, *115*, 11758.

[282] S. K. Park, T. N. Jackson, J. E. Anthony, D. A. Mourey, *Appl. Phys. Lett.* **2007**, *91*, 063514.

[283] K. N. Choi, K. S. Kim, K. S. Chung, H. Lee, *IEEE T. Device Mat. Re.* **2009**, *9*, 489.

[284] C. S. Kim, S. Lee, E. D. Gomez, J. E. Anthony, Y.-L. Loo, *Appl. Phys. Lett.* **2008**, *93*, 103302.

[285] Y. W. Wang, J. L. Cheng, Y. K. Wang, T. H. Hu, J. C. Ho, C. C. Lee, T. F. Lei, C. F. Yeh, *Thin Solid Films* **2004**, *467*, 215.

[286] S. H. Han, J. H. Kim, S. M. Cho, S. H. Lee, D. J. Choo, M. H. Oh, J. Jang, *Appl. Phys. Lett.* **2006**, *88*, 073519.

[287] W. L. Yang, T. S. Chao, C.-M. Cheng, T. M. Pan, T. F. Lei, *IEEE T. Electron Dev.* **2001**, *48*, 1304.

[288] A. Hossain, A. E. Bolotnikov, G. S. Camarda, Y. Cui, S. Babalola, A. Burger, R. B. James, *J. Electron. Mater.* **2008**, *37*, 1356.

[289] M. Halik, H. Klauk, U. Zschieschang, G. Schmid, C. Dehm, M. Schütz, S. Malsch, F. Effenberger, M. Brunnbauer, F. Stellacci, *Nature* **2004**, *431*, 963.

[290] S. Kobayashi, T. Nishikawa, T. Takenobu, S. Mori, T. Shimoda, T. Mitani, H. Shimotani, N. Yoshimoto, S. Ogawa, Y. Iwasa, *Nat. Mater.* **2004**, *3*, 317.

[291] K. P. Pernstich, S. Haas, D. Oberhoff, C. Goldmann, D. J. Gundlach, B. Batlogg, A. N. Rashid, G. Schitter, *J. Appl. Phys.* **2004**, *96*, 6431.

[292] M. McDowell, I. G. Hill, J. E. McDermott, S. L. Bernasek, J. Schwartz, *Appl. Phys. Lett.* **2006**, *88*, 073505.

[293] M. Park, J. Jang, S. Park, J. Kim, J. Seong, J. Hwang, C. E. Park, *Appl. Phys. Lett.* **2012**, *100*, 102110.

[294] H. B. Akkerman, H. Li, Z. Bao, *Org. Electron.* **2012**, *13*, 2056.

국문초록

유기전자소자는 우리의 일상생활에 여러가지 면에서 상당한 변혁을 가져올 것으로 예상된다. 가장 기대되는 응용분야는 디스플레이, 발광모듈, 유기태양전지 등이다. 유기전자소자는 현재의 소자에 비하여 가볍고 얇으며 내구성이 뛰어나고 유연하다는 큰 장점을 가지고 있다. 그런데 유기전자소자의 성능, 효율 및 수명은 사용된 유기전극의 광학적, 전기적, 구조적 특성과 매우 밀접한 관계가 있다. 이러한 유기전극은 높은 광학적 투과도와 전기 전도도, 구조적 안정성, 강한 박막-기판간의 점착성, 낮은 대기 투과도 등의 구체적인 요구조건들을 만족해야만 한다.

기존에는 투명한 전도성 산화물로 이루어진 전극이 각광을 받고 많은 연구가 이루어졌다. 전통적으로, 인듐-주석 산화물이 높은 광학적 투과도와 낮은 전기 저항 때문에 주로 사용되어 왔으나 인듐-주석 산화물은 몇 가지 중요한 문제점을 안고 있다. 인듐의 공급이 채굴과 지정학적인 문제로 제한되고 있기 때문에 가격이 상대적으로 비싸다. 그리고 인듐-주석 산화물을 증착하는 수율이 낮을 뿐만 아니라 공정을 건립하고 유지하는 데에도 많은 비용이 소모된다. 또한 인듐-주석 산화물은 상대적으로 낮은 압력에도 쉽게 균열이 발생하거나 깨지는 문제가 있다. 이것은 이미 많은 현재의 소자에서 문제가 되고 있으며, 앞으로의 유연전기소자 구현에 있어서도 큰 장벽으로 작용한다.

가볍고, 깨지지 않으며, 유연하고, 말 수 있으며, 궁극적으로는 투명하기까지한 유기전자소자를 구현하기 위해서는 반드시 기존의 금속 기반 구성품들이 유기물질로 대체되어야만 한다. 본 연구는 유기전자소자의 유연하고 투명한 전극으로 적용될 수 있는 물질로서 전도성 고분자와 그래핀에 초점을 맞추어 가능성 있는 해결책을 제시한다. 캄포술폰산이 이차도핑된 폴리아닐린은 용액 공정이 가능하므로 유리, 인듐-주석 산화물 기판은 물론 유연한 고분자 기판에도 성공적으로 도포할 수 있어 고전도성 폴리아닐린 전극을 제조할 수 있게 해 주었다. 잉크젯 프린팅이 매개된 기상증착중합법은 비분산성 전도성 고분자 전극 패터닝에 적용할 수 있는 아주 유용한 방법이다. 이 방법을 이용하여 상향접촉식 박막트랜지스터에 기존의 금속 전극을 대체하는 정교하게 패턴된 폴리피롤 전극을 제조할 수 있었다. 화학적 환원과 압력-도움 열환원 공정을 결합하여, 180도의 온도에서 환원된 산화그래핀 투명 전극을 제조하는 새롭고 신뢰성 있는 방법을 고안하였다. 상대적으로 낮은 공정온도 덕분에 유연한 고분자 기판이 사용 가능해짐으로써 유연하고 투명한 그래핀 전극 제조가 비로소 가능했다. 이 환원 공정은 기존에 그래핀 박막 생산을 위해 사용되던 전사 또는 각인 과정 없이 환원된 산화그래핀을 제조할 수 있다는 장점을 가진다. 이러한 본 연구에서 제조된 유기전극들은 화학센서, 염료감응형 태양전지, 유기박막트랜지스터 등을 포함하여 유기전자소자와 관련된 많은 새로운 형태의 응용분야에 매우 유용하게 활용될 수 있을 것으로 사료된다.

주요어: 유기전극; 전도성 고분자; 그래핀; 화학센서; 염료감응형 태양전지; 유기박막 트랜지스터

학번: 2010-30806